



Novel Nanofabrications for Advanced Nanophotonic and Optoelectronic Devices

**A thesis submitted in fulfilment of the requirements for the degree of
Doctor of Engineering.**

Salah Ezzat Mohamed El-Zohary

**Department of Optical Systems Engineering
Graduate School of Advanced Technology and Sciences**

The University of Tokushima, Tokushima, Japan

March 2014

STATEMENT OF ORIGINAL AUTHORSHIP

The work contained in this thesis has not been previously submitted to meet requirements for an award at this or any other higher education institution. To the best of my knowledge and belief, the thesis contains no material previously published or written by another person except where due reference is made.

ACKNOWLEDGMENT

All praise and thankfulness is due my **Creator Almighty “ALLAH”**. I greatly thank **Allah** for giving me the inspiration, patience, time, and the ability to finish this work. With **His** will and mercy, I have been guided to all those great people who helped me to finish this work.

I am heartily thankful to my supervisors, **Prof. Masanobu Haraguchi** and **Prof. Toshihiro Okamoto**, whose encouragement, guidance and support from the initial to the final level throughout my research.

I am heartily thankful to **Dr Mohamed Swillam** and **Dr Nageh Allam** who served as co-supervisors during my research through research collaboration between our laboratory and their laboratory in **Physics Department, The American University in Cairo**.

I am also grateful to my family who face with me all difficulties in Japan, **my beloved wife Marwa El Marhoumy, my beloved sons Mohamed, Abu Bakr and Omar**. I could not complete this work without their unwavering love, patience, prayer and supplications.

Thanks to all colleagues at the **Department of Optical Science and Technology, Tokushima University**. Thanks to **Dr. Yoshinori Nakagawa from Nichia Corporation, Tokushima, Japan** for his interesting discussions about fabrication and characterization process. Thanks to **Dr. Hiroyuki Okamoto, Anan National college of Technology, Tokushima, Japan** for his helping in the simulation work. Thanks to **Dr. Mohamed Shenashen, Post Doctor from Egypt** for helping in the chemical preparations, for good advises and his cooperation.

Thanks to **Abdulilah Azzazi**, undergraduate student at The American University in Cairo who helped a lot through simulation.

I would like to acknowledge **financial support received from the NEC C&C Foundation of Japan.**

My deep love to **my family and my wife's family, in Egypt**, they always support me to face any difficulty in my life and my research.

Lastly, I cannot forget home university **Tanta University**, I would like to thank my professors, my friends and everybody in **Physics Department, Faculty of Science, Tanta University, Egypt**, they provided me the knowledge and information in my undergraduate and graduate study.

SUMMARY

Current micro-scale electronics technology has been approaching rapidly towards its technological limit. This has shifted the focus towards nano-scale technology in recent years. More and more researchers around the world are working for bringing nano-scale technology into mainstream.

The research carried out here is a small step towards a similar goal. Novel nanofabrications and nanostructures could be fabricated, developed and optimized. The resulted nanofabrications will help to investigate novel optoelectronic and nanophotonic devices. So the research described here is a little step combining the worlds of nanophotonics and optoelectronics.

Our research revolves around two kinds of nanofabrications. One of which is based on (Si) silicon, a material that the semiconductor industry has been working on for over thirty years; it would be really attractive to stay on silicon and also achieve good device metrics that nanoelectronics provides.

So a part of our research based on Nanostructuring of Si to develop new electronic and optoelectronic devices. Si nanostructures such like porous Si and Si nanowires were main Si nanostructures we have been focused upon. Generally porous Si and Si nanowires have been the focus of intensive research over the past decade due to their unique physical morphology and the associated electrical, mechanical, and thermal properties.

The Si nanostructures mentioned above were the first step towards a fabrication of heterojunction diode. So fabrication of Si nanowires or porous Si was followed by synthesis and fabrication of Nanopolyaniline (NPANI) and its derivative polyortho-toluidine (POT).

Generally the intense attention and research on conducting polymers have resulted with number of practical applications because of their distinct electronic properties, diversity, ease of fabrication and potentially low cost. PANI and its derivatives have attracted significant interest as electronic material because of its high capacity, good conductivity, unique doping–dedoping process, and ease of synthesis. Finally we could finalize the first part our research which is a fabrication and characterization of a heterojunction diode, the porous Si or Si nanowires serve as p-type and PANI or POT serve as n-type.

The second type of nano-structure developed and investigated, is based upon nano-metallic which could be called as a plasmonic nanostructure. In general, surface plasmon wave is formed through coherent oscillation of free electrons at a metal-dielectric interface, thus generate a phenomenon called plasmon resonance effect.

So in this part of research we succeeded to design a plasmonic sensor to detect the minor changes of refractive index. We propose a novel system using the plasmonic resonator for detecting a micro change of the refractive index. The detection performance of our device has been numerically evaluated by (FDTD) finite-difference time-domain simulations. Our design could be easily fabricated using the focus ion beam milling technique. It leads to a highly compact sensor in terms of high integration in dimensions of few hundred nanometers associated with a high sensitivity and high detection limit.

Based on the same idea of plasmonic resonance, It is possible to fabricate a novel metallic nanostructure which is Silver-coated Si nanowire. Again we return to a useful application of Si nanowires to do Surface Enhanced Raman Spectroscopy (SERS), making use of the metal nano-array developed. The results we have need more analysis and left for future research. Only the concept and idea of fabrication mentioned in thesis in chapter 1 (General introduction) and in chapter 4 (General conclusions and future work).

List of Figures

Figure 1.	Absorption of gold nanoparticles of different sizes and shapes and fluorescence emission for different CdSe nanoparticle sizes.....	2
Figure 2.	Towards the nanometer scale, nm scale of some natural things and for other things that Man could fabricate in the nm scale	3
Figure 3.	Schematic illustration of different steps to fabricate Si V-grooves as an example of top-down fabrication method.....	7
Figure 4.	Schematic representation showing the basic components of a typical EBL and FIB systems.....	10
Figure 5.	Different aspects for the bottom-up fabrication.....	11
Figure 6.	Schematic diagram of the P <i>Si</i> anodization circuit.....	14
Figure 7.	Schematic drawing of the VLS process as it takes place in a PVD or CVD deposition experiment	17
Figure 8.	Mechanism of SiNWs formation during metal-assisted chemical etching of Si falling down of Ag particles from the surface to the bulk Si occurred to form SiNWs.....	19
Figure 9.	Structure of PANI and Its derivative POT.....	22
Figure 10.	SPs generation when light beam striking a metal. The figure shows a schematic representation of an electron density wave propagating along a metal/dielectric interface.....	25
Figure 11.	NPANI SEM micrographs and rod-like shape nanostructures.....	38
Figure 12.	TEM micrograph of synthesized rod-like PANI.....	39
Figure 13.	FTIR spectrum of the synthesized NPANI.....	40
Figure 14.	UV-visible spectrum of the synthesized NPANI.....	41
Figure 15.	I-V characteristics of NPANI/P <i>Si</i> heterojunction at different temperatures.....	43
Figure 16.	ln(I) vis Bias voltage(V) for NPANI/P <i>Si</i> heterojunction at various temperatures in dark.....	44
Figure 17.	Temperature dependence of Barrier height and Ideality factor	46

Figure 18. Barrier height versus ideality factor for the NPANI/PSi heterojunction.....47

Figure 19. Richardson plot for the NPANI/PSi heterojunction.....48

Figure 20. $dV/d(\ln I) - I$ curves of the NPANI/PSi heterojunction at different temperatures.....38

Figure 21. Top view (a tilt angle of 45 degrees) of SiNW arrays after 15 min of etching in 5 M HF, 0.02 M AgNO₃, and 0.05 M KMnO₄ aqueous solution.....56

Figure 22. Top view (a tilt angle of 45 degrees) of SiNW arrays formed using in 5 M HF, 0.02 M AgNO₃, and 0.05 M KMnO₄ aqueous solution57

Figure 23. Top views (tilt angle of 45 degrees) of SiNW arrays after 30 min of etching in 5 M HF, 0.02 M AgNO₃, and 0.05 M KMnO₄ aqueous solution.....58

Figure 24. Top views (tilt angle of 45 degrees) of SiNW arrays after 40 min of etching in 5 M HF, 0.02 M AgNO₃, and 0.05 M KMnO₄ aqueous solution.....59

Figure 25. UV-visible spectrum and FTIR spectrum of the synthesized NPANI.....61

Figure 26. X-ray diffraction (XRD) patterns of POT.....62

Figure 27. NPOT SEM micrographs and rod-like shape nanostructures.....62

Figure 28. Scanning electron micrograph of SiNWs after the deposition of NPOT.....63

Figure 29. I-V curves for NPANI/PSi heterojunction in dark at room temperature.....64

Figure 30. $\ln I - V$ plot of the PtSi/p-Si Schottky diode at the temperature of 293 K in dark.....67

Figure 31. The $dV/d\ln I$ vs. I plot of NPOT/SiNWs heterojunction diode at the temperature of 293 K.....69

Figure 32. $H(I)$ vs I plot of NPOT/SiNWs heterojunction.....70

Figure 33. Schematics of the plasmonic square resonator with a trench structure used in the FDTD simulations. The figure shows a schematic of the plasmonic square resonator using Metal-Insulator-Metal (MIM) configuration.....76

Figure 34. Transmission spectra of plasmonic square resonator as a function of wavelength.....78

Figure 35.	A proposed design of an integrated hybrid chip involving our proposed plasmonic sensor.....	79
Figure 36.	Profiles of the electric field in the plasmonic square resonator	81
Figure 37.	Transmission intensity at the wavelength of 691 nm as a function of the refractive index changes of materials surrounding the plasmonic square resonator.....	82
Figure 38.	Transmission intensity as a function of the wavelength for different gap size.....	83
Figure 39.	Transmission intensity as a function of the wavelength for gap of 20 nm and gap of 22 nm.....	84
Figure 40.	Transmission intensity as a function of different square resonator dimensions.....	85

LIST OF TABLES

Table 1. Saturation current (I_0), barrier height (Φ_B), ideality factor (η) and R_s factor for NPANI/PSi heterojunction. The values of saturation current (I_0), barrier height (Φ_B), ideality factor (η) and R_s factor for NPANI/PSi heterojunction were calculated from the forward I–V characteristics at different temperatures48

Table of Contents

STATEMENT OF ORIGINAL AUTHORSHIP.....	i
ACKNOLEDGMENT.....	ii
SUMMARY.....	iv
LIST OF FIGURES.....	vii
LIST OF TABLES.....	x
CHAPTER 1: GENERAL INTRODUCTION.....	1
1.1 Nanoscience and Nanofabrication Technologies	1
1.2 MEMS and NEMS.....	4
1.3 Nanofabrication Technologies.....	4
1.4 Silicon based nanofabrication technology.....	5
1.5 Top-down and down-top fabrication.....	6
1.6 Promised Si nanofabrications.....	12
1.7 Wet Chemical & Electrochemical Etching of Si.....	12
1.7.1 Wet Chemical Etching.....	12
1.7.2 Electrochemical Etching of Si.....	13
1.8 Methods for SiNWs fabrication.....	15
1.8.1 VLS growth mechanism to fabricate SiNWs.....	15
1.8.2 Metal-assisted chemical etching of Si.....	17
1.9 Conducting Polymers.....	20
1.9.1 PANI and its Derivative.....	21
1.10 Si /Conducting Polymers Heterojunctions.....	22

1.11 Metal Nanofabrications and Plasmonics.....	23
1.11.1 Plasmonics & Refractive Index Change.....	25
1.12 SiNWs-Based Surface-Enhanced Raman.....	26
1.13 Objective/approach and Summary of chapters.....	27
CHAPTER 2: Electrical Characterization of NPANI/PSi Heterojunction at High Temperatures.....	31
ABSTRACT.....	31
2.1 Introduction.....	31
2.2 Preparation of PSi substrates.....	35
2.3 Preparation of NPANI / PSi heterojunction.....	36
2.4 Characterization.....	36
2.5 RESULT AND DISCUSSION.....	37
2.5.1 Morphological, Structural and Optical Properties.....	37
2.6 I–V measurements.....	41
CONCLUSION.....	51
CHAPTER 3: Synthesis and Characterization of NPOT/Si NWs Heterojunction.....	52
ABSTRACT.....	52
3.1 Introduction.....	52
3.1.1 POT as PANI Derivative.....	53
3.1.2 Silicon micropillar /nanowire composite structure.....	53
3.2 Experimental Work.....	54
3.3 Results and discussion.....	55
3.3.1 Mechanism for the Formation of SiNWs Array.....	55

3.3.2 Characterization of NPOT.	59
3.4 Characterization of NPOT/Si NWs Heterojunction.....	63
3.4.1 I-V characteristics of heterojunction.....	64
CONCLUSION.....	72
CHAPTER 4: Design and Characterization of Integrated a Plasmonic Nanosensor for lab-on-chip applications.....	73
ABSTRACT.	73
4.1 Introduction	73
4.2 FDTD Simulations.	75
4.3 Wavelength characteristics of the plasmonic square resonator.	76
4.4 Electric field profiles of the plasmonic square resonator.....	80
4.5 Analysis of the detection limit of the refractive index Change.....	81
4.6 Sensitivity Analysis of the Proposed Sensor.....	83
CONCLUSION.....	86
CHAPTER5: GENERAL CONCLUSIONS & FUTURE WORK.....	87
5.1 General Conclusions.....	87
5.2 Future Work.....	89
REFERENCES.....	92

CHAPTER 1: GENERAL INTRODUCTION

1.1 Nanoscience and Nanofabrication Technologies

The prefix “nano” comes from the Greek meaning “dwarf”. It is one billionth, which is expressed mathematically as 10^{-9} . One nanometer (nm) is about 3 atoms long. Reducing size to reach nm was helping to achieve the well-known old discovery which reported that, the melting point of gold decreases rapidly as the particle dimensions reaches the nm scale. It was also reported that gold and other noble metal nanoparticles could give brilliant colors. These brilliant colors were found to depend on the shape and size of the nanoparticle and also depend on the dielectric surrounding medium [1-3].

Nanomaterials and nanostructures were found to give such new and unique properties which could not be found in the bulk materials. The new properties or behaviour associated with different nm scale of some materials could be explained according to two main reasons [1]:

1. The ratio of surface area-to-volume of the structure increases. So most atoms brought to be at or near the surface. As a result, atoms become more weakly bonded and more reactive.
2. It was found that, the quantum mechanical effects play an important role when the size of the structure become on the same scale as the wavelengths of electrons. So a quantum confinement occurs resulting in changes of electronic and optical properties of the new nm structure.

Figure 1 is showing the absorption of gold nanoparticles of different sizes and shapes. Also in Fig. 1, we can see for a semiconductor like CdSe, the change of nanoparticle size could alter a fluorescence emission with different colors. Such fluorescence colors are depending on size and shape of CdSe nanoparticles. There are many examples was indicating unique and novel properties of some nanoscale structures or nanofabrications could be found in case of bulk structure or materials. This gives potentials to nanomaterials and nanofabrications to be used in many useful applications and in different aspects and fields. [3].

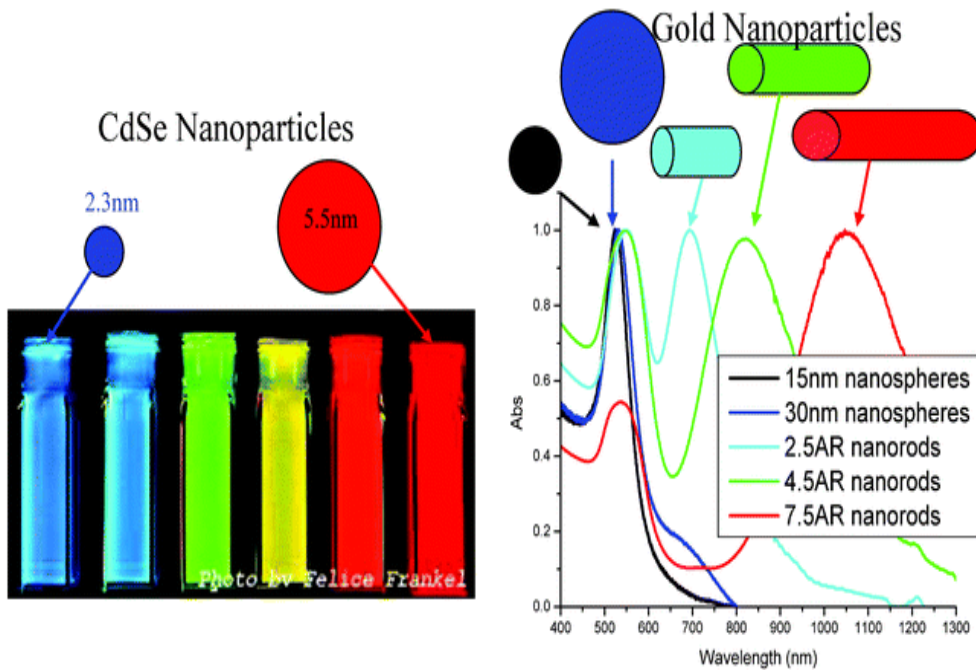


Figure 1. Absorption of gold nanoparticles of different sizes and shapes and fluorescence emission for different CdSe nanoparticle sizes [3].

From the previous information, the term “Nanotechnology” could be defined as: building and using materials, devices and machines at the nm (atomic/molecular) scale, making use of unique properties that occur for structures at those small dimensions [1-3].

Figure 2 shows how small is nm scale for some natural things and for other things that Man could fabricate.

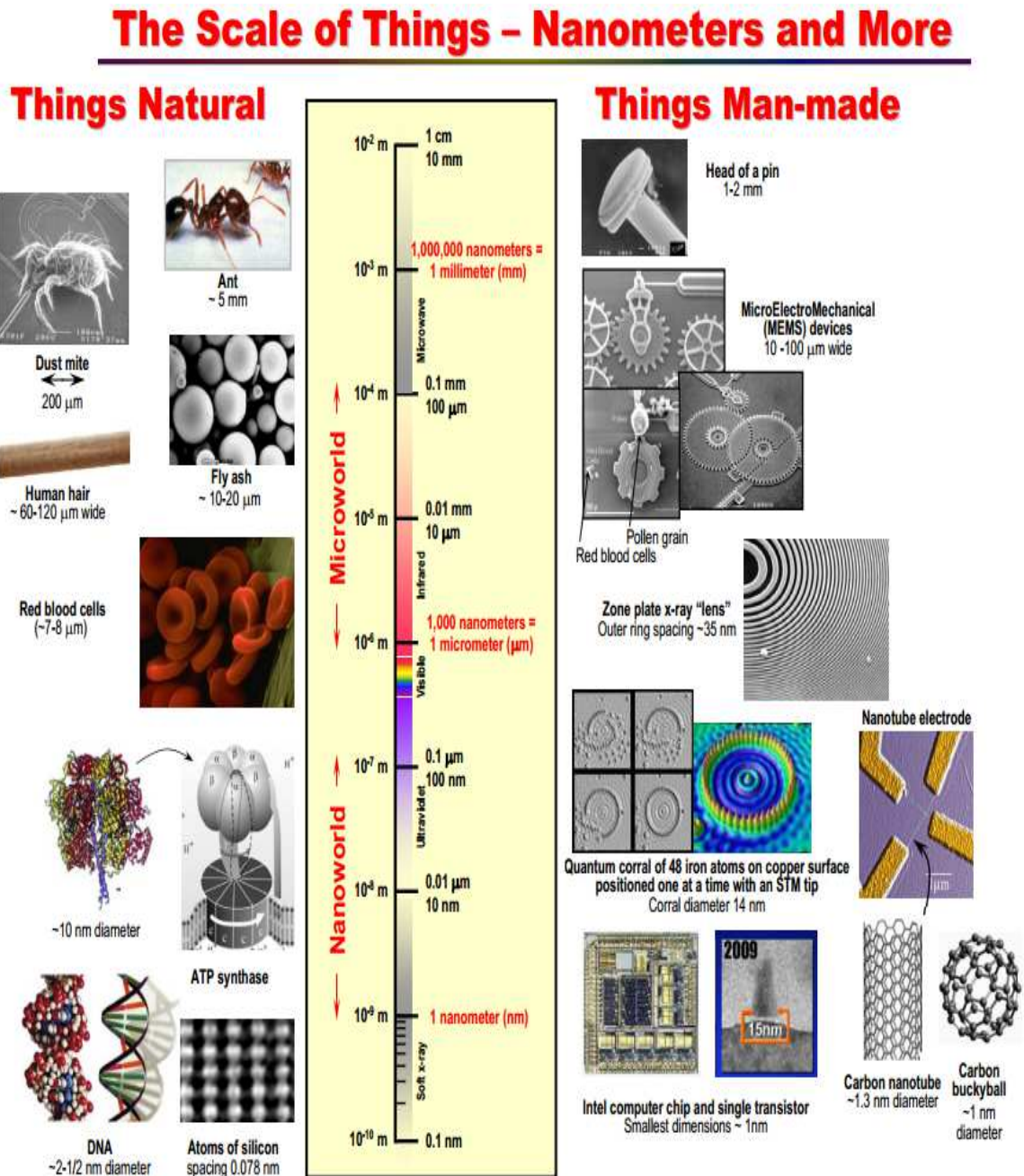


Figure 2. Towards the nanometer scale, nm scale of some natural things and for other things that Man could fabricate in the nm scale [1].

1.2 MEMS and NEMS

There are many beneficial attributes of Micro-Electro-Mechanical Systems (MEMS) and Nano-Manufacturing. Generally, it was found that miniaturization of micro- and nanosystems enable many benefits including increased portability, lower power consumption. It could provide the ability to place radically more functionality in a smaller amount of space without any increase in weight. Also it could provide the ability to make the signal paths smaller. All of these features make the overall performance of electromechanical systems to be enormously improved. The trend towards Nano-Electro-Mechanical Systems (NEMS) is driven by the common perception that miniaturization reduces costs by decreasing material consumption and allowing batch fabrications.

A positive side effect of NEMS is that more functionality which could be integrated on the same or smaller footprint. In addition, through reduced size and mass, NEMS could provide the means to deploy systems at places where traditional systems won't fit [4-6].

A large variety of nanoscale and microscale structures and devices, as well as systems integrate structures, devices, and subsystems have been widely used, and a worldwide market for NEMS and MEMS and their applications will be drastically increased in the near future.

1.3 Nanofabrication Technologies

Nanoscience and Nanotechnology are advancing at a rapid pace and making revolutionary contributions in many fields including electronics, materials science, chemistry, biology, structures, mechanics, and optoelectronics. Nanoscale materials are particularly interesting for photonics, which can be defined as the science and technology of light. Photonics

supplements electronics in the form of optoelectronics, and it is considered as one of the key technology areas of the 21st century. Nanofabrication technologies are applied for the manufacturing of nanoscale devices applicable to fields of research such as microelectronics or nanophotonics [7- 10].

Nanofabrication is a very active area of research. As can be noticed a huge number of research articles and publications appear continuously. All are trying in providing novel nanofabrications for promised devices and applications.

The research carried out here may be considered as a small step towards a similar goal. We believe that nanofabrications and nanostructures presented here in thesis could be developed and optimized to help to investigate novel optoelectronic and nanophotonic devices and combining the worlds of nanophotonics and optoelectronics.

1.4 Silicon based nanofabrication technology

Silicon (Si), a material that semiconductor industry has been working on for over thirty years; it would be really attractive to stay on Si achieving good device metrics that nanoelectronics can provide based on Si nanofabrications.

Although nanoscience and technology are progressing along many fronts, the most impressive progress has been made in the area of semiconductor technology. As we enter the 21st century, semiconductor nanostructures are revolutionizing many areas of electronics, optoelectronics, and photonics. Si has become the major platform for microelectronic processing boards. MEMS found to help in the integration of mechanical elements, sensors, actuators, and electronics on a common Si substrate through microfabrication technology. Due to historic reasons, Si is considered to be the most important material for the electronics

industry and in microelectronics enabling devices like diodes, transistors, and other important electronic devices [10, 11].

Si can be considered as the leading material for optoelectronics; hence the integration of all optical functions into Si technology is practically very important and widely recognized as a great challenge. Around 1982, the term micromachining came into use to designate the fabrication of micromechanical parts for Si microsensors. The micromechanical parts are fabricated by selectively etching areas of Si substrates away in order to leave behind the desired geometries [12, 13].

1.5 Top-down and down-top fabrications

To be able to fabricate nanoscale structures, you may choose between two fabrication methods to obtain your final structure. The first method is “top-down”. The top-down method is usually starting with a larger piece then followed by carving or etching some areas away to obtain the final design of the desired structure [1].

The top-down method usually starts by patterning process as in photolithography using masks. The unprotected parts or places will be etched away. The etching process could be performed once or in successive etching steps using different etchants.

Figure 3 give an example for a top-down method used in my master research to fabricate Si V-grooves. The target was to fabricate Si V-grooves as a part of fabrication of V-groove plasmonic waveguide using low cost method. This fabrication method passed through many steps including photolithography, isotropic wet chemical etching of SiO₂ using hydrofluoric acid (HF) solution and anisotropic wet chemical etching of Si using

potassium hydroxide (KOH) solution. The fabrication method can be described according to the fabrication steps shown in Fig. 3.

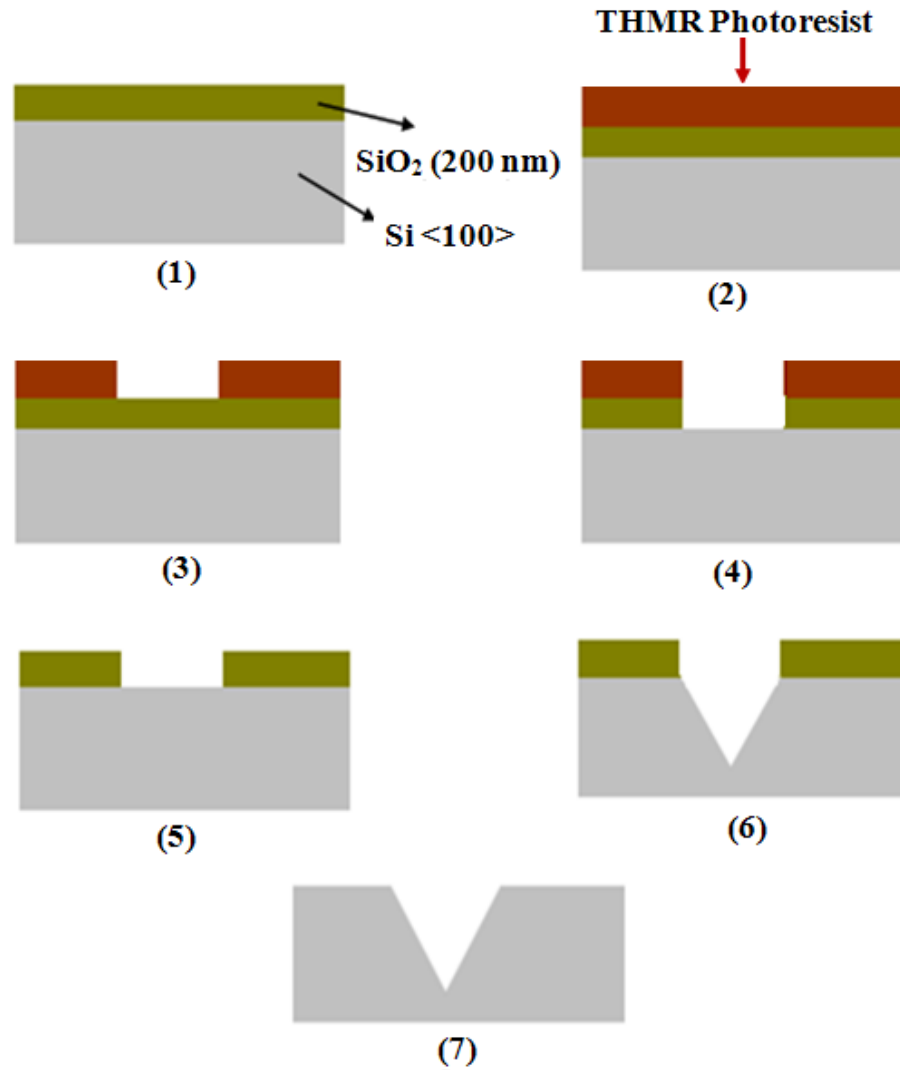


Figure 3. Schematic illustration of different steps to fabricate Si V-grooves as an example of top-down fabrication method.

The Fabrication of Si V-grooves as presented here serve as an example for the top-down method. In details this fabrication is divided into the following steps:

Step 1: Formation of thermal oxide layer of SiO_2 (200 nm) on the surface of Si samples. SiO_2 will serve as mask for KOH etching after removing the photoresist.

Step 2: Spin coating of (**THMR –iP3650**) photoresist which will oppose HF etching at the protected areas covered by the photoresist.

Step 3: Ultraviolet (UV) lithography and developing of the photoresist to leave protected and unprotected areas. The unprotected areas will undergo etching by HF solution.

Step 4: BHF isotropic etching of the unprotected areas of SiO₂ to produce Si areas instead.

Step 5: Removing of the photoresist from the protected areas.

Step 6: Anisotropic chemical etching using KOH solution. SiO₂ areas are protected and Si areas will only undergo KOH etching.

Step 7: Removing the silicon dioxide layer by last BHF etching to produce smooth Si V-grooves.

The previous procedures were a part of a top-down method to fabricate a Si microstructure. Of course one can find thousand microfabrications follow and serve as examples for the top-down method.

Due to diffraction effects, the practical limit for optical or photolithography is around 100 nm. Electron Beam Lithography (EBL) is a fundamental technique allowing direct writing of structures down to sub-10 nm dimensions. However e-beam projection systems using masks have not been fully developed. Also parameters such as proximity effect, thickness uniformity of resist layer, and manual development of samples have limited the resolution of EBL method [14]. Instead, “direct-write” e-beam lithography has been used. A typical EBL system is shown schematically as in Fig. 4 (a).

Briefly, the EBL system consists of an electron gun, electron optical column, and a vacuum chamber containing a laser controlled x/y stage. The x/y stage is used for accurately positioning the substrate under the beam. The electron optical column is used to form and direct a focused beam of electrons onto the surface of the substrate. The electron optical column is mounted in a holder and clamped to the stage. The electrons are produced in the

uppermost section, which is called the electron source or electron gun. After the beam of electrons emerges from the gun it passes through several additional stages in the electron optical column. Such specific beam modification processes is needed to produce a beam having the required current and spot size which could be correctly focused onto the substrate. Beam current and current density are critical parameters in the optimization of pattern writing time [14, 15].

The electron optical system is limited by the brightness of its electron gun, the imaging limitations of its lenses, and beam interactions along the beam path. The relative importance of these limitations depends upon the writing strategy used.

For a direct milling to fabricate nanostructure, Focus Ion Beam (FIB) method could be used. FIB machining offers the greatest resolution, with the ability to make features as small as 20 nm, but it is very slow [1, 14, 15].

For a direct milling using EB and FIB, it should be mentioned that those systems have series limitations due to high cost, complexity, and very low throughput. So in nanofabrications, if possible to avoid EB or FIB and depending upon alternative and low cost method will provide a great advantage and impact to the nanofabrication and its application [16, 17].

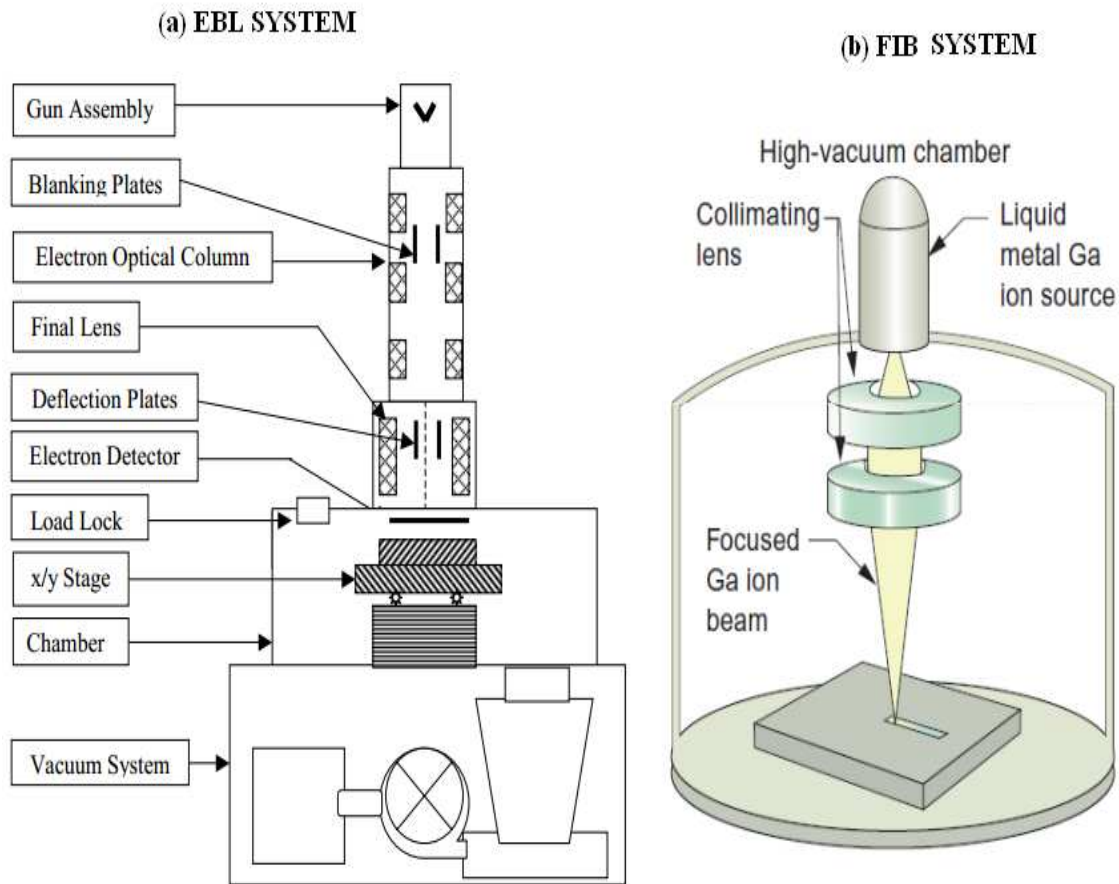


Figure 4. Schematic representation showing the basic components of a typical EBL and FIB systems [14].

An alternate method for the previous top-down method is “bottom-up” fabrication as shown in Fig. 5. As shown in Fig. 5, three types of the bottom-up fabrication included and could be described as:

- Adding atoms to atoms, molecules to molecules.
- Self-assembly of atoms and molecules.
- Use of chemical and biological processes.

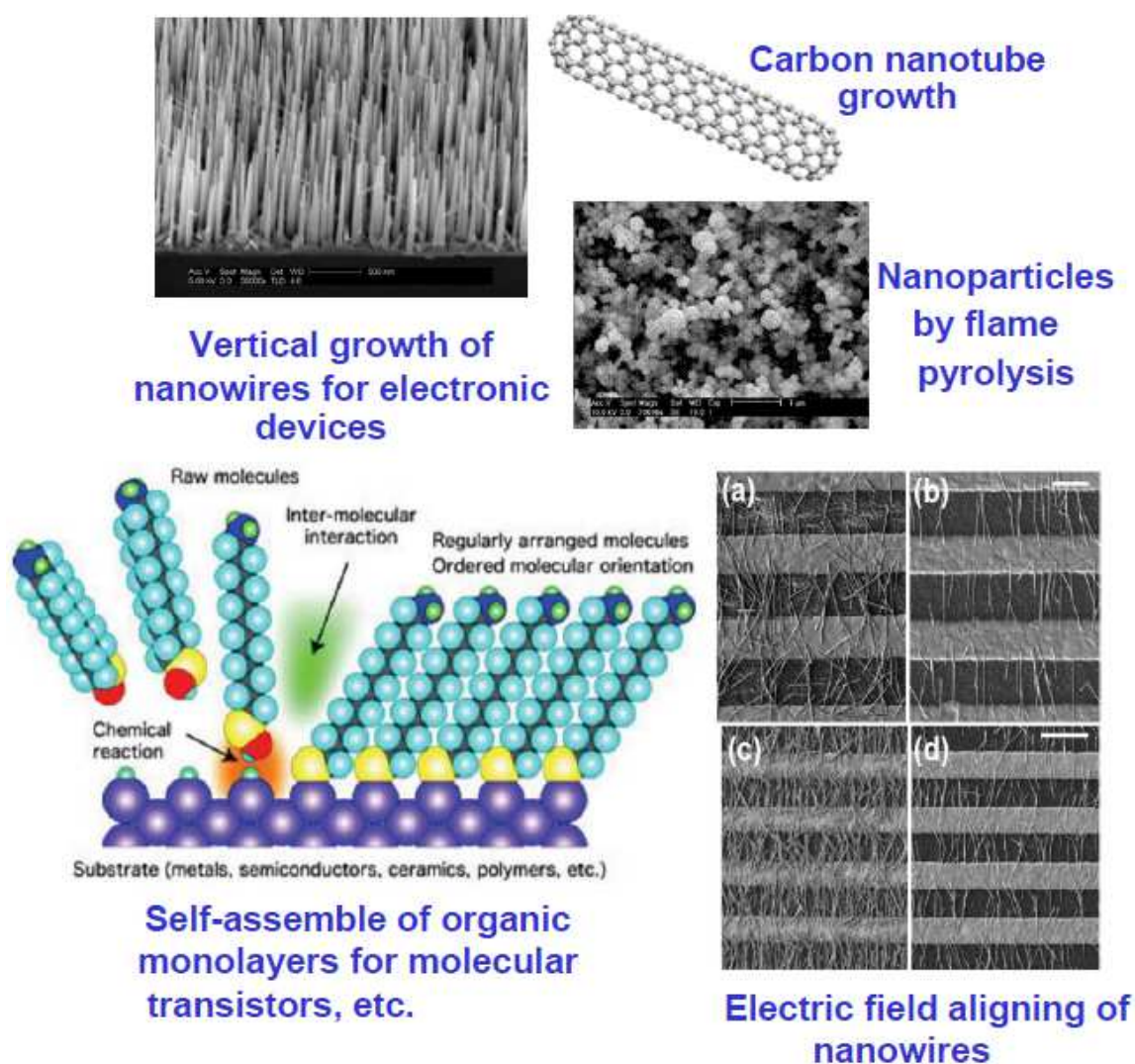


Figure 5. Different aspects for the bottom-up fabrication [1].

It should be mentioned that there are common strategies when fabricating a nanostructure using bottom-up fabrication such as using catalysts, stress fields, electric fields, capillary forces, diffraction gratings, etc... . These strategies are helping to achieve a selective growth or placement in only some specific locations. Also there are possibilities for using top-down processes in conjunction with bottom-up processes, to build a desired structure [18-21]. The strategy one can choose is depending upon properties of materials involved which could be Si or other materials based on the final design or nanostructure.

1.6 Promised Si nanofabrications

Si Nanostructuring is a mean for developing new electronic and optoelectronic devices. Si nanostructures such like porous Si (PSi) and Si nanowires (SiNWs) were the main Si nanostructures we have been focused upon. PSi and SiNWs have been the focus of intensive research done over the past decade due to their unique physical morphology and the associated electrical, mechanical, and thermal properties.

1.7 Wet Chemical & Electrochemical Etching of Si

Usually the fabricated devices are made out of semiconductor materials, dielectrics, oxides, and metals. Most of the manufacturing processes of nanoscale devices consist of two basic stages:-

- 1- Formation of an image on a surface of a material.
- 2- Processing and patterning the surface.

There are several techniques and fabrication means capable of performing the exposition and realization of the devices. In many times the nanofabrication technologies and methods need the chemical etching which is a technique includes etching of the surface of a material in corrosive fluids or gases. Different kinds of chemical etchants may be used and various types of materials can be etched (metals, dielectrics, semiconductors, etc...) [22- 24].

1.7.1 Wet Chemical Etching

Historically, wet etching techniques preceded dry techniques. Wet etching techniques still constitute an important group of etchants for micro/nanofabrication despite the fact that they

are used less frequently in very large-scale integration (VLSI) processes. This is the simplest etching technology and its entire requirement is a container with a liquid solution that will dissolve the material in question.

Usually a mask is desired to selectively etch the material. It is important to find a mask that will not dissolve or at least undergo etching much slower than the material to be patterned. In order to minimize the fabrication cost, which is the indispensable requirement of the industry; wet etching is preferred over dry etching as wet etching does not require any sophisticated and expensive machinery [25, 26].

1.7.2 Electrochemical Etching of Si

PSi can be considered as Si crystallite having a network of nanosized voids in it. The nanosized voids in the bulk Si result in a sponge-like structure of pores and channels surrounded with a skeleton of crystalline SiNWs. Described simply, PSi could be described as a network of air holes in a Si matrix. PSi was discovered in 1956 by Uhlir while performing electropolishing experiments on Si wafers using an electrolyte containing HF acid [27].

PSi substrates are commonly prepared by chemical or electrochemical dissolution of crystalline silicon in HF-based solutions. The presence of HF in the etching solution leads to a hydrogen-terminated PSi surface (Si-H_x termination). This termination is very reactive and thus does not fully protect the optical and electronic properties of the freshly prepared PSi surface. The surface of a Si wafer, contacted on the back, is in contact with a solution containing HF acid. After applying a voltage (in the right direction) between the wafer backside contact and an electrode in the HF solution, a pore growth by Si dissolution starts,

provided certain key parameters are set correctly. Figure 6 is showing a schematic diagram of the PSi anodization circuit. The understanding of PSi formation still comes from the I-V relationships, and a basic knowledge of Si electrochemistry is essential to understand the fundamentals of pore formation [28, 29].

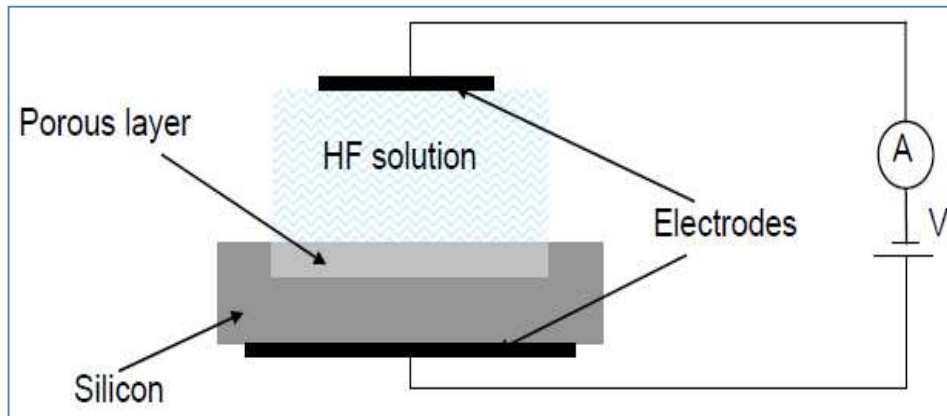


Figure 6. Schematic diagram of the PSi anodization circuit.

The fabricated pores allow the penetration of chemical or biological substances, liquids, cells, and molecules which give a potential to change the optical behavior of the original systems. These effects inspired research into different applications such like optoelectronic sensing and biomedical applications [30-32].

The open porous structure and the very large specific surface area of PSi are strong motivations for trying to introduce different kinds of materials inside the pores. The resulting composite structures open the door to new developments mostly in the field of light emitting devices and sensors based on Si [33].

On the other hand, this material is penetrated with a large amount of nanoscale pores resulting in a sufficient change of physical properties of this material in comparison with the initial Si. In particular, PSi is much more elastic and pliant than Si. Therefore PSi can be used as a buffer between Si substrate and a growing epitaxial film [34, 35].

1.8 Methods for SiNWs fabrication

As mentioned many times that numerous synthesis techniques have been currently developed for various types of nanomaterials to produce various and useful nanostructures. However, there is a large area to be improved, which is preparation of large-area of uniform nanostructure arrays, especially through controllable and facile approaches.

Because Si is a very important semiconductor material, SiNWs have attracted tremendous research interest because of their potential applications in the microelectronic industry. SiNWs are expected to work as building blocks and interconnect for nanoscale electronic and optoelectronic devices. SiNWs-based nanodevices such as biological sensors, field-effect transistors (FETs), and integrated logic circuits have been demonstrated as powerful examples in application. Currently, different methods have been utilized to produce SiNWs [36-39].

1.8.1 VLS growth mechanism to fabricate SiNWs

Coating a Si substrate with a thin film of gold (Au) and annealing the substrate in a vacuum chamber to obtain Au–Si catalyst particles. Then when a vapour-phase Si precursor is introduced at a substrate temperature above the eutectic point (the lowest temperature at which the Au–Si mixture will melt), the catalyst particles become supersaturated with Si and crystalline SiNWs will nucleate out of the melt and grow.

In this vapour–liquid–solid (VLS) growth mechanism, proposed by Wagner and Ellis, the Au catalyst particle, located at the tip of the nanowire, is in a liquid state during growth. This liquid particle serves as the preferential site for adsorption of the Si from the vapour precursor species. The metal nanoparticle form nanoscale droplets can be supersaturated

from the gas phase with Si containing species by e.g. chemical vapour deposition (CVD) or physical vapor deposition methods such as laser ablation molecular beam epitaxy (MBE) or electron beam evaporation (EBE) [40,41].

The schematic representation shown in Fig. 7 illustrates the VLS growth process as it occurs when a particle beam provides the growth species. Vaporized growth species “e.g. Si atoms or silane (SiH_4) molecules” reach the substrate surface is covered with metal nanoparticles.

The substrate temperature is held above the eutectic temperature of the alloy (Au-Si: 373°C). The liquid gold droplet can be supersaturated with Si atoms. Under the influence of a concentration gradient between the droplet surface and the droplet/nanowire interface, Si atoms diffuse to the interface to be incorporated into the SiNWs crystal. [40-43]

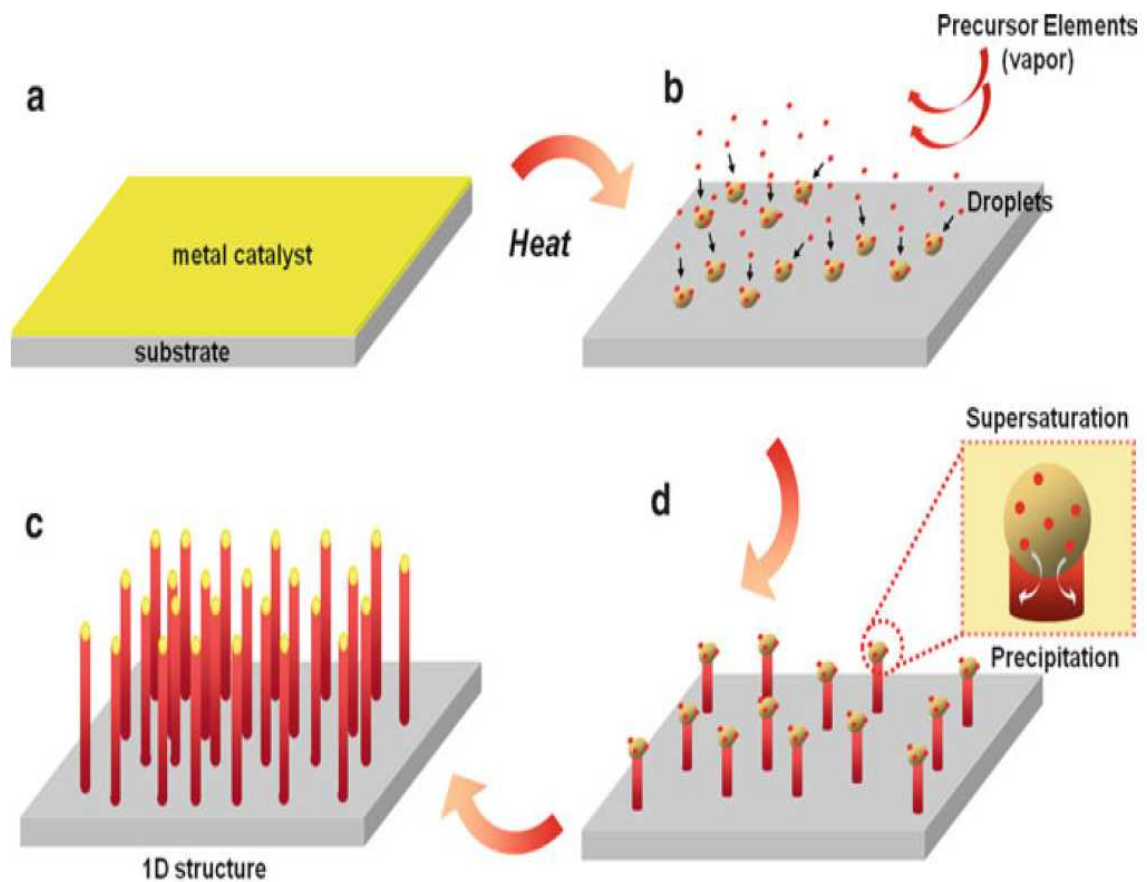


Figure7. Schematic drawing of the VLS process as it takes place in a PVD or CVD deposition experiment; first two steps yield the formation of gold droplets by heating of a continuous gold layer on a silicon substrate; third step shows Si atoms to reach the substrate and to be incorporated into the liquid Au-Si droplet above the eutectic temperature (Au-Si: 373 °C); and in the last one supersaturation of the Au-Si droplet with Si leads to growth of the SiNWs at a higher growth velocity than the continuous silicon layer in between the droplets takes place.

1.8.2 Metal-assisted chemical etching of Si

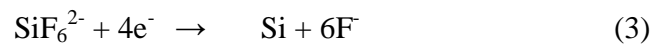
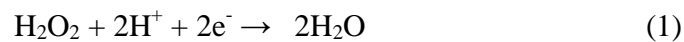
VLS approach gives high quality SiNWs but requires the use of hazardous silane gases at high temperature. Another method could be used as alternative method which is metal-assisted chemical etching. Briefly, in metal-assisted chemical method SiNWs could be fabricated when Si wafers undergo electrochemical reaction in HF solution. The formation mechanism will be discussed later. Many reasons could be mentioned to know advantages of

metal-assisted chemical etching over VLS-based growth to fabricate SiNWs. These reasons could be mentioned as in the following explanation:

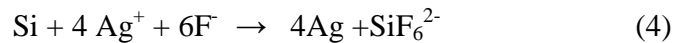
- Metal-assisted chemical etching is a simple and low-cost method for fabricating various Si nanostructures with the ability to control various parameters (e.g., cross-sectional shape, diameter, length, orientation, doping type, and doping level). Almost all procedures can be accomplished in a chemical lab without expensive equipment.
- Metal-assisted chemical etching enables control of the orientation of Si nanostructures (e.g., nanowires, nanopores) relative to the substrate. In contrast, in VLS-based growth of SiNWs, the crystallographic orientation of SiNWs depends upon the diameter of nanowires. [44- 45]
- Due to the existence of equivalent crystallographic directions, it is difficult to grow epitaxial SiNWs with uniform orientation relative to the surface of the Si substrate. For example, the growth of epitaxial and vertical nanowires on (110) substrates or nanowires on (100) substrates has not yet been accomplished without the use of an appropriate template. On the other hand, electrochemical etching is well-known to occur anisotropically along $\langle 100 \rangle$ directions. In contrast, although the metal-assisted chemical etching is intrinsically anisotropic, methods have been developed to control the etching direction, enabling the fabrication of vertically aligned SiNWs on (100) and non-(100) substrates or in certain inclined directions on non-(100) substrates [45- 47].
- VLS-based methods can only be used to grow nanowires with circular cross-sections, while metal-assisted chemical etching is much more flexible and can be used to make higher surface-to volume ratio structures [48- 49].

- The crystalline quality of SiNWs fabricated by metal-assisted etching from single crystalline substrates generally is high. Although their surfaces are typically rougher than those of nanowires obtained by VLS growth, the nanowires do not contain the obvious crystallographic defects. Dry etching (e.g., RIE) tends to introduce defects in a region close to the etched Si surfaces. Also it was found that there is no obvious limitation on the size of features fabricated by metal-assisted chemical etching [50, 51].

The mechanism for the Formation of SiNWs Arrays could be understood through Si electrochemical reaction in HF solution according to three half-reactions.



Etching of Si includes two main reactions as shown below:



A large amount of Ag^+ in the aqueous solution and Si in the bulk substrate force these reactions occur repeatedly and continuously. The initial reduction of Ag^+ forms Ag nanoparticles on the Si wafer surface, thus delimiting the spatial extent of the oxidation and etching process. Further reduction of Ag^+ occurs on the nanoparticles, not the Si wafer, which becomes the active cathode by electron transfer from the underlying wafer. The vertical alignment is contributed to the longitudinal falling down of the Ag particles from the surface to the bulk of Si substrates, along with continuous dissolution of Si in the

vicinity of Ag particles. The mechanism could be clearly understood using the following illustration [52].

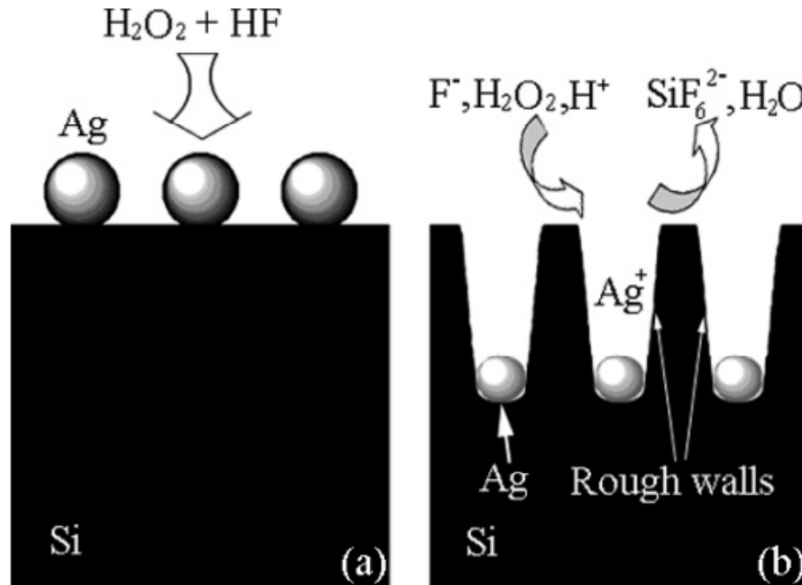


Figure 8. Mechanism of SiNWs formation during metal-assisted chemical etching of Si. Longitudinal falling down of Ag particles from the surface to the bulk Si occurred to form SiNWs.

1.9 Conducting Polymers

Generally the intense attention and research on conducting polymers have resulted with number of practical applications because of their distinct electronic properties, diversity, potentially low cost, and ease of fabrication.

Intrinsically conducting polymers, including polyacetylene, polyaniline (PANI), polypyrrole, polythiophene, poly(p-phenylene-vinylene), etc., are termed organic polymers that possess the electrical, electronic, magnetic, and optical properties of a metal. The retaining the mechanical property, process ability, etc... commonly associated with a conventional polymer, and more commonly known as “synthetic metals” [26, 53].

1.9.1 PANI and its Derivative

PANI and its derivatives have attracted significant interest as electronic material because of its high capacity, good conductivity, unique doping–dedoping process, and ease of synthesis. PANI is a unique among the conducting polymers in its doping characteristics. Rather than changing its oxidation state (i.e. carrier density) by addition or removal of electrons or doping. This is accomplished by removal or addition of protons using strong bases (e.g. ammonium hydroxide) or protonic acids (e.g. hydrochloric or sulfuric). The net effect is similar: electrons in partially filled frontier orbitals are responsible for carrying the current; overall charge neutrality is maintained by the protons bound to the backbone nitrogen atom and by the anion of the protonic acid [54].

One of the most active areas is polymer nanotechnology owing to the size of polymer chains. Advancement of nanotechnology tools has provided a rare opportunity to investigate individual chains of polymers. On the other hand, polymers as a member of soft matter family have incredible flexibility for the preparation of various nanostructures, particularly for nano-devices. Recently, the interests in nano-structured PANI, especially, PANI nanofibers, have increased extensively [54, 55].

PANI is now accepted to have the general polymeric structure shown in Fig. 9 (a): In the generalized base form, $(1 - y)$ measures the function of oxidized units. When $(1 - y) = 0$, the polymer is commonly known as a leucoemeraldine base (reduced form). The fully oxidized form, $(1 - y) = 1$ is referred to as a pernigraniline base. The value of y varies from 0 to 1, but the percentages of carbon, hydrogen and nitrogen will be almost the same [56-58].

Poly (Ortho-Toluidine) (POT) is a PANI derivative which contains the – CH₃ group in the ortho position of the aniline monomer among the ring – substituted PANI derivatives as shown in Fig. 9 (b) [59].

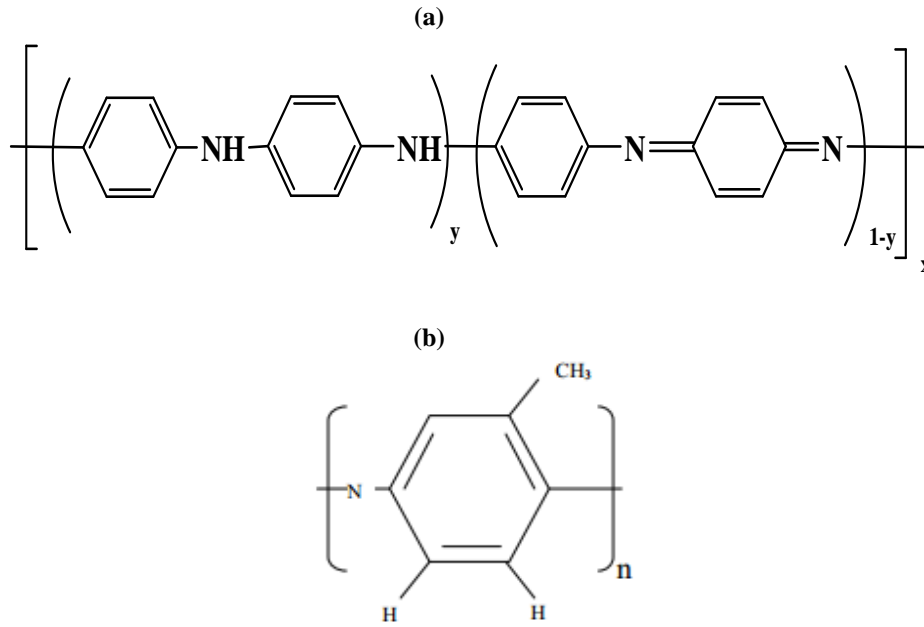


Figure 9. Structure of PANI and Its derivative POT

1.10 Si /Conducting Polymers Heterojunctions

Heterojunction devices have been drawn a great attention in recent years mainly due to their use in optoelectronic field [59]. The properties of these heterojunction are of very importance when they are used as FET, bipolar transistor, light emitting diode and lasers. The heterojunction diode could give a great potential for their use in sensor applications [60].

The fabrication of such heterojunction diode taking its impact from the advantages of the conducting polymers like diversity, easy synthesis, inexpensive thin film production by spin coating or dip coating, and good mechanical properties (flexibility, resistance, elasticity) and are processable. Moreover, the electrical conductivity of these polymers can

be changed from isolating to metallic by the chemical or electrochemical doping process. Their electrochromic and luminescent properties are quite similar to inorganic semiconductors. Also PSi and SiNWs were found to be perfect nanostructures to host the polymerization of conducting polymers.

Also PSi and SiNWs provide a large surface area within a small volume that beside its unique properties mentioned before which enable to fabricate novel electronic and photovoltaic devices. Even we should remember that the method of synthesis could help to optimize the individual fabrications and also help to optimize the resulted heterojunction. These heterostructures could help to fabricate heterojunction diodes, sensors, a hybrid inorganic/organic solar cell with considerable efficiency etc...

1.11 Metal Nanofabrications and Plasmonics

Today the electronic circuits can be fabricated at dimensions below 100 nm. On the other hand, the wavelength of light used in photonics circuits is on the order of 1000 nm. When the dimensions of an optical component become close to the wavelength of light, the propagation of light is obstructed by optical diffraction. This means that optical fibres and electronic interconnects are difficult to combine within the same circuit and even by using the photonic crystal by its minimal confinement is nevertheless restricted to the diffraction limit $\lambda/2n$ of the light [61, 62].

The diffraction limit can only be overcome if the optical mode is somehow converted into a non-radiating mode that is confined to dimensions smaller than the diffraction limit. The further progress will require the development of a radically new chip-scale device technology that can facilitate information transport between nanoscale devices at optical

frequencies and bridge the gap between the world of nanoscale electronics and microscale photonics [63, 64]

Plasmonics or surface plasmon (SPs) based circuits, explores how electromagnetic fields can be confined over dimensions on the order of or smaller than the wavelength of light. An interaction processes between electromagnetic radiation and conduction electrons at metallic interfaces or in small metallic nanostructures, leading to an enhanced optical near field of sub-wavelength dimension. The resonant interaction between electron-charged oscillations near the surface of the metal and the electromagnetic field of the light creates the SPs.

SPs are electromagnetic waves that occur at a metal/dielectric interface, where the conducting free electrons interact with the electromagnetic field of light resulting in collectively oscillations of these electrons. SPs are bounded to the metallic surface with exponentially decaying fields in both neighboring media. So plasmonics can merge electronics and photonics at the nanoscale offering a solution for the size compatibility problems and also can offer a solution to such diffraction limit problem. So plasmonics nanostructures are having both the capacity of photonics and the miniaturization of electronics [65-67].

Figure 10 is showing a schematic representation of an electron density wave propagating along a metal/dielectric interface. The charge density oscillations and associated electromagnetic fields are called surface plasmon polariton (SPP) waves. The exponential dependence of the electromagnetic field intensity on the distance away from the interface is shown on the right. This feature of SPs provides the possibility of localization and the guiding of light in subwavelength metallic nanostructures. Also the futures of SPs could be

used to construct miniaturized optoelectronic circuits with subwavelength components. Such plasmonic optoelectronic circuits, or plasmonic chips, will consist of various components such as waveguides, switches, modulators, and couplers, which can be used to carry the optical signals to different parts of a circuit [65, 67].

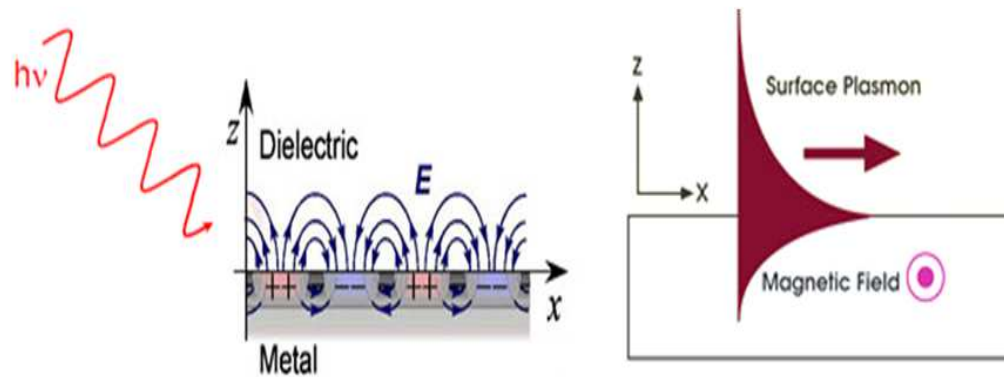


Figure 10. SPs generation when light beam striking a metal. The figure shows a schematic representation of an electron density wave propagating along a metal/dielectric interface. The charge density oscillations and associated electromagnetic fields are called surface plasmon polariton (SPP) waves.

1.11.1 Plasmonics & Refractive Index Change

Detecting the small and minor refractive index change is an important as refractive index sensing has a wide range of applications in areas such as chemistry, physics, and biomedical engineering. Surface plasmon resonance (SPR) spectroscopy is one method that has gained popularity to measure bimolecular interactions without the need for labels [68-71].

Localized surface plasmon resonance (LSPR) spectroscopy offers easy sensor fabrication and inexpensive instrumentation while retaining all the advantages characteristic of label-free surface sensing, in some cases even demonstrating improved capabilities over other techniques.

Surface plasmon resonance (SPR) spectroscopy is widely applicable for biosensing due to the simple, low-cost instrumentation, and the variety of signal transduction platforms that can be used. LSPR biosensing makes use of the fact that plasmonic nanoparticles and other plasmonic structures are sensitive to local changes of refractive index and hence no labelling of analytes is needed. This produces very large shifts in the LSPR spectrum, which are typically much larger than those observed from changes in refractive index [72-75].

1.12 SiNWs-Based Surface-Enhanced Raman

Surface-enhanced Raman scattering (SERS) is a powerful spectroscopy technique that can provide non-destructive and ultrasensitive characterization down to single molecular level, comparable to single-molecule fluorescence spectroscopy. This technique provides greatly enhanced Raman signal from Raman-active analyte molecules that have been adsorbed onto certain specially prepared metal surfaces. The importance of SERS is that it is both surfaces selective and highly sensitive whereas normal Raman spectroscopy is neither. Normal Raman spectroscopy is ineffective for surface studies because the photons of the incident laser light simply propagate through the bulk and the signal from the bulk overwhelms any Raman signal from the analytes at the surface [76, 77].

The commonly used SERS substrates, such as silver nanoparticles (AgNPs) colloid, AgNPs array, and AgNPs-coated SiNWs, rely on interparticles gaps with a spacing of 10 nm or less as the enhancing units, or so-called “hot spots”. At each hot spot, both excitation and Raman scattering light can couple with SPs of the metal nanoparticles and be electromagnetically enhanced [76, 78].

SiNWs could be better than LSPR of the separated nanospheres as practical SERS detection requires spot-to-spot reproducibility, or similar SERS spectra at different spots on the same substrate which could be easily achieved in case of Silver-coated SiNWs. Local changes cannot be monitored precisely with such mobile NPs. Therefore, integrating the advantages of both SiNWs and SERS is expected to lead to the development of a highly efficient optical endoscope for intracellular detection. AgNPs-coated SiNWs complex yields a high enhancement factor value of $\sim 10^{10}$. This resultant high-efficiency SERS-active substrate is further applied as biosensor for detecting DNA with high sensitivity and specificity [76-81].

1.13 Objective/approach and Summary of chapters

The main objectives drafted for this research of the presented thesis could be described as in the following main points:

- Learn to prepare, develop and design certain nano-scale fabrications.
- Learning different methods to characterize and study the properties of such nanostructures.
- Simulation of plasmonic nanostructures.
- Providing new design and also finding new low cost processing of some nanofabrications compared complex and high cost methods.
- Finding out novel and useful applications for some nanoscale structures.

The nanoscale structures that have been investigated in this research here are including:

1. PSi and SiNWs
2. The conductive polymer PANI and its derivative POT in nano scale.

3. Plasmonic nanosensor based on a square resonator.

The first and second nano-scale fabrications were helped to fabricate a hybrid inorganic/organic heterojunction diode with low-cost processing. PSi and SiNWs were fabricated by a simple and low cost wet chemical etching. PSi and SiNWs served to host the polymerization of the conducting polymers to form heterojunction diodes have characteristics similar to P-N junction or Schottcky diode.

Such heterojunction diodes are taking their impacts from the advantages and good properties of PANI and POT nanostructures such like diversity, easy synthesis, inexpensive thin film production by spin coating' or 'dip coating'. Also PSi and SiNWs are perfect nanostructures to host the polymerization of NPANI or NPOT. Also PSi and SiNWs provide a large surface area within a small volume that beside its unique properties mentioned before which enable to novel electronic and photovoltaic devices. Also it is expected that such heterostructures could help to design a hybrid inorganic/organic solar cell with considerable efficiency depending on the unique properties of SiNWs.

In chapter 2, NPANI/p-type PSi heterojunction films were chemically fabricated via in-situ polymerization. The composition and morphology of the nano-polymer were confirmed using Fourier transform infrared, scanning electron microscopy (SEM), UV-visible and X-ray diffraction techniques. I-V measurements were performed at different temperatures in dark conditions, enabled the calculation of many parametrs of the fabricated heterojunction such ideality factor, barrier height and series resistance.

In chapter 3, the fabrication method of SiNWs by metal-assisted chemical method based on chemical etchant solution contains $\text{KMnO}_4/\text{AgNO}_3/\text{HF}$. The composition and morphology of the nano-polymer were confirmed using Fourier transform infrared, scanning

electron microscopy (SEM), UV-visible, Transmission electron microscopy and X-ray techniques. NPOT/p-type SiNWs heterojunction films were chemically fabricated via in-situ polymerization. We provided SEM measurements of the fabricated SiNWs before and after POT deposition. I-V measurements, performed at room temperature in dark conditions. From I-V characteristics we were able to calculate different parameters of the fabricated heterojunction. Different calculation methods were applied and compared to confirm the different parameters of the fabricated heterojunction.

The third point here in our research work is relating to a design of plasmonic nanosensor to detect the minor changes of refractive index. The proposed nanosensor may open the door to act as a compact sensor can be easily utilized for integrated on chip system for lab-on-chip applications. Some trials were done to fabricate the real structure. We believe that verifying our proposed nanosensor through optimizing real structure and also experimental characterization will add a high impact to the FDTD simulation done. Optimizing the real structure and the experimental characterization could pave way for future research endeavors.

In Chapter 4, a novel integrated plasmonic nanosensor based on square resonator was proposed and analyzed. The detection performance of the proposed device has been numerically verified by finite-difference time-domain (FDTD) simulations. The spectral sensitivity and the detection limit of the proposed sensor were determined. Sensitivity analysis of the Proposed Sensor and the effect of fabrication imperfections in the design parameters have also been investigated.

For the last research point is relating to Silver-coated SiNWs for SERS applications take its importance from fabricating SiNWs by chemical wet etching and normal

evaporation of silver thin film upon the fabricated SiNWs. Some publications discussed similar research but they usually focused on producing by some high cost methods such like nanolithography. We are trying to use a low cost wet chemical etching as to fabricate SiNWs. Till the moment, we have some promised results but still need more analysis. So we left this research point for a future research which will be done in the near future. Only the concept of using SiNWs in SERS applications was mentioned in chapter 1(General introduction) and our idea of to fabricate SERS device to enhance Raman signals of a molecule such like Rodamine 6G (R6G) was mentioned in chapter 5 (General conclusions and future work).

CHAPTER 2

Electrical Characterization of NPANI/PSi Heterojunction at High Temperatures

ABSTRACT..... NPANI/p-type PSi (NPANI/PSi) heterojunction films were chemically fabricated via in situ polymerization. The composition and morphology of the nanopolymer were confirmed using Fourier transform infrared, scanning electron microscopy, UV-visible, and transmission electron microscopy techniques. The results indicated that the polymerization took place throughout the porous layer. The I-V measurements, performed at different temperatures in dark, enabled the calculation of ideality factor, barrier height, and series resistance of those films. The obtained ideality factor showed a nonideal diode behavior. The series resistance was found to decrease with increasing temperature.

2.1 Introduction

Intrinsically conducting polymers, including polyacetylene, PANI, polypyrrole, polythiophene, poly(p-phenylene-vinylene), etc., are termed organic polymers that possess the electrical, electronic, magnetic, and optical properties that are close to that of metals. Besides, they keep the same mechanical properties, processability, etc. that are commonly associated with conventional polymers. Therefore, these polymers are commonly known as “synthetic metals” [53].

PANI is one of the most important classes of conjugated polymers that possess excellent electronic, optical, and redox properties. PANI is unique among the conducting

polymers in its doping characteristics. Rather than changing its oxidation state (i.e. carrier density) by addition or removal of electrons, doping is accomplished by removal or addition of protons [54], using strong bases (e.g. ammonium hydroxide) or protonic acids (e.g. hydrochloric or sulfuric). The net effect is similar: electrons in partially filled frontier orbitals are responsible for carrying the current; overall charge neutrality is maintained by the protons bound to the backbone nitrogen atom and by the anion of the protonic acid.

It is important to mention that, one of the most active areas is polymer nanotechnology owing to the size of polymer chains. Advancement of nanotechnology tools has provided a rare opportunity to investigate individual chains of polymers. On the other hand, polymers as a member of soft matter family have incredible flexibility for the preparation of various nanostructures, particularly for nano-devices. Recently, the interests in nano-structured PANI, especially, PANI nanofibers, have increased extensively [54, 55].

Also, doping PANI with acids improves its environmental stability and conductivity [82,83]. PANI, as a conducting polymer, has been used in a plethora of practical applications such as battery electrodes [84,85], electrochromic devices [86,87], photoelectric cells [88], light-emitting diodes [89,90], Solar cells [91,92], Energy storage [93], electromagnetic interference shielding [94], electrostatic discharge [95], biosensors [96,97] and anti-corrosive coatings [98,99].

Various methods are available for the synthesis of PANI. However, the most widely used two techniques are electrochemical and chemical oxidative polymerization methods [100]. The chemical method is especially preferred as it can be used to produce PANI for large scale applications. Recently, there has been a great interest in the fabrication and assembly of nano-structured PANI, especially PANI nanofibers, [101]. Since the first report

by Huang et al. [102] that PANI nanofibers can be easily synthesized by an interfacial polymerization, many template-free methods have been established. For instance, PANI nanofibers were easily prepared by rapidly mixing acidic aqueous solutions of aniline and ammonium peroxydisulphate (APS), [103]. Also, NPANI has been synthesized using dodecylbenzylsulfonic acid, which was successfully electrodeposited on the surface of glassy carbon electrodes to form nanostructured films suitable for heterogeneous catalysis applications [104].

As another class of important materials, PSi is commonly prepared by chemical or electrochemical dissolution of crystalline silicon in HF-based solutions. Electrochemically fabricated PSi has a set of unique properties, especially the open porous structure and the enormous surface area. Moreover, PSi is much more elastic and pliant than the starting Si and thus can be used as a buffer between Si substrates and growing epitaxial films [105,106].

Recently, there has been a great interest in the fabrication and assembly of organic/inorganic semiconductor heterostructures, which have been found promising in many applications, opening the door to new developments. For example, heterojunctions made of a thin layer of a molecular semiconductor deposited on the surface of an inorganic semiconductor substrate, such as Si, GaAs, or InP, have been found to form rectifiers with characteristics similar to ideal p–n junctions [107,108].

Of special interest, PANI/Si heterojunction has recently been studied thoroughly. [75] A fabricated heterojunction solar cells using PANI on crystalline Si recently studied [93,109,110]. It was found that, the open-circuit voltage to increase with increasing the conductivity of the PANI film, saturating at a value of 0.51 V. Dirani et al. [111] fabricated

heterojunction diodes using poly(o-methoxyaniline)/PANI and amorphous/microcrystalline Si structures. They showed a dependence on the polymer doping level. Regarding the use of PSi, Chiboub et al. successfully prepared a PANI/PSi hybrid structure by oxidative chemical/electrochemical polymerization of an aniline-terminated PSi surface in the presence of aniline monomer in solution. The results suggested that the PANI was covalently grafted onto the PSi surface, and that the polymerization took place throughout the porous layer.

The resulting PANI/PSi hybrid interfaces showed a high chemical stability and good electrical properties [111]. Betty [112] presented an easy and inexpensive method for the fabrication of highly sensitive and specific immunosensor based on PANI/PSi heterojunction.

The PANI/PSi sensor was able to detect analyte-antibody interactions, while being reusable. A heterojunction between PSi and water-soluble copolymer of PANI was fabricated by Wan [113], which showed rectifying characteristics that were enhanced with decreasing the degree of sulfonation and the thickness of the copolymer.

As the operating temperature of the devices made of such heterojunctions is a determinant factor of their efficiency, Aydogan et al. [114] studied the I–V characteristics of Au/PANI/PSi/Al heterostructure in a wide range of temperatures (90–300 K). They showed a decrease in the barrier height (BH) and an increase in the ideality factor (n) with decreasing temperature. The refractive index shows an anomalous dispersion in the absorption region and a normal behavior in the transparent region. Therefore, more studies are needed to evaluate the performance of such heterojunctions at different temperatures.

Herein, we demonstrate the in-situ chemical fabrication of nano-PANI/PSi heterojunction films and their characterization using FTIR, UV-Visible, X-Ray, SEM and TEM techniques. The I-V characteristics of the films are studied at different temperatures (298–398K) and discussed based on the thermionic model. The electronic parameters (eg. n , BH and resistance) of the fabricated heterostructures are also determined.

2.2 Preparation of PSi substrates

Materials

Aniline (Riedel-de Haën, puriss grade) was distilled twice under atmospheric pressure and over zinc dust before use. Ammonium peroxydisulfate (APS) (WINLAB, UK) and cetyltrimethylammonium bromide (CTAB) (Fluka) were used without further purification. Sulfuric acid (H_2SO_4) 96%, hydrogen peroxide (H_2O_2) 30% (Sigma-Aldrich), hydrofluoric acid (HF) 47-51% (Fluka), ethanol and methanol were used as received.

Double-side polished p-type Si(100) wafer (boron-doped, 5–10 Ω cm resistivity) was first cleaned in 3:1 concentrated H_2SO_4/H_2O_2 for 5 min at 80 °C and then sonicated in deionized water for 10 min. Consequently, the wafer was rinsed in acetone to remove the cleaning residue and acts as a further cleaning solvent, after that the wafer was immersed in methanol for 3 min. to remove any acetone residue. Finally, the wafer was rinsed in deionized water for 3 min. to remove methanol residue. The clean wafers were immersed in HF: H_2O (1:10) solution for 20 s at room temperature to remove the native oxide. The hydrogen-terminated surfaces were electrochemically etched in a 1:1:3 (by volume) solution of HF: ethanol: H_2O for 15 min. After etching, the samples were rinsed with ethanol and de-ionized water, and then dried under a stream of dry nitrogen prior to use.

2.3 Preparation of NPANI / PSi heterojunction

CTAB (0.05 g, 0.69 mM) was dissolved in doubly deionized water (40 ml) and stirred at room temperature. Aniline (0.05 M) was added to the CTAB solution and stirred for an additional one hour at room temperature (15 ± 1 °C). APS solution (0.0625 M) dissolved in deionized water (40 ml) was added to aniline solution at room temperature. 5 ml of this mixture were then taken and be poured carefully on the surface of PSi wafer. The remaining solution (75 ml) was left to complete reaction. The originally colorless mixture turned blue and later became dark green. The resultant green color content was allowed to stand for 15 h without being disturbed. The solid mass was filtrated and washed with distilled water and methanol several times until the filtrate became colorless. The solid product was then dried in a vacuum oven at 60 °C for 48 h to be ready for analytical measurements. Also, the wafer was washed with deionized water several times.

2.4 Characterization

1- **UV-VIS spectra:** PANI films were obtained during the polymerization of aniline on rectangular glass slides. These slides were introduced into the reaction vessel before the polymerization starts. Once the reactants were introduced to the vessel, the film grows onto the glass support simultaneously. After time intervals during the polymerization process, the glass supports were removed from the reaction mixture and rinsed with deionized water and finally dried. These supports coated with PANI films were used to for the UV-visible absorption measurements. The absorption spectra were recorded with a Shimadzu UV-2101 DC spectrophotometer. Uncoated glass supports were used as references.

2- FTIR measurements: FTIR spectra of the PANI samples dispersed in a KBr pellet were obtained using a JASCO 410 instrument.

3- Scanning Electron Microscope (SEM): A morphological study was performed via SEM observation of the cross section of PANI nanoparticles using a SEM (model JOEL14775) at 10 kV with gold coating on the samples.

4- Transmission electron microscopic analysis (TEM): The nano-structure of deposited PANI film was confirmed by TEM technique. TEM measurements were taken using a JEOL JEM -2000EX microscope at an accelerating voltage of 100kV. For TEM observation, the PANI nanoparticles were placed onto a carbon film supported by a copper grid.

5- I–V measurements: Current–voltage (I–V) characteristics of the heterojunction films were studied at different temperatures (298–398K) using Keithley 2400 source meter. The temperature was continuously monitored by using thermocouple close to the sample.

2.5 RESULT AND DISCUSSION

2.5.1 Morphological, Structural and Optical Properties:

SEM was used to investigate surface morphology of the NPANI synthesized in CTAB micelles. In the SEM micrographs Fig. 11 (a) and (b), rod-like shape nanostructures can be distinguished Fig. 11 (b) with diameters ranging from 30-50 nm, which is in good agreement with the TEM results shown in Fig. 12.

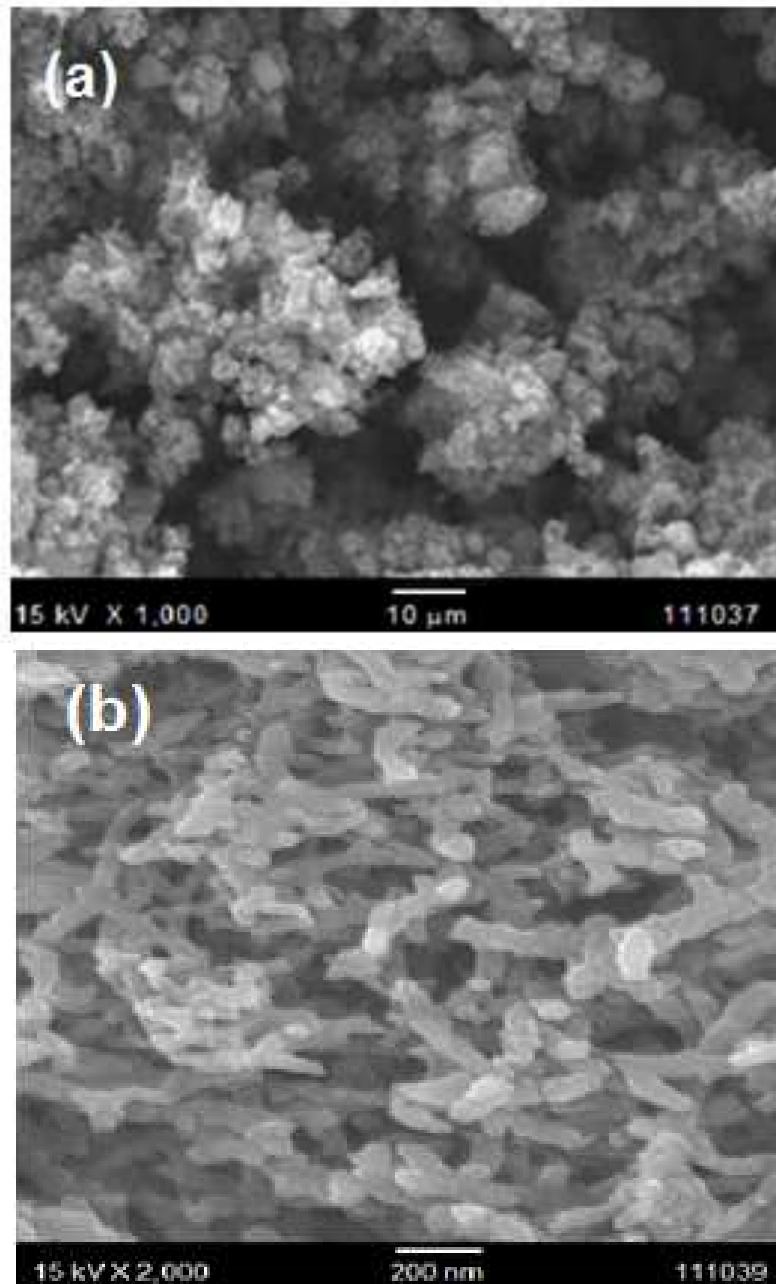


Figure 11. NPANI SEM micrographs and rod-like shape nanostructures.

The obtained diameters are much smaller with very narrow size distribution compared to those reported by Guo and Zhou who synthesized PANI nanofibers with diameters in the range 80–100 nm by electrochemical polymerization [115] and electrospun PANI with diameters of 20–150 nm [116]. However, these are larger than PANI nanofibers

synthesized using aluminum oxide template (20–40 nm in diameter) [117] and FeCl_3 as an oxidant (16–23 nm in diameter) [118].

In our study, the micelles formed by CTAB and aniline might act as templates for the formation of the obtained self-assembled PANI nanorods. Upon the addition of APS, polymerization takes place only at the micelle/water interface. In addition, as PANI is a rigid molecule, the micelles have a tendency to elongate in the direction of the polymer chain during the polymerization process resulting in the observed PANI nanorods.

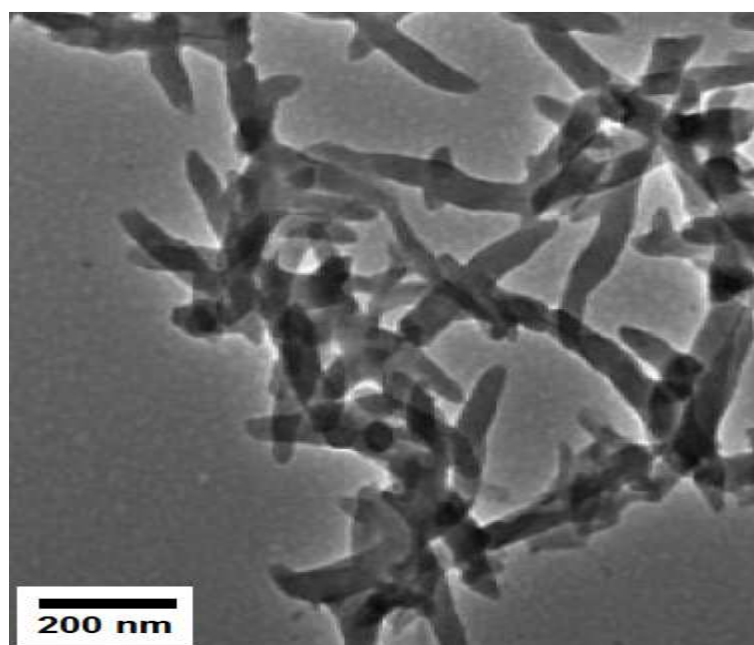


Figure 12. TEM micrograph of synthesized rod-like PANI

Figure 13 represents the FTIR spectrum of the fabricated NPANI film. The characteristic sharp band appeared at $1220\text{--}1020\text{ cm}^{-1}$ can be assigned to the C-N tertiary aromatic vibration, while the bands located at $1360, 1250, 1340$ and 1310 cm^{-1} are due to the C-N primary and secondary vibrations. The sharp characteristic band at $3450\text{--}3200\text{ cm}^{-1}$ is due to the N-H stretching vibration. Moreover, the bands at 1550 and 1475 cm^{-1} are due to

the presence of quinoid structure and the band obtained at 1240 cm^{-1} can be related to the C–N stretching mode for benzenoid ring. The band at 810 cm^{-1} is a characteristic of a p-substituted aromatic ring proposing that polymerization has proceeded in a “head to tail” form.

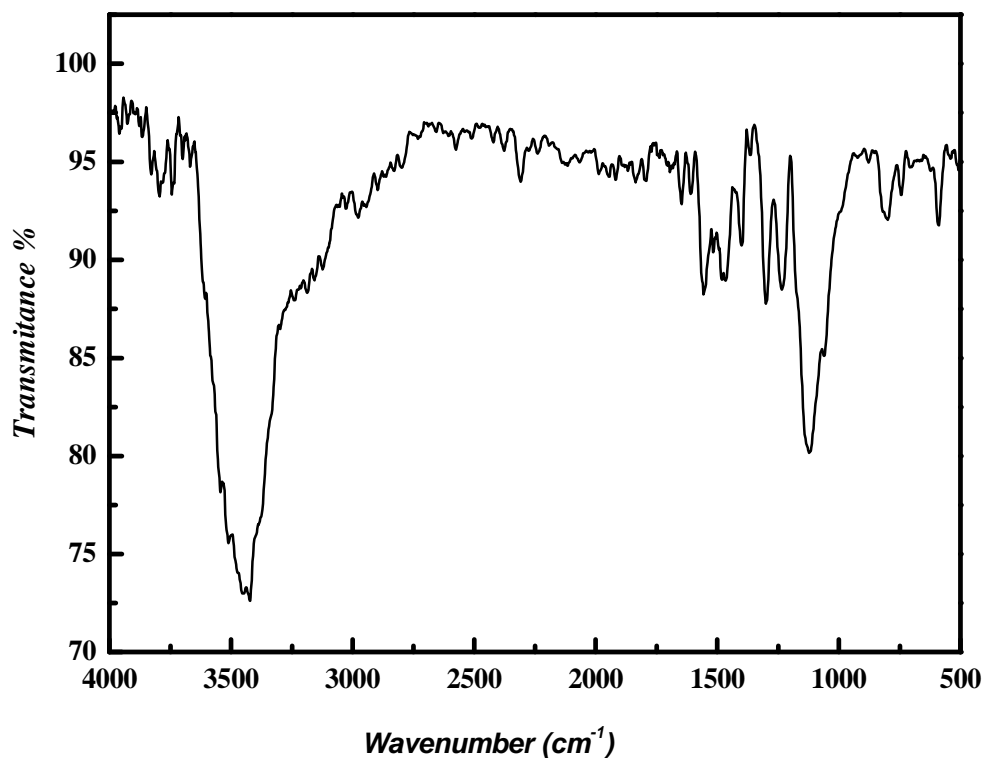


Figure 13. FTIR spectrum of the synthesized NPANI. This figure represents the FTIR spectrum of the fabricated NPANI film. The characteristic sharp band appeared in some positions while other bands located at different position. Generally FTIR could give some useful information such proposing that polymerization has proceeded in a “head to tail” form.

For more justification, Fig. 14 shows the UV–visible spectrum of NPANI film deposited on a glass substrate. It can be shown that the spectrum shows two bands; one at 345 nm corresponds to the π - π^* transition of the benzenoid rings and another broad band at 795 nm corresponds to the quinone structure.

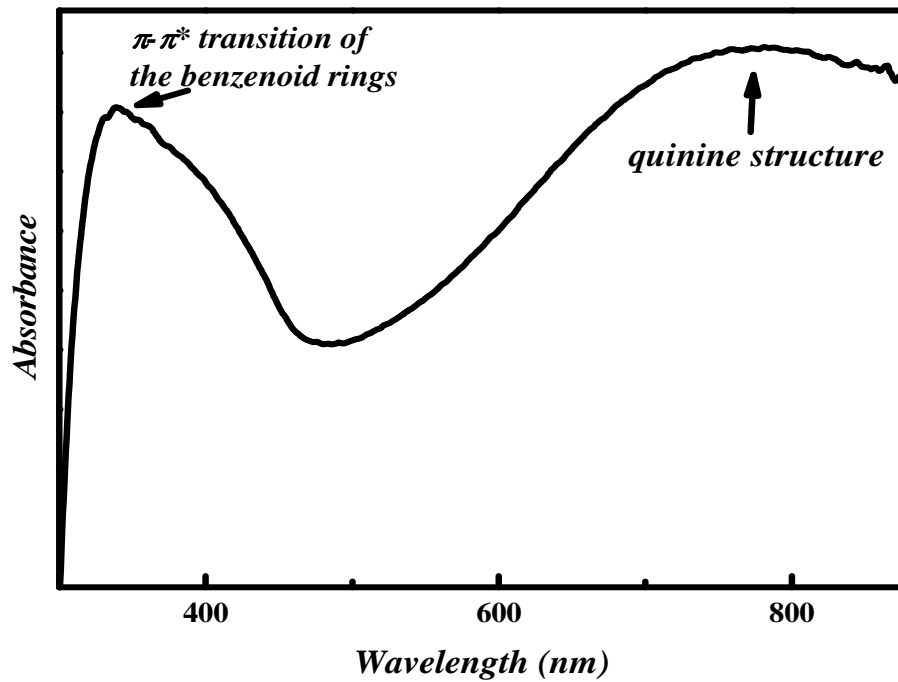


Figure 14. UV-visible spectrum of the synthesized NPANI.

The figure shows that the UV-visible spectrum of NPANI film deposited on a glass substrate. It can be shown that the spectrum shows two bands; one at 345 nm corresponds to the π - π^* transition of the benzenoid rings and another broad band at 795 nm corresponds to the quinine structure.

2.6 I-V measurements

According to the thermionic emission model, for a metal/semiconductor (M/S) or metal/polymer (M/P) contact [119-122], the I-V characteristic under the forward and reverse bias voltages through an SBD can be represented as:

$$I = I_0 \left[\exp \left(-\frac{qV}{nkT} \right) - 1 \right] \quad (1)$$

where I is the forward diode current, I_0 is the reverse saturation current, q is the electron charge, V is the applied bias voltage, k is the Boltzmann's constant, T is the absolute temperature, and η is the ideality factor. The reverse saturation current (I_0) can be obtained by extrapolating the linear portion of the forward bias in the $\ln I$ - V plot to the intercept point on the current axis at zero-bias ($V = 0$) and is given by:

$$I_o = AA^* T^2 \exp\left(-\frac{q \Phi_B}{kT}\right) \quad (2)$$

where A is the effective diode area, A^* is the effective Richardson constant ($32 \text{ A/cm}^2 \text{ K}^2$ for p-type Si), and Φ_B is the zero-bias barrier height [119-122].

The ideality factor (η), a dimensionless quantity, is a measure of the conformity of the diode behavior to pure thermionic emission. It is introduced to account for the deviation from the thermionic emission diffusion theory. η can be determined from the slope of the straight line region of the $\ln I$ - V plot and can be represented as:

$$\eta = \frac{q}{kT} \left(\frac{dV}{d(\ln I)} \right) \quad (3)$$

For an ideal diode, η is unity. However, values greater than unity are usually observed and attributed to many factors such as the presence of interfacial thin native oxide layer, series resistance, etc.. Also, barrier inhomogeneity has been used to explain the higher values of the ideality factor [89]. For the estimation of the barrier height (Φ_B), one may also make use of the Richardson plot of saturation current, i.e.

$$\ln\left(\frac{I_o}{T^2}\right) = \ln(AA^*) - \frac{q \Phi_{Bo}}{KT} \quad (4)$$

Based on the above analysis, the I - V measurements were done for the NPANI/PSi films to determine the transport mechanism in such diodes. Figure 15 shows the I - V characteristics under the forward and reverse bias conditions at different temperatures in the range 298–373 K. The curves are similar to that of a metal/semiconductor (MS) Schottky barrier (SB). Asymmetrical I - V characteristic under the forward and reverse bias voltages is observed. In the low voltages range, the forward current increases with increasing temperature indicating a negative resistance temperature coefficient. The observed

exponential dependence may be due to the formation of a depletion region between NPANI layer and PSi film.

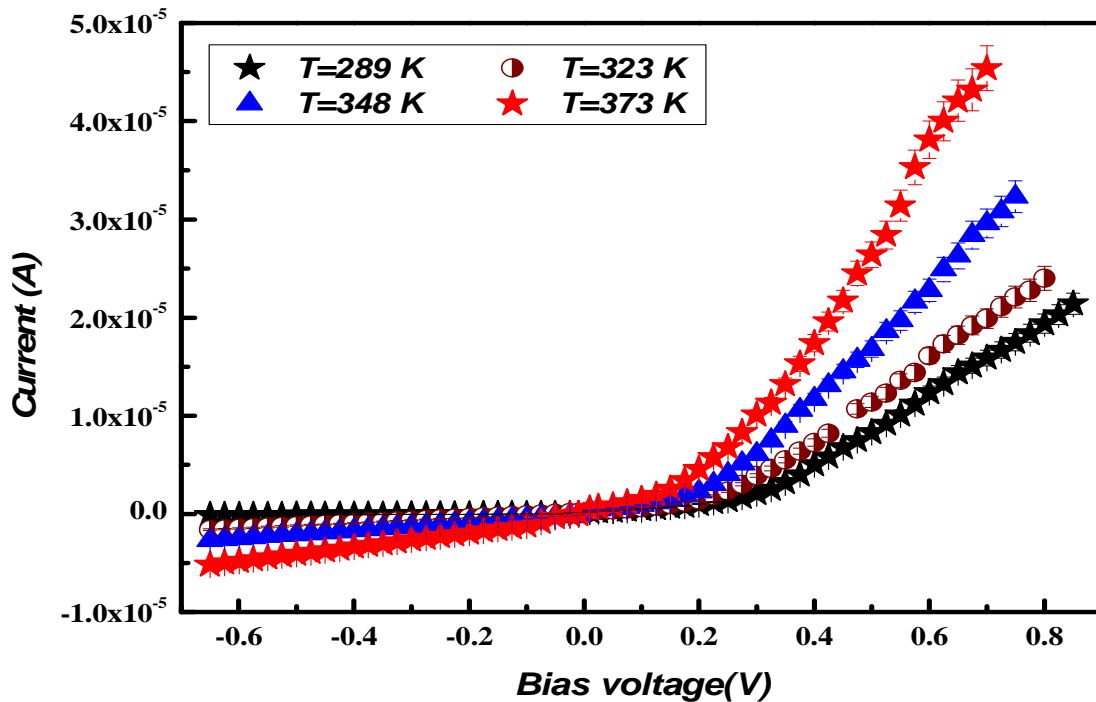


Figure 15. I-V characteristics of NPANI/PSi heterojunction at different temperatures.

Strong rectifying characteristics could be shown. I-V characteristics under the forward and reverse bias conditions at different temperatures in the range 298–373 K. The curves are similar to that of a metal/semiconductor (MS) Schottky barrier (SB). Asymmetrical I-V characteristic under the forward and reverse bias voltages is observed. In the low voltages range, the forward current increases with increasing temperature indicating a negative resistance temperature coefficient. The observed exponential dependence may be due to the formation of a depletion region between NPANI layer and PSi film.

It is observed that the junction exhibits strong rectifying characteristics in dark showing an n-p heterojunction as diode behavior. This behavior can be attributed to the barrier at the interface that limits the forward and reverse carriers flow across the junction, where the built-in potential could be developed [119].

The forward I-V characteristics of NPANI/PSi SB diode, according to thermionic emission theory [120], are expressed by eq. (1). As can be seen in Fig. 11, the forward bias

of the structure current is an exponential function of the applied bias voltage in the intermediate voltage regime ($V \geq 0.35$ V).

To confirm that the thermionic emission is the operating conduction mechanism, the experimental values of η and Φ_B at each temperature were determined using eqs. (4) and (5), respectively. η is estimated from the slope of the linear region of the forward bias plot shown in Fig. 16. The obtained η values (2.8-5.45) indicate that the NPANI/PSi SBD represents a non-ideal diode. Moreover, the obtained values ($\eta > 1$) can be generally attributed to the presence of a bias- dependent Schottky barrier height “SBH”.

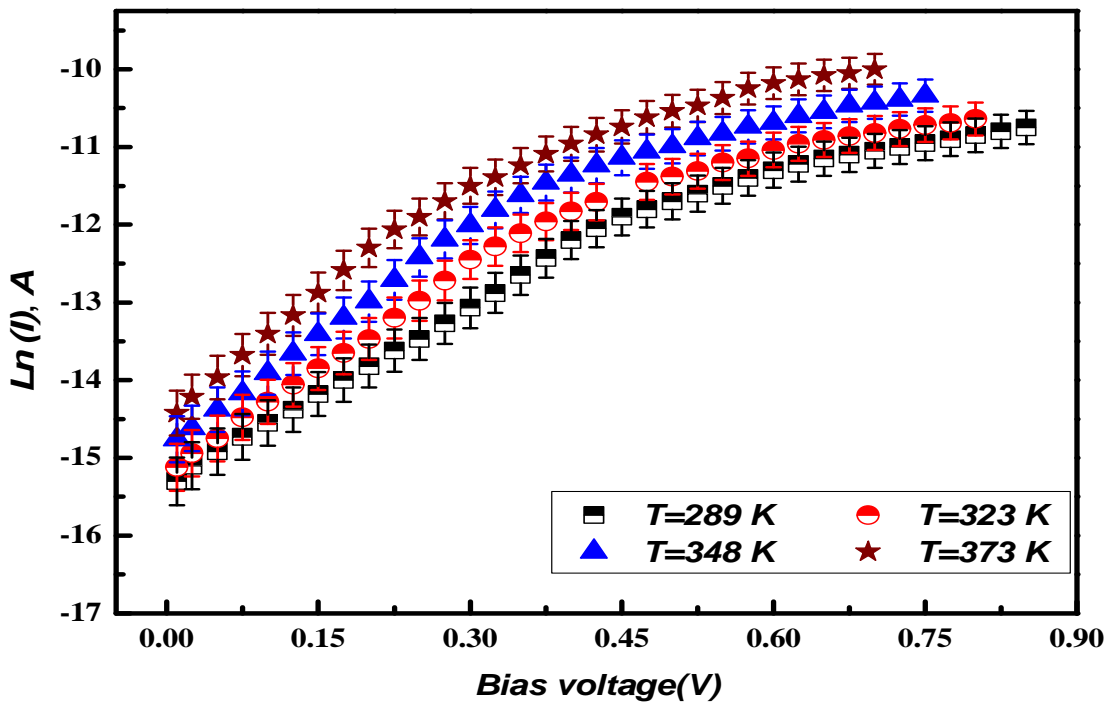


Figure 16. : $\ln(I)$ vis Bias voltage(V) for NPANI/PSi heterojunction at various temperatures in dark. To confirm that the thermionic emission is the operating conduction mechanism, the experimental values of η and Φ_B at each temperature were determined using eqs. (4) and (5), respectively. η is estimated from the slope of the linear region of the forward bias plot shown in Fig. 12. The obtained η values (2.8-5.45) indicate that the NPANI/PSi SBD represents a non-ideal diode.

For an inhomogeneous SBD, with a distribution of low SBH, η may increase with decreasing temperature [121]. The SB consists of laterally inhomogeneous patches of different barrier heights. Since current transport across the organic/inorganic interface is a temperature activated process, at low temperature electrons are able to surmount the lower barriers and, therefore, the current transport will be dominated by the current flowing through the patches of lower SBH and larger η [119-123].

The high values of η are also probably due to a potential drop in the interface layer, and presence of excess current as well as the recombination current through the interfacial states between the PSi substrate and the NPANI organic layer [121,122]. In this case, Φ_B is the contact potential barrier that exists at the interface between organic material and semiconductor layer.

Using linear curve fitting of Fig. 17, Φ_B was found to increase with increasing temperature as shown in Fig.17, while η is decreasing with increasing temperature, in agreement with previous reports [114,119]. It is important to note that such temperature dependence is an obvious disagreement with the reported negative temperature coefficient of SBHs.

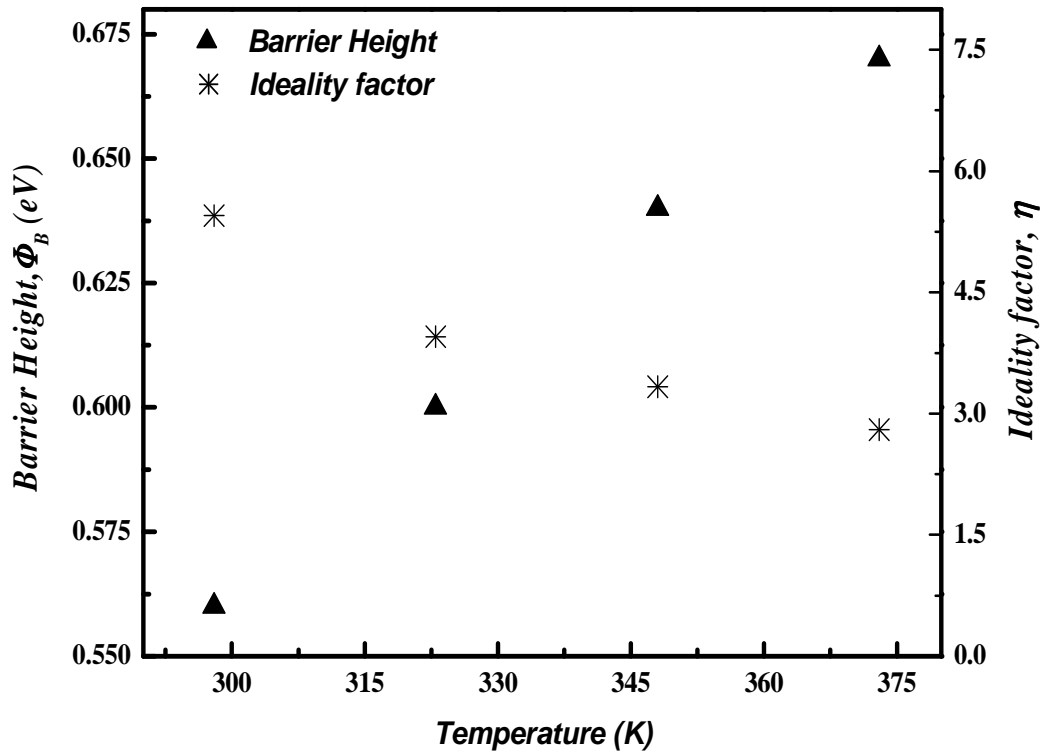


Figure17. Temperature dependence of Barrier height and Ideality factor.

Upon increasing the temperature, more and more electrons will have sufficient energy to surmount the higher barrier. As a result, the dominant Φ_B will increase with increasing temperature and bias voltage [124]. Therefore, the current flow through the lower Φ_B and larger η will dominate the current transport mechanism.

Figure 18 shows the variation of Φ_B versus η for the tested PANI/PSi heterojunction. Note that a linear relationship between Φ_B and η is obtained. This can be evidence that the current transport across the organic/inorganic interface is a temperature-dependent activated process, which can be explained by lateral inhomogeneities of the barrier heights in the diodes [122].

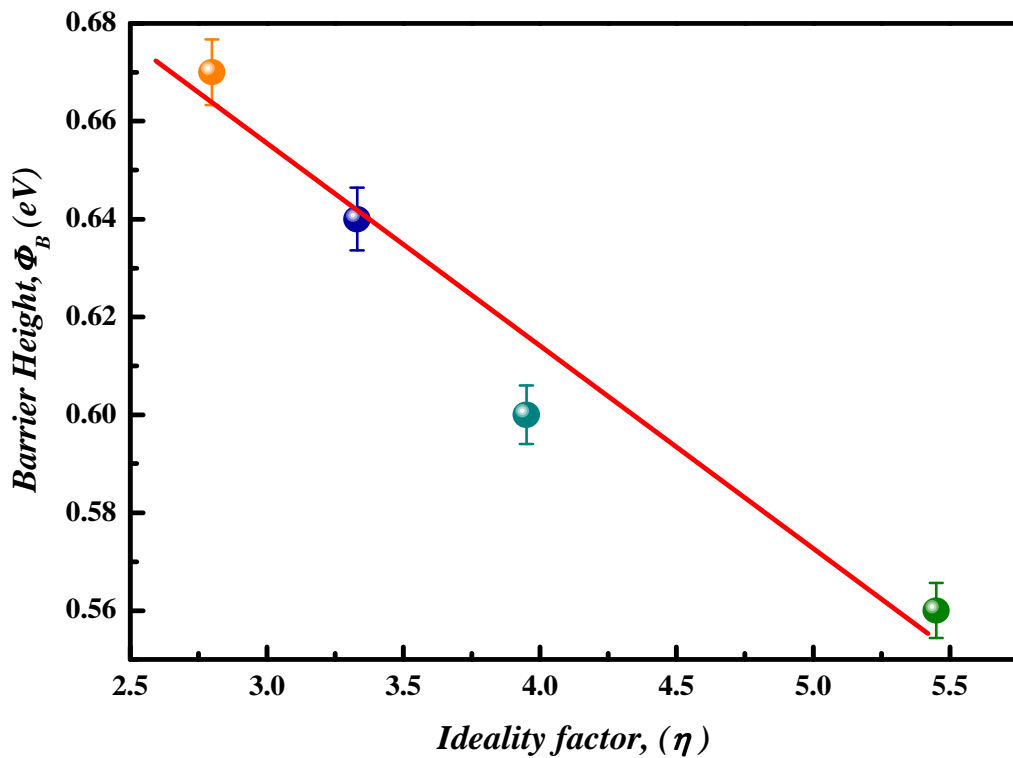


Figure 18. Barrier height versus ideality factor for the NPANI/PSi heterojunction.

The variation of Φ_B versus η for the tested PANI/PSi heterojunction.

A linear relationship between Φ_B and η is obtained. This can be evidence that the current transport across the organic/inorganic interface is a temperature-dependent activated process.

For the evaluation of Φ_B , one may also make use of the Richardson plot of saturation current. Figure 19 shows the variation of $\ln(I_0/T^2)$ versus $1000/T$ where linear relation was observed over the entire range of temperature. This indicates that thermionic emission is the dominant mechanism of charge transport. A Richardson constant (A^*) value of $2.8297 \times 10^{-4} \text{ AK}^{-2}\text{cm}^{-2}$ is determined from intercept at the ordinate of this experimental plot, which is much lower than the corresponding reported value ($32 \text{ AK}^{-2}\text{cm}^{-2}$) for PSi. This deviation

may be due to the spatial inhomogeneous barrier heights and potential fluctuations at the interface that consist of low and high barrier areas [125,126].

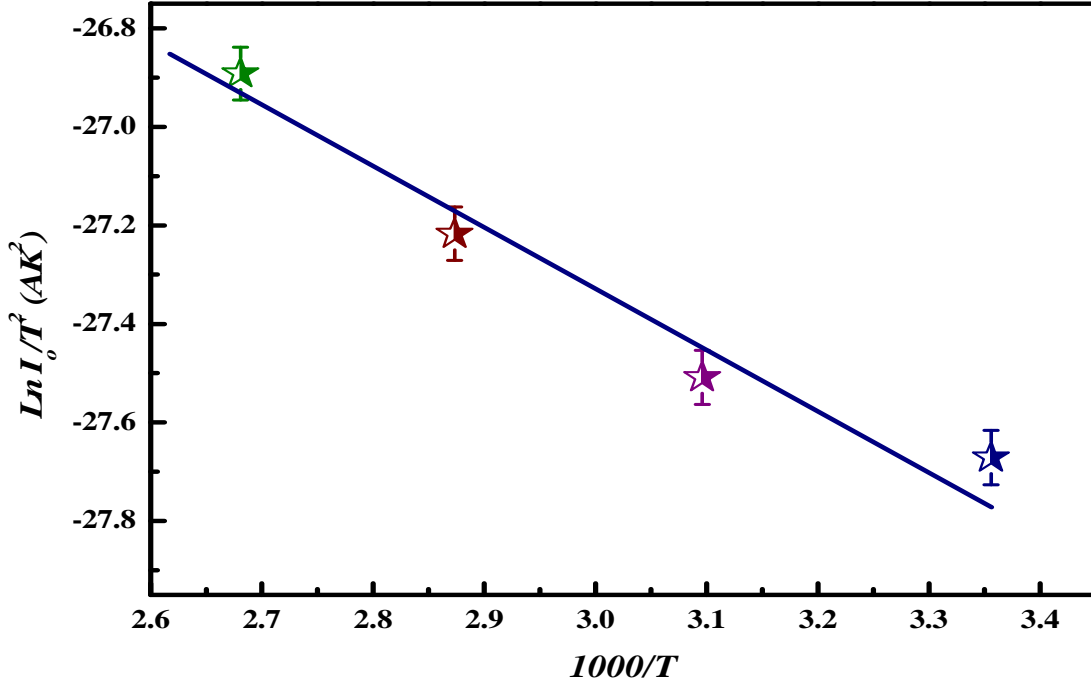


Figure 19. Richardson plot for the NPANI/PSi heterojunction.

The variation of $\ln(I_0/T^2)$ versus $1000/T$ where linear relation was observed over the entire range of temperature. This indicates that thermionic emission is the dominant mechanism of charge transport.

According to the thermionic emission theory, the forward bias I–V characteristics of a Schottky diode with a series resistance can be approximately expressed as:

$$I = I_o \exp\left[\frac{q(V - IR_s)}{\eta kT}\right] \quad (5)$$

where the IR_s is the voltage drop across the series resistance (R_s) of the device. The series resistance can be determined using Eq. (7):

$$\frac{dV}{d(\ln I)} = \frac{\eta kT}{q} + IR_s \quad (6)$$

The values of I_0 , Φ_B , η and R_s for NPANI/PSi heterojunction were calculated from the forward I–V characteristics at different temperatures and listed in Table 1. A plot of $(dV/d\ln I)$ vs. (I) is linear with the slope giving the R_s , and η can be estimated from the intercept ($\eta kT/q$). Temperature dependence of the obtained R_s is shown in Fig. 20. The R_s values vary exponentially with temperature in the temperature range 298–398K. The decrease in R_s with increasing temperature can be attributed to the factors responsible for increasing η and/or to the lack of free carriers at low temperatures [127].

Table 1. Saturation current (I_0), barrier height (Φ_B), ideality factor (η) and R_s factor for NPANI/PSi heterojunction. The values of saturation current (I_0), barrier height (Φ_B), ideality factor (η) and R_s factor for NPANI/PSi heterojunction were calculated from the forward I–V characteristics at different temperatures.

T(K)	I_0 (A)	η	Φ_B (eV)	dV/d(ln I)	
				η	R_s (k Ω)
298	8.52782×10^{-8}	5.45	0.56	4.47	28.8
323	1.17942×10^{-7}	3.95	0.60	3.34	16.8
348	1.83184×10^{-7}	3.33	0.64	2.78	10.2
373	2.91448×10^{-7}	2.80	0.67	2.24	5.81

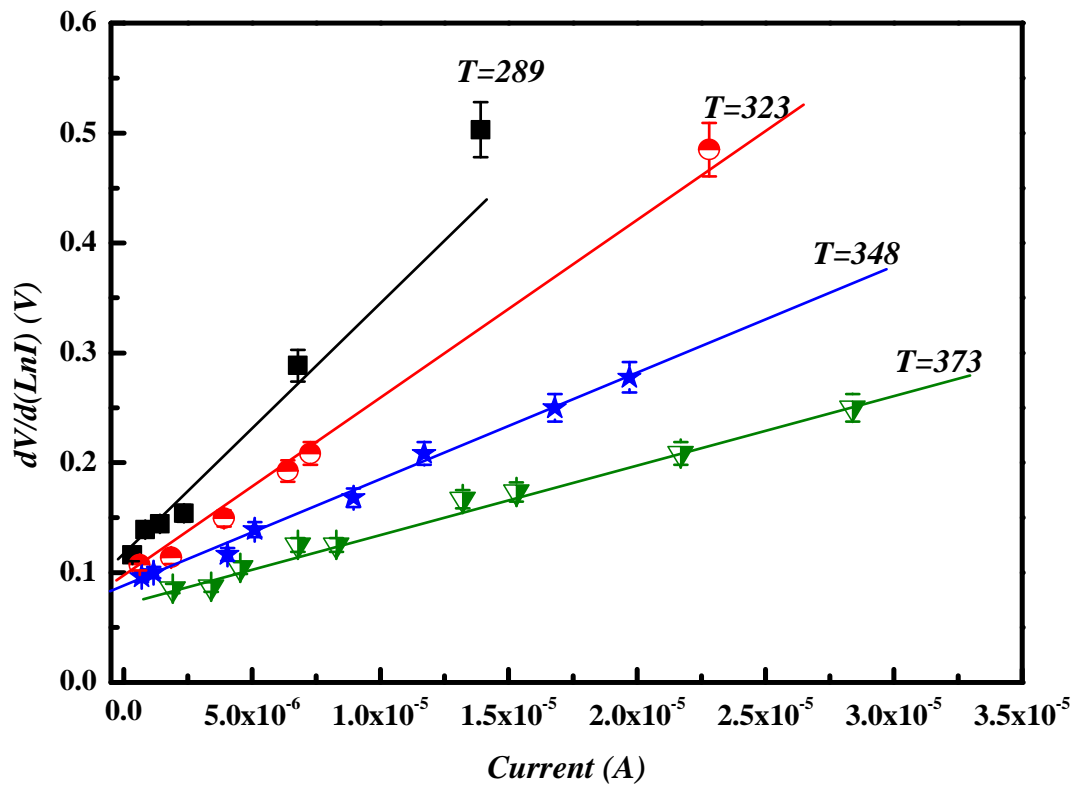


Figure 20. $dV/d(\ln I)$ - I curves of the NPANI/PSi heterojunction at different temperatures. A plot of $(dV/d\ln I)$ vs. (I) is linear with the slope giving the R_s , and η can be estimated from the intercept $(\eta kT/q)$. Temperature dependence of the obtained R_s is shown.

CONCLUSION

The morphological, structural and optical properties of the fabricated nano-polyaniline (NPANI) were characterized by SEM, TEM, FTIR and UV-visible techniques. Different parameters for the assembled NPANI/PSi heterojunction were calculated from I–V measurements performed in the dark conditions in the temperature range 298–373 K. It has been found that while the zero-bias barrier height decreases, ideality factor increases with decreasing temperature. This behavior has been attributed to particular distribution of barrier heights, barrier inhomogeneity, and interface states localized at the NPANI/PSi SBD. The calculated ideality factor (2.8-5.45) indicates that NPANI/PSi SBD represents a non-ideal diode. The series resistance values are decreased with increasing temperature, which was attributed to the factors responsible for increase in η and/or to the lack of free carriers at low temperatures. The results suggested that the NPANI was covalently grafted onto the PSi surface, and polymerization took place throughout the porous layer.

CHAPTER 3

Synthesis and Characterization of NPOT/Si NWs Heterojunction

ABSTRACT..... Herein, the organic nanostructured conducting polymer Poly (ortho-toluidine) / Silicon nanowires (NPOT/SiNWs) heterojunction is investigated as a candidate heterojunction diode with low turn on voltage and lower series resistance compared conducting polymers/porous Si heterojunctions. For this purpose, NPOT/SiNWs heterojunction was fabricated through low cost and simple techniques. The morphology of SiNWs before and after deposition of NPOT was confirmed by scanning electron microscope (SEM). The chemical composition of NPOT was examined by Fourier transform infrared (FTIR) and ultraviolet-visible (UV-visible) spectroscopy techniques. NPOT morphology was identified using SEM and X-ray diffraction techniques. NPOT thin film was chemically fabricated via in situ polymerization method. I-V measurements of the device were made at room temperature under dark conditions. The heterojunction diode parameters such as turn on voltage, reverse saturation current (I_0), ideality factor (η), barrier height (Φ_B) and series resistance (R_s) are determined from I-V curves using Schottky equations. Heterojunction parameters were also extracted and verified by applying different methods of calculations.

3.1 Introduction

Conductive polymer nanostructures have attracted a great deal of interest for use in energy applications because of several beneficial characteristics including tunable electrical properties, flexibility, and high processability from solution [128,129].

On the other hand, polymers as a member of soft matter family have incredible flexibility for the preparation of various nanostructures, particularly for nano-devices. Recently, the interests in nano-structured PANI, especially, PANI nanofibers, have increased extensively [54,55].

3.1.1 POT as PANI Derivative

Poly (O- toluidine) (POT) is a PANI derivative which contains the – CH₃ group in the ortho position of the aniline monomer . Among the ring – substituted PANI derivatives [59].

POT has been probably the most widely studied one. Indeed, Ram and Borol as well as other authors have studied the electro polymerization of (O- toluidine) using various electrolytes with different concentrations, These works revealed that POTs have interesting electro-optical properties and can be used as electrochromic and electronic devices. [130-132]

3.1.2 Si Micropillar /Nanowire Composite Structure

Si micropillar /nanowire composite structures become more interesting recently due to its excellent light trapping and efficient carrier collection, which is applied to design and construct high performance radial p-n junction solar cells. A template-free fabrication method for Si nanostructures, such as Si micropillar /nanowire composite structure is presented. Utilizing an improved metal-assisted electroless chemical etching of Si in KMnO₄/AgNO₃/HF solution. As a result Si composite nanostructure of the long micropillars erected in the short nanowires arrays could be generated on Si substrate. [133]

3.2 Experimental Work

Chemicals:

HF (50% concentration), Silver nitrate (AgNO_3), Potassium permanganate (KMnO_4), ethanol and methanol were used as received. The monomers o-toluidine (OT) was obtained from Aldrich and was purified by doubly distilled before being used for the synthesis and kept at 5 °C before use. Ammonium peroxydisulfate (APS) (Merck) as an oxidant, Sodium dodecyl sulfate (SDS) were used without further purification. All other chemicals were analytical-grade reagents and were used as procured.

Experimental procedures

In these experiments, p-type Si (100) wafers with a resistivity around 1 $\Omega\cdot\text{cm}$ were used. The wafer was cut into 1.0×1.0 cm^2 pieces and used as test samples. Si samples were ultrasonically cleaned in acetone, absolute alcohol, and deionized water successively. Then, the cleaned Si samples were dipped into dilute HF solution to remove native oxide. Following the cleaning step, the etching process was performed through immersing Si samples into the etchant solution, which contains 5 M HF, 0.02 M AgNO_3 , and 0.05 M KMnO_4 . The reaction time was adjusted to be 15 min.

Different etching times were tried and it will be clearly shown when studying the morphologies of the silicon nanostructures by SEM. After etching process, Si samples were rinsed with deionized water and then immersed into the concentrated HNO_3 to remove the retaining silver and other residue. All treatments were performed at room temperature which was 20 °C.

POT was chemically synthesized with APS as an oxidant. A 0.05 M of purified OT was dissolved in 50 ml of 0.03 M SDS solution. A 50 ml of 0.1 M HCl aqueous solution contain 0.05 M of APS was added into the previous OT solution, and at the same time, the mixture was stirred. 5 ml of this mixture was added to the silicon surface; the reaction was lasted for 1 hour at ambient temperature.

The molar ratio of APS as oxidant to OT is 1:1. During the polymerization of OT, the originally colourless mixture turns blue and later becomes dark green. The dark green colour indicated the formation of salt form. Si wafer washed with 0.1 M HCl solution, then dried at 60 °C for 24 h in vacuum-desiccator. The precipitate was collected and washed with methanol to remove the unreacted monomer and the impurities followed by 0.1 M HCl aqueous solution. Precipitate was dried at 60°C for 24 h in vacuum-desiccator.

3.3 Results and discussion

3.3.1 Mechanism for the Formation of SiNWs Array

The formation mechanism of the fabricated SiNWs mentioned in chapter 1 which showed that the main mechanism which is responsible of nanowires fabrication. The initial reduction of Ag^+ which forms Ag nanoparticles on the Si wafer surface which finally led to vertical alignment contributed to the longitudinal falling down of the Ag particles from the surface to the bulk of Si substrates, along with continuous dissolution of Si in the vicinity of Ag particles.

Figure 21 shows a planar top view SEM (image of a tilt angle of 45 degrees) which shows micrograph of the prepared SiNWs array. Figure 1 display the morphology of SiNWs which indicates a uniform SiNWs surface with diameters in the range of 50-200 nm. SiNWs

lengths are in the range of 500-700 nm. Figure 1 also confirms that SiNWs arrays are uniform on the entire wafer surface and they are vertical to the wafer surface.

The large-scale top view image in Fig. 22 confirms that the SiNWs arrays are uniform on the entire wafer surface. SiNWs arrays in which all SiNWs are distinguishable and most of them are vertical to the wafer surface.

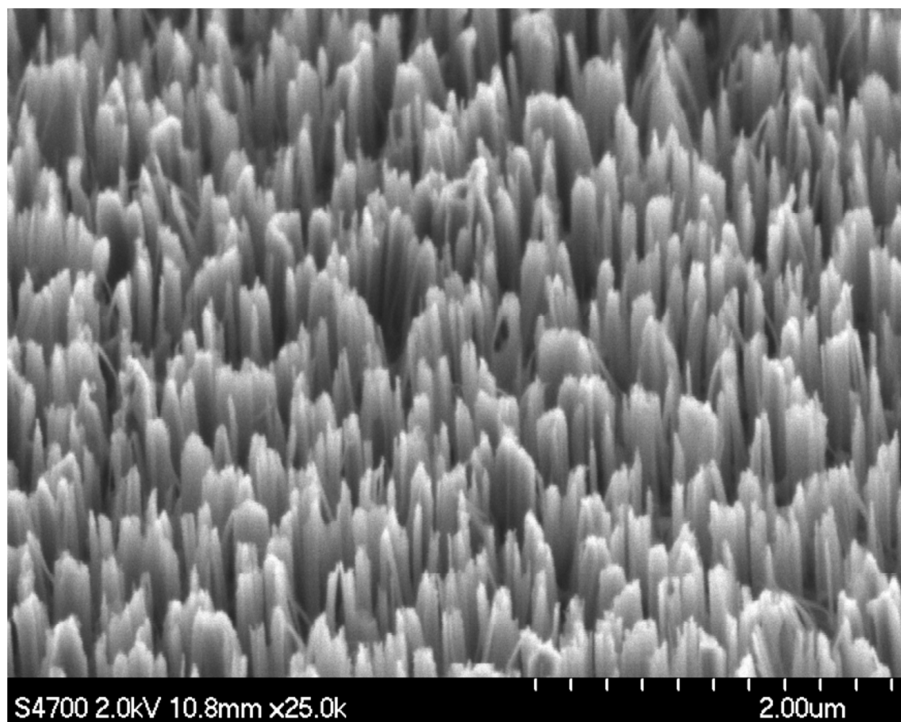


Figure 21. Top view (a tilt angle of 45 degrees) of SiNW arrays after 15 min of etching in 5 M HF, 0.02 M AgNO₃, and 0.05 M KMnO₄ aqueous solution.

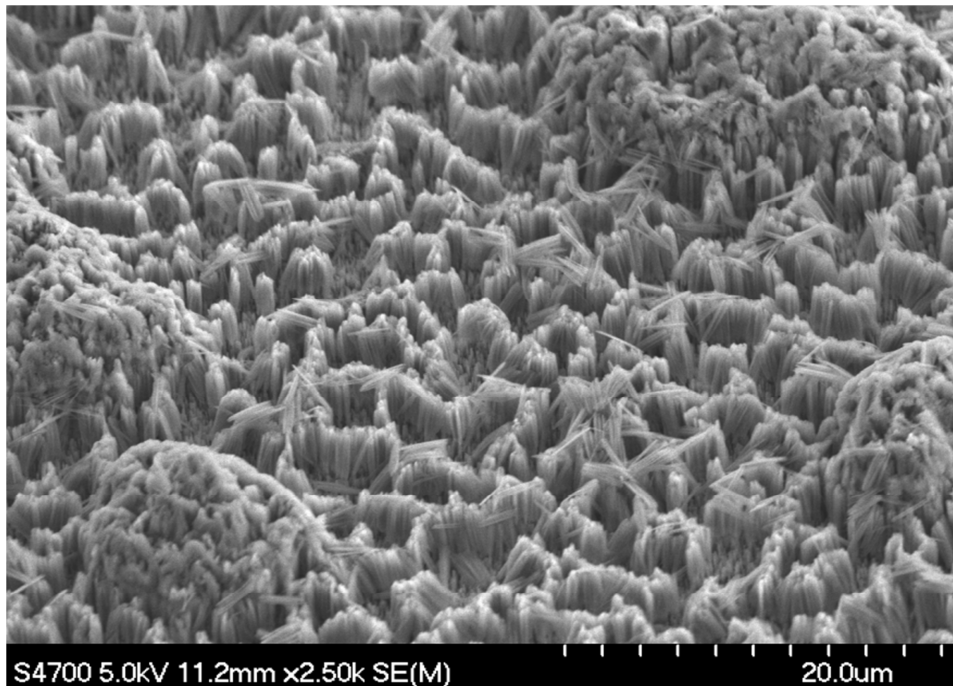


Figure 22. Top view (a tilt angle of 45 degrees) of SiNW arrays formed using in 5 M HF, 0.02 M AgNO₃, and 0.05 M KMnO₄ aqueous solution. The figure shows a large-scale top view image of SiNWs and also Micropillars appear in different places.

As shown SEM images, Some disorder SiNWs arise from cutting and loading of the SEM samples. Also as shown in Fig. 22, it is noticed that a formation of Micropillars occurs during the SiNWs production.

The formation of such micropillars as shown in Fig. 22 was explained and found to be related to K₂SiF₆ crystallite, spontaneously generation. Such generation starts when the solubility product of K₂SiF₆ exceeded to $6.3 \times 10^{-7} \text{ mol}^3\text{dm}^{-9}$, is a byproduct during the forming process of PSi . Hadjersi et al. reported that an insoluble solid-phase film (K₂SiF₆) covered the top of porous silicon layer by the etching of silicon-coated silver film in HF-oxidizing solution.

Also, the existence of K₂SiF₆ layer causes the decrease of the etching rate of Si. So in this fabrication method K₂SiF₆ has an ability to form a masking layer during etching process

and was utilized to realize one-step fabrication of silicon nanowires/ micro-pillar structures. This composite structure is important and becomes more interesting recently due to its excellent light trapping and efficient carrier collection, which is applied to design and construct high performance radial p-n junction solar cells. [133-135]

We can also mention that as the etching time increased the fabricated SiNWs become longer. This is clearly shown in Fig. 23 and Fig. 24. The following two figures show SEM micrographs when the etching time was increased to 30 min and 40 min. The fabricated SiNWs were much longer than the fabricated SiNWs in 15 min in Fig. 21. In our I-V characterizations of the heterojunction diode we used the samples which were etched for 15 min.

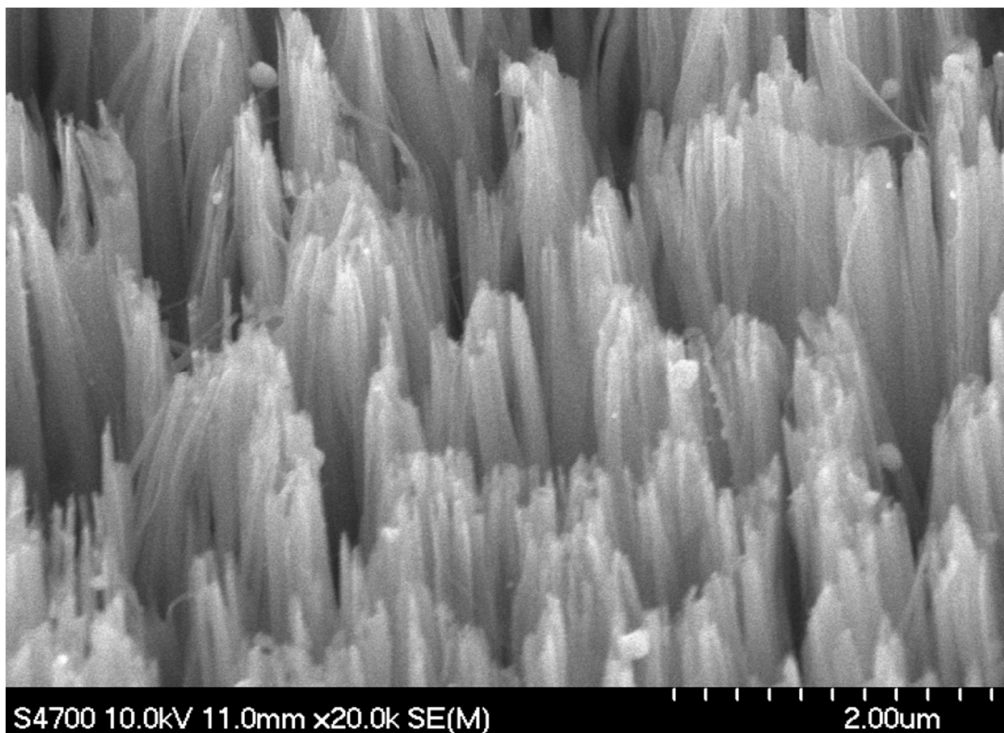


Figure 23. Top views (tilt angle of 45 degrees) of SiNW arrays after 30 min of etching in 5 M HF, 0.02 M AgNO₃, and 0.05 M KMnO₄ aqueous solution.

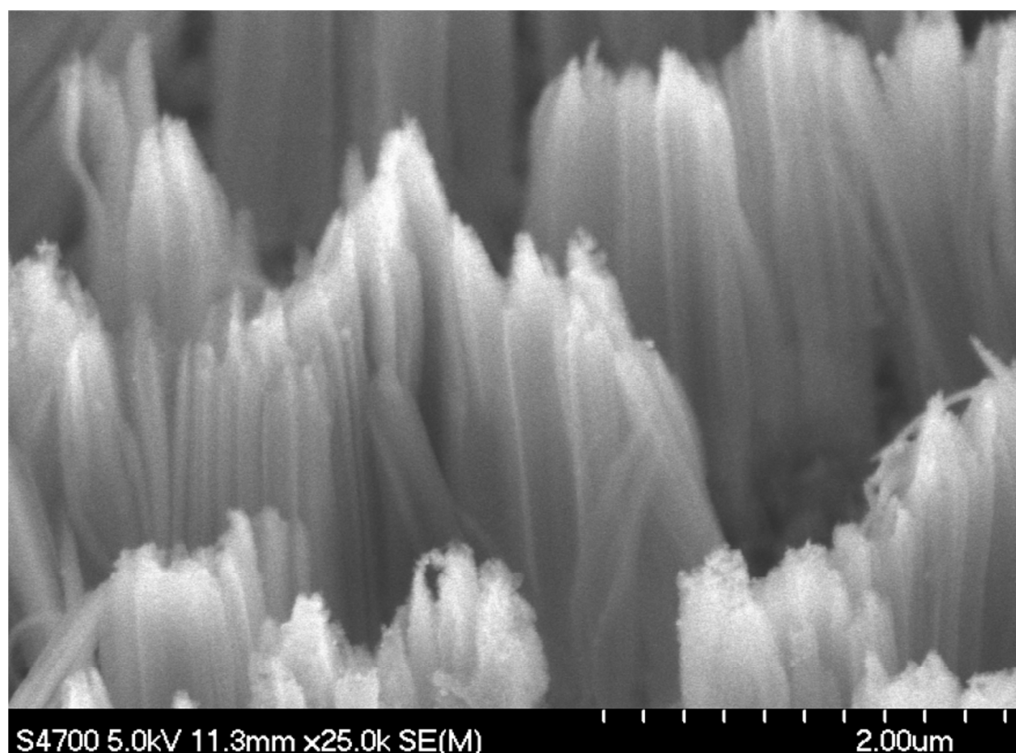


Figure 24. Top views (tilt angle of 45 degrees) of SiNW arrays after 40 min of etching in 5 M HF, 0.02 M AgNO₃, and 0.05 M KMnO₄ aqueous solution.

3.3.2 Characterization of NPOT

FTIR spectroscopy of POT:

UV-vis spectra indicate that POT exists as conductive emeraldine salt Fig. 25(A), there are two peaks near 360 and 698 nm were observed as well as a long absorption band. The 360 nm peak is attributed to the $\pi-\pi^*$ transition of POT's benzenoid ring. The peak at 698 nm and the long absorption band is ascribed to polaron bands, which are characteristic of a conductive emeraldine salt.

FTIR spectra of the polymer materials (in KBr pellets) were recorded on JASCO FTIR 410 spectrophotometer. FT-IR spectra of POT synthesized using $(\text{NH}_4)_2\text{S}_2\text{O}_8$ are illustrated in Fig.25. (B). As seen from Fig.25. (B) represents the IR spectrum for doped PANI.

The main characteristic bands of doped PANI are assigned as follows:

The characteristic sharp band at $1220\text{-}1020\text{ cm}^{-1}$ is due to C-N tertiary aromatic vibration, the bands at 1360 , 1250 , 1340 and 1310 cm^{-1} are due to C-N primary and secondary vibrations. The sharp characteristic band at $3450\text{-}3200\text{ cm}^{-1}$ is due to single bridge compounds polymeric association or to NH stretching vibration. The bands at 1550 and 1475 cm^{-1} are due to the presence of quinoid structure and 1240 cm^{-1} is due to C-N stretching mode for benzenoid ring. The band at 810 cm^{-1} is characteristic of a para-substituted aromatic ring, it appears that polymerization has proceeded in a “head to tail” form. Both UV-vis and FTIR results reveal that the POT nanostructure is typical doped polymer in its emeraldine salt form.

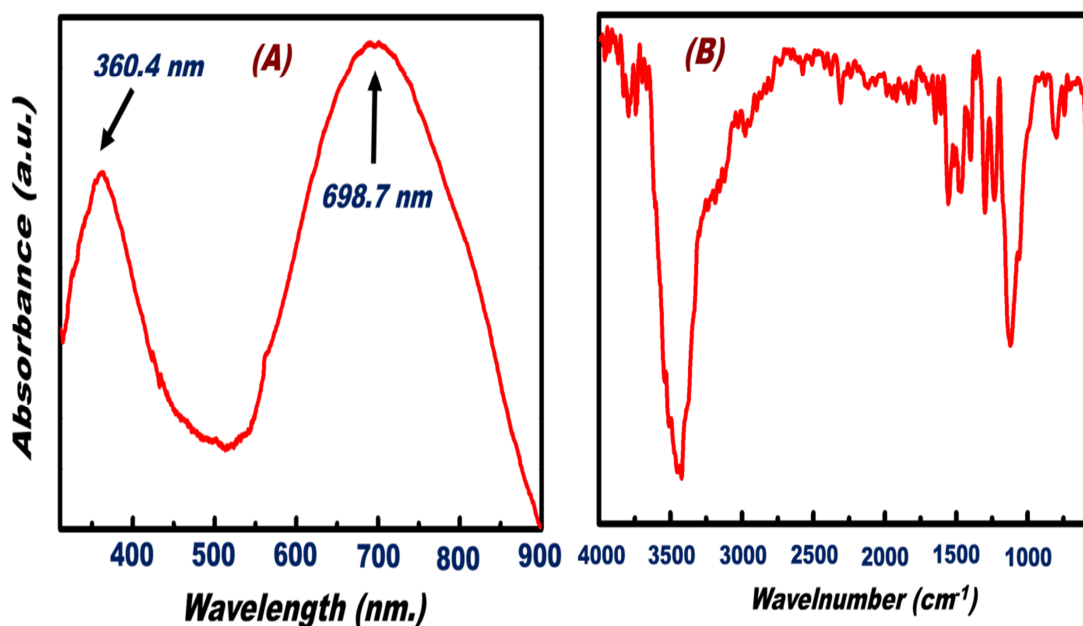


Figure 25. UV-visible spectrum and FTIR spectrum of the synthesized NPANI. The figure shows that the UV-visible spectrum of NPANI film deposited on a glass substrate. It can be shown that the spectrum shows two bands; one at 345 nm corresponds to the π - π^* transition of the benzenoid rings and another broad band at 795 nm corresponds to the quinone structure. (b) FTIR spectrum of the synthesized NPOT, FTIR spectrum of the fabricated NPANI film. The characteristic sharp band appeared in some positions while other bands located at different position. Generally FTIR could give some useful information such proposing that polymerization has proceeded in a “head to tail” form.

X-Ray of NPOT

Figure 26, shows the X-ray diffraction (XRD) patterns of POT, the X-ray profile showed three well defined peaks for the POT prepared. The peaks were observed at $2\theta=15$, 20 and 25°. The maximum peak at around 25° can be assigned to the scattering from the POT chains at the interplanar spacing [136]. On the other hand, two broad peaks centered at $2\theta=15^\circ$ and 20° may be ascribed to the periodicity parallel to the polymer chains, while the latter peaks may be caused by the periodicity perpendicular to the polymer chains [137]. The XRD patterns also result suggest that the nanostructured POT obtained has slightly high crystallinity.

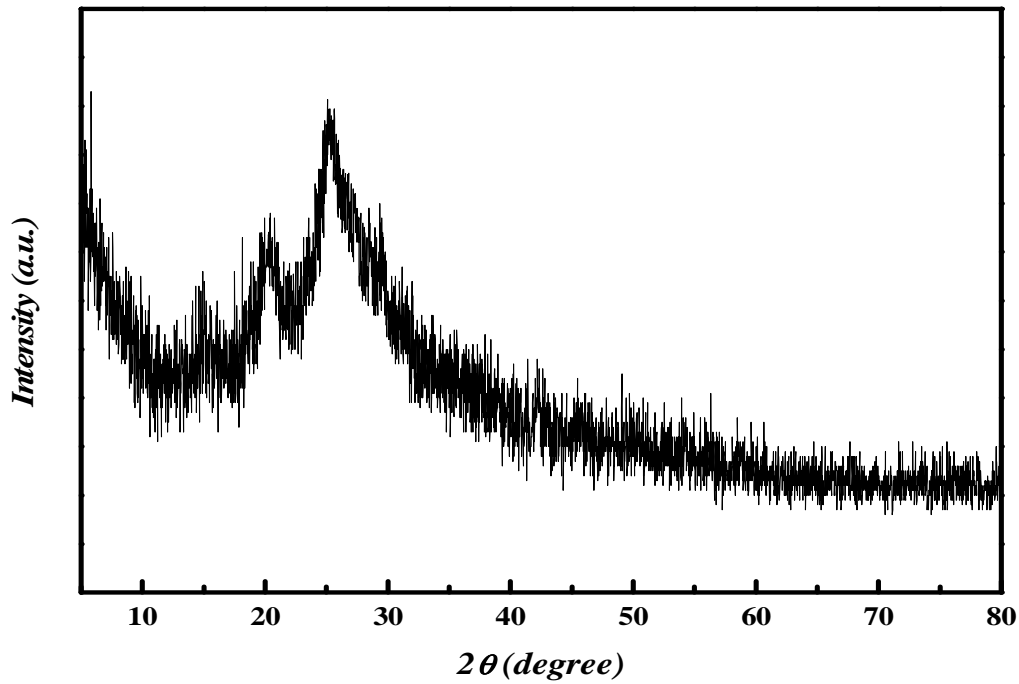


Figure 26 X-ray diffraction (XRD) patterns of POT

SEM was used to investigate surface morphology of the NPOT synthesized. In the SEM micrographs (Fig. 27), rod-like shape nanostructures can be distinguished.

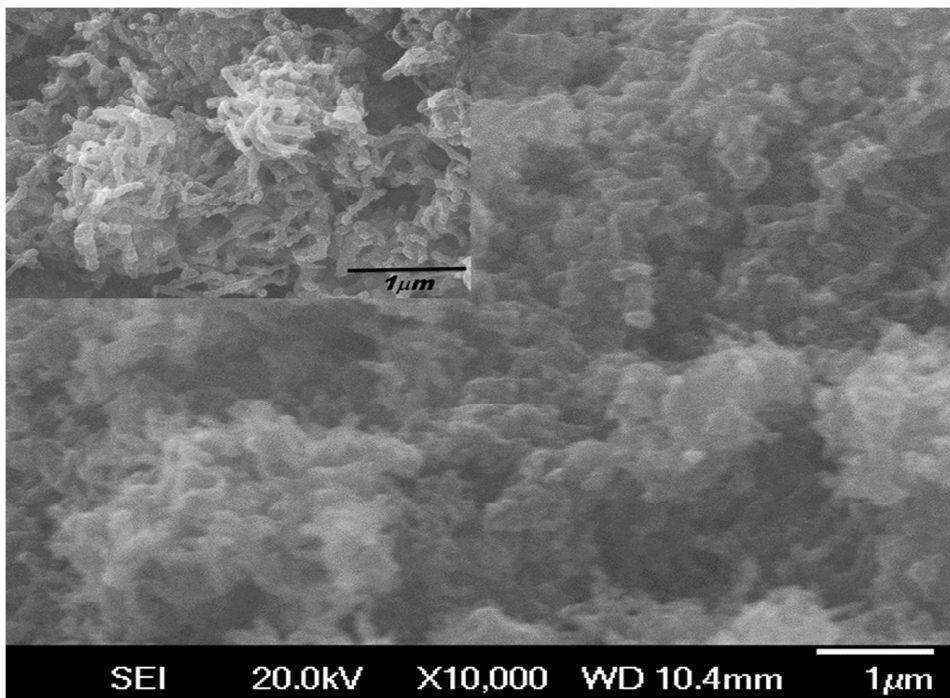


Figure 27. NPOT SEM micrographs and rod-like shape nanostructures.

3.4 Characterization of NPOT/Si NWs Heterojunction

Figure 28 shows the SEM micrograph of after the deposition of the chemically synthesized NPOT upon the fabricated SiNWs. The deposition of NPOT found to be homogenous upon the fabricated SiNWs. Thickness of the NPOT thin film was found to be about 100 nm measured by deposition of the same polymer upon planar Si substrate. We believe that the chemical method which is *in situ* polymerization method is able to make good coverage above and between the fabricated SiNWs. This may give good coverage compared spin coating method. Good coverage is needed to fabricate a valuable and good heterojunction between the conducting polymer and the Si nanostructures.

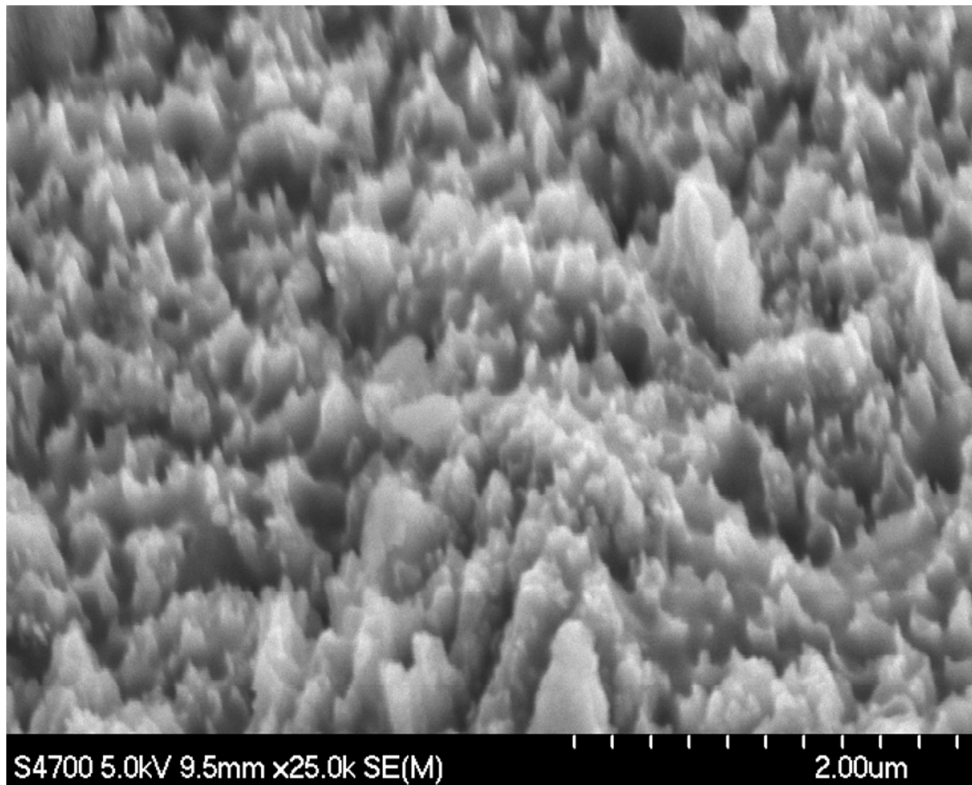


Figure 28 Scanning electron micrograph of SiNWs after the deposition of NPOT.

3.4.1 I-V characteristics of heterojunction

After cleaning and etching, an ohmic contact was made on the bottom of Aluminium (Al) using thermal evaporation. The other ohmic contact was made by thermal evaporation of 100 nm of gold (Au) onto the conducting polymer NPOT.

IV characteristics of the heterostructure was measured for many samples fabricated undergone the same fabrication method and at the same conditions and found to be similar. IV characteristics of heterostructures Al/NPOT/SiNWs/Au could be shown in the following figures.

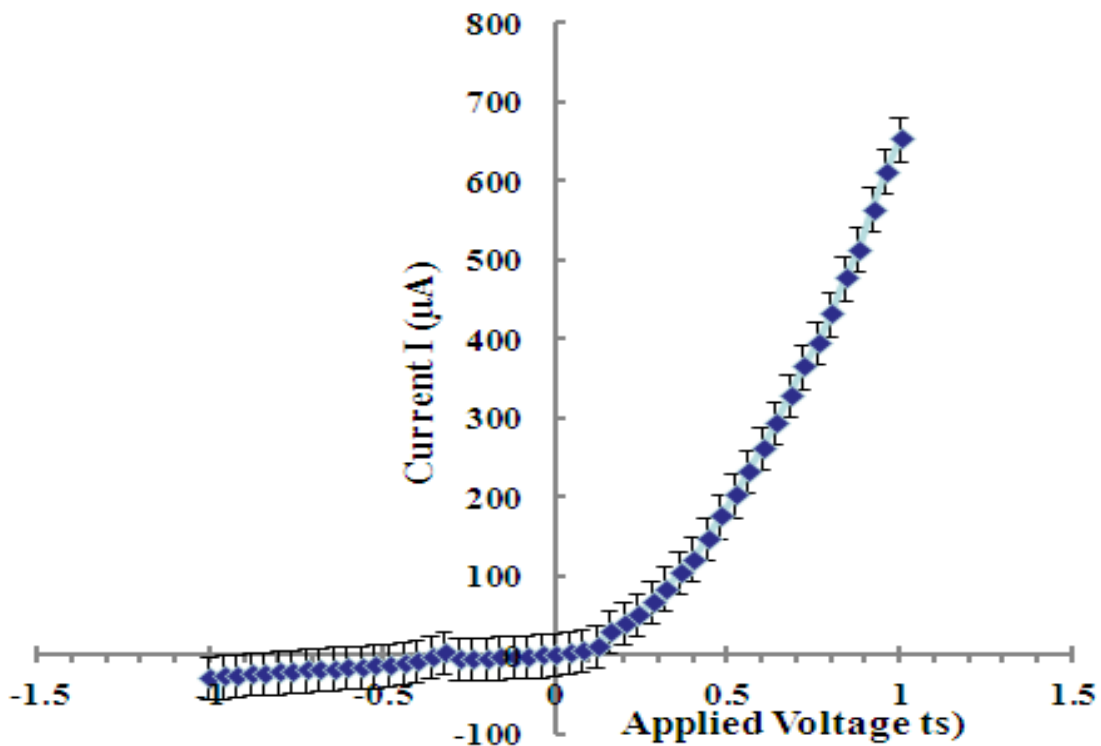


Figure 29 I-V curves for NPANI/PSi heterojunction in dark at room temperature

According to I-V curves shown in Fig. 29 It was noticed that curves clearly possess good diode characteristics which clearly demonstrates the occurrence of a rectifying

junction. The rectification ratio (RR), which is the ratio of forward current to reverse current at same voltage, is 21.4 at ± 1 V.

From the I-V curves it was found that turning voltage is 0.2 volts which much lower than the Si PN diode (0.6 to 0.7 volts) and similar to Schottcky diode (0.2 to 0.3 volts). The low forward voltage drop allows lower power loss than ordinary Si PN junction diodes. So as in Shottcky diode the lower turning on voltage enable the fabricated us to say that the fabricated NPOT/SiNWs heterojunction diode could be used in ultrafast switches in electronic circuits. For this same reason, they may be useful in VHF (Very High Frequency) and UHF (Ultra High Frequency) circuits. They also may be used as switching elements in generators, detectors, motor driver circuits, RF circuits, and a variety of other circuits. [138-140].

With assumption that the current is due to thermionic emission, the current in the device can be analyzed by using thermionic emission theory. So we could apply the same equations from equation (1), equation (2) and equation (3) mentioned in ch 2 when we studied the IV characteristics of Psi/NPANI heterojunction. However most of our calculations here to derive different electronic parameters are the same as in chapter 2 but we prefer to recall these equations again to make the matter easy to be followed.

As previously driven, the current in the device can be analyzed by using thermionic emission theory. According to this theory, the relation between current and voltage of the device can be expressed as [113],

$$I = I_0 \left[\exp \left(- \frac{qV}{\eta kT} \right) - 1 \right] \quad (1)$$

where I_o is the reverse saturation current and is expressed as follows,

$$I_o = AA^* T^2 \exp\left(-\frac{q \Phi_B}{kT}\right) \quad (2)$$

and q is the electron charge, V is the applied voltage, A^* is the effective Richardson constant equal to $32 \text{ A/cm}^2 \text{ K}^2$ for P type Si [119,122], A is the effective diode area, T is the absolute temperature, k is the Boltzmann constant, η is the ideality factor and Φ_B is the barrier height. The value of η could be determined from the slope of the linear region of the forward bias semi log I-V characteristics through the relation [119,141]

$$\eta = \frac{q}{kT} \left(\frac{dV}{d(\ln I)} \right) \quad (3)$$

The barrier height can be obtained from the following equation [143],

$$\Phi_B = \frac{kT}{q} \ln\left(\frac{AA^* T^2}{I_o}\right) \quad (4)$$

Since the current curve in forward bias quickly becomes dominated by series resistance and deviates from linearity so low forward bias part of I-V characteristics should be used to calculate the ideality factor. The ideality factor η could be calculated according to the natural logarithm (lnI-V) plot according to the following equation:

$$\ln I = \ln I_o + \frac{q}{\eta kT} V \quad (5)$$

During reading in literature we found that such method is not so accurate and sometimes give unreasonable values of the ideality factor η . The reason may return to that this method only works for diodes with low series resistance which can be neglected in the low forward region of I-V curve. This could not be satisfied in many heterojunctions.

Also in our opinion to perform least square fitting strongly related the effect of series resistance even for low forward bias comparing conventional p-n junction diodes [143].

For the past mentioned reasons, the past method of calculation could not be only the method that we can depend to derive or tell something especially about the ideality factor. Other methods of calculations should be taken in consideration.

According to equation (5) the $(\ln I-V)$ plot could be shown in the following figure:

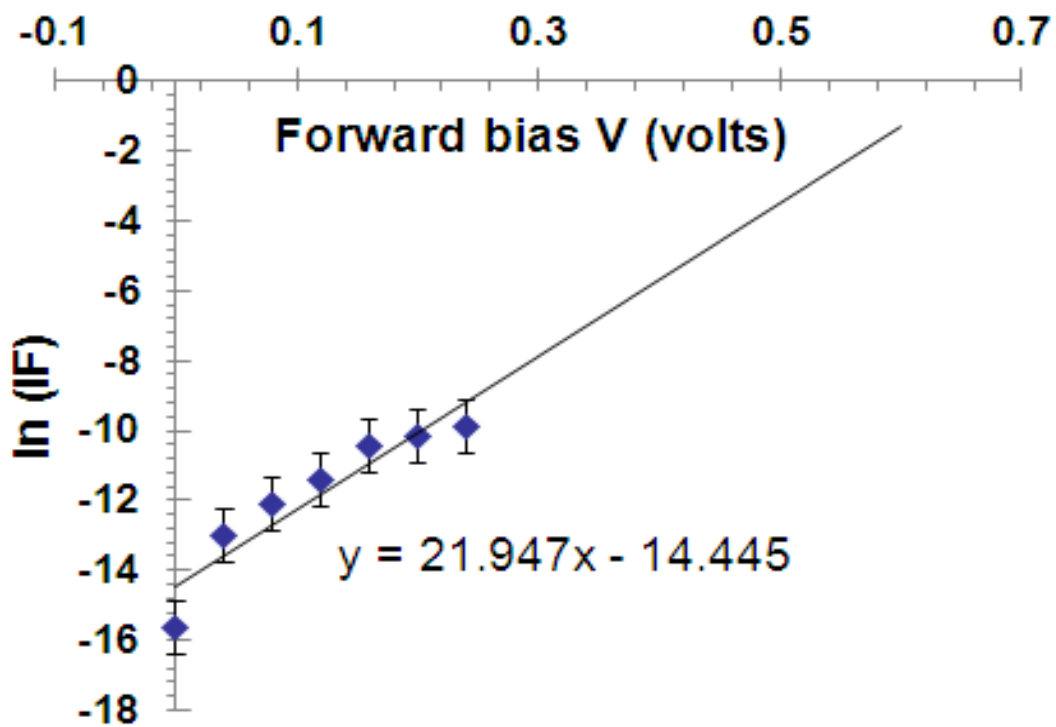


Fig. 30 $\ln I-V$ plot of the PtSi/p-Si Schottky diode at the temperature of 293 K in dark

The ideality factor η and the saturation current I_0 could be calculated from the slope and the y-axis intercept of the fitted straight line respectively. Using equation (5) η and I_0 were determined to be 1.8 and 5.328×10^{-7} A. From equation (4) we are able to calculate the barrier height Φ_B which found to equal 0.74 eV.

Series resistance R_s is an important parameter that influences the electrical characteristics of heterojunction diode so we used Cheung method as a second and efficient method to calculate R_s and confirming the values of Φ_B , and η calculated from the previous method. Cheung method was found to be helpful and convenient to check the validity of the diode-series resistor model because deviations from straight lines can easily be detected [144]. The forward bias current-voltage characteristics due to thermionic emission of a Schottky barrier diode with series resistance can be expressed as Cheung's functions as in the following equations,

$$\frac{dV}{d\ln I} = IR_s + \eta \frac{KT}{q} \quad (6)$$

$$H(I) = V - \eta \frac{KT}{q} \ln\left(\frac{1}{AA^*T^2}\right) \quad (7)$$

$$H(I) = IR_s + \eta \Phi_B \quad (8)$$

Experimental $dV/d\ln I$ vs. I plot of our heterojunction diode at room temperature of 293 K is presented in Fig. 31

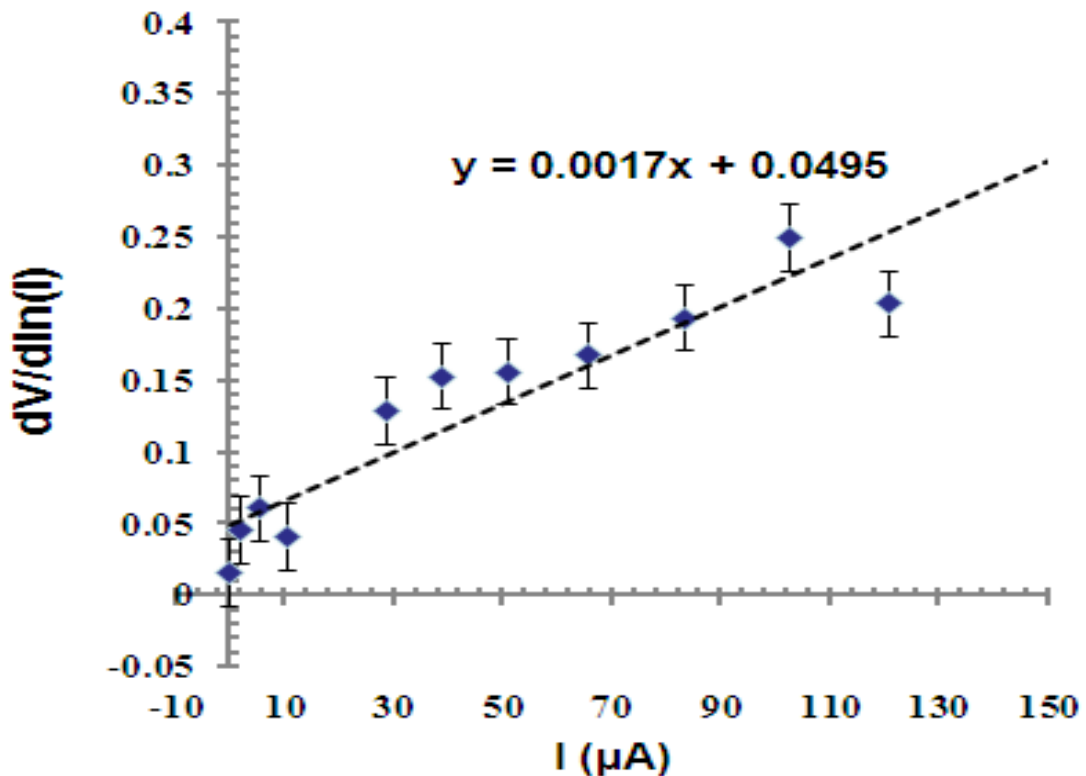


Fig. 31 The $dV/d\ln I$ vs. I plot of NPOT/SiNWs heterojunction diode at the temperature of 293 K

After fitting the curve to a straight line and using equation (7), η and R_s can be determined from the intercept and the slope of the line respectively. R_s and η were determined to be 1.7 K Ω and 1.9565 respectively. The value of η obtained by this method is in great agreement with the values determined by applying the thermionic emission theory to I-V characteristics.

Using the η value determined from Eq. (8), a plot of $H(I)$ vs I as shown in Fig. will also give a straight line with y-axis intercept equal to Φ_B and the slope of this plot also provides a second determination of R_s . In this method we used the least square fitting approach which gives us the opportunity of using more data points and hence increasing the accuracy of our calculations.

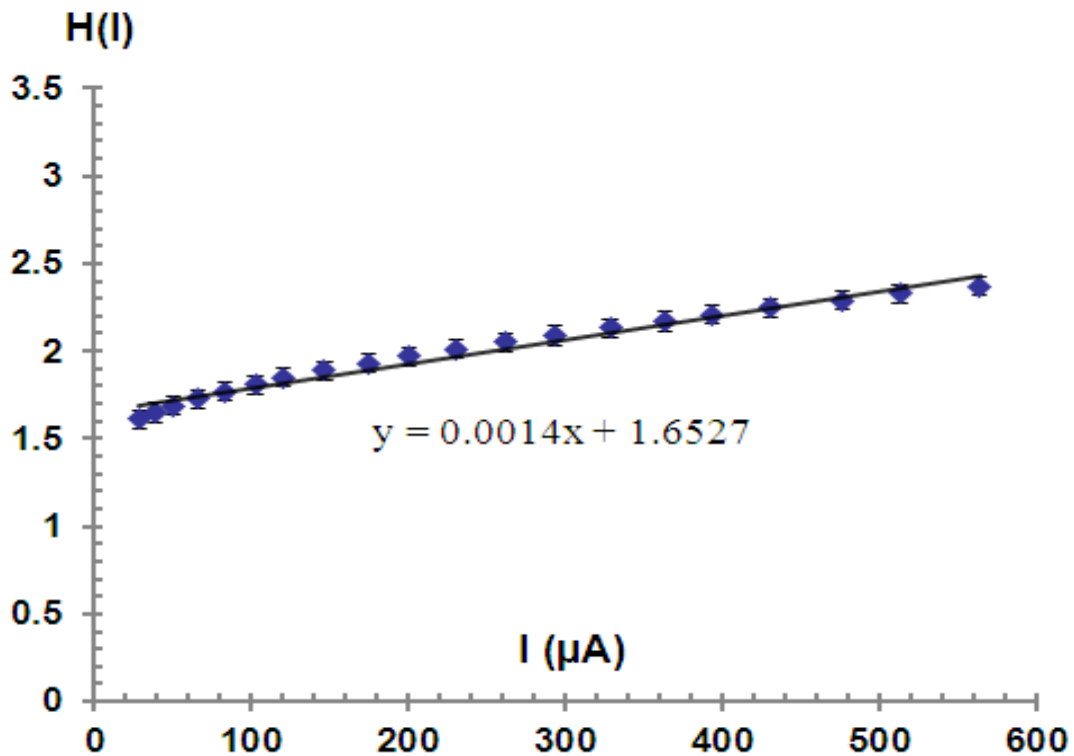


Figure 32. $H(I)$ vs I plot of NPOT/SiNWs heterojunction.

From Fig. 32, the values of Φ_B and R_s were determined to be 0.844 eV and 1.4K Ω respectively. The value of η obtained by this method is in great agreement with the values determined by applying the thermionic emission theory to I-V characteristics.

The values of η (average value calculated was found to be 1.87) and R_s (1.4 K Ω) of this NPOT/SiNWs heterojunction was much lower than η and R_s of NPANI/PSi heterojunction we fabricated and discussed before in chapter 2. which was already published [145].

We opened the scope and compared the value of η and R_s of our NPOT/SiNWs heterojunction compared with values η and R_s of different conducting polymers such like PANI or Polypyrrole/PSi heterojunctions mentioned in many research papers in literature [146-150].

The exact mechanism of this high ideality factor has not been fully understood. However in literature some reported that the higher value suggests that the carrier recombination in Si substrate may be significant in conduction mechanism [148], some suggested Ideal ity factor is high because they used PSi as substrate and therefore at the interface of heterojunction the defect density is very high [147]

We expected that the R_s of the fabricated NPOT/ SiNWs become lower as SiNWs may play an important role to decrease R_s compared with Psi structures. The reason may be understood as the aligned one-dimensional nanowire arrays offer a promising substrate providing a direct pathway for charge transport and high mobility for carriers. In addition it was reported that SiNWs could play an important role in providing a large effective junction area which could help in light trapping helping in solar cell applications [151] which is considered as a future point of research to use NPOT/SiNWs heterojunction as a hybrid solar cell. Also we are presently performing experiments to investigate the conduction mechanisms in more details.

Regardless of these details, the lower η and R_s shown here already demonstrate the potential for the fabrication of high quality NPOT/SiNWs heterojunctions.

CONCLUSIONS

SiNWs fabricated using improved metal-assisted electroless etching of silicon in $\text{KMnO}_4/\text{AgNO}_3/\text{HF}$ solution. A high quality NPOT/SiNWs heterojunction has been fabricated through low cost and simple techniques in all stages of fabrication processes. The devices present reproducibility of electrical characteristics, good rectifying behavior. NPOT/SiNWs provided low turn on voltage (0.2 volts), which may give possibility to use such heterojunction diode like Schottky diode in ultrafast switching. The saturation current of I_0 was found to equal 5.328×10^{-7} A. The ideality factor becomes close to 2. The series resistance R_s was found to be about equal 1.4 $\text{K}\Omega$ which is lower than R_s in case of using PSi heterojunctions. The barrier height was about 0.79 eV. The heterojunction is presently putting in our consideration as a candidate for solar cell applications.

CHAPTER 4

Design and Characterization of Integrated a Plasmonic Nanosensor for lab-on-chip applications

ABSTRACT..... A novel integrated plasmonic resonator was proposed and analyzed. The detection performance of our device has been numerically verified by (FDTD) finite-difference time-domain simulations. The spectral sensitivity obtained found to be 700 nm/RIU, where RIU is the refractive index unit. Our proposed sensor was found to have a detection limit in the order of 10^{-6} RIU. The plasmonic sensor could be fabricated using FIB milling. Our design leads to an ultra-compact sensor suitable for on-chip sensing applications associated with a high sensitivity. For biosensing, the proposed sensor could have the ability for a specific capture of biomolecules at the sensor surface that enables for quantification of the biomolecules.

4.1 Introduction

Refractive index sensing has a wide range of applications in areas such as chemistry, physics and biomedical engineering. Measuring the refractive indices of chemicals and food products are utilized for managing the quality of these products in the field of industry. The density and concentration of mixtures can be measured by detecting a refractive index change of the product such as chemicals [152-155].

One of the most widely used approaches involves detecting the spectral shift of a resonant feature as the refractive index is varied. Different techniques have been introduced for the implementation of compact and portable sensors [156].

Recently, the detection of minor changes in the refractive index has been required for precise sensing. Therefore, the refractive index measurement system with a high accuracy is of prime importance.

In the last decade, novel sensing techniques with high accuracy and good detectivity (detection limit) have been proposed based on plasmonic structures [156,157]. Among these techniques Surface plasmon resonance (SPR) considered as a key candidate for such applications sensor. SPR uses surface plasmon polariton (SPP) waves to probe interactions between biomolecules and sensor surfaces have attracted tremendous interest in the past decade for optical detection of small biological or chemical entities in liquids [156,158].

In general, surface plasmon wave is formed through coherent oscillation of free electrons at a metal-dielectric interface. The electromagnetic energy of a surface plasmon mode is highly confined at the metal dielectric interface. Thus, these modes are highly sensitive to the refractive index changes of the dielectric medium [158].

However, conventional SPR sensor systems are usually large and bulky because of the excitation and interrogation mechanism, which is mostly done through prism coupling and angle interrogation. Thus, those systems and its associated peripherals are not well-suitable for lab-on-chip applications. Recently, plasmonic resonators have been investigated to propose novel integrated structures with small footprint. These plasmonic resonators can easily influenced by the surrounding environment which may result in shift of the resonance wavelength [159-163].

We propose a novel system using the plasmonic resonator for detecting a micro change of the refractive index. The detection performance of our device has been numerically evaluated by (FDTD) finite-difference time-domain simulations. Our design has

been easily fabricated using the focus ion beam milling technique. It leads to a highly compact sensor in terms of high integration in dimensions of few hundred nanometers associated with a high sensitivity and high detection limit.

4.2 FDTD Simulations

In order to verify the performance of the proposed plasmonic sensor, using commercial FDTD simulation has been exploited [164].

In order to test our setup, few test cases have been first examined by verifying the simulations results in [161].

In addition, the perfect matched layer has been optimized in order to minimize the reflection from plasmonic waveguides. Figure 33 shows a schematic of the plasmonic square resonator using Metal-Insulator-Metal (MIM) configuration. The refractive index of the SiO₂ substrate set to 1.45. The permittivity of silver is given by the Drude model as:

$$\varepsilon(\omega) = \varepsilon_{\infty} - \frac{\omega_p^2}{\omega^2 + i\gamma\omega}, \quad (1)$$

Where ε_{∞} is the relative permittivity at infinite frequency, ω_p is the plasma frequency, and γ is the collision frequency; these parameters are set to 6.0, 1.5×10^{16} rad/s, and 7.73×10^{13} rad/s, respectively [165].

The 2D TM simulations have been performed with a mesh size in x and y direction taken to be 3 nm, number of time steps 32,000 steps with time step of 0.007236 f sec. The Perfectly Matched Layer (PML) is utilized with 12 layers in all directions. A converge

analysis has been performed to examine the effect of mesh size on the output. This analysis shows that the results change of 1% is obtained for mesh size of 4 nm.

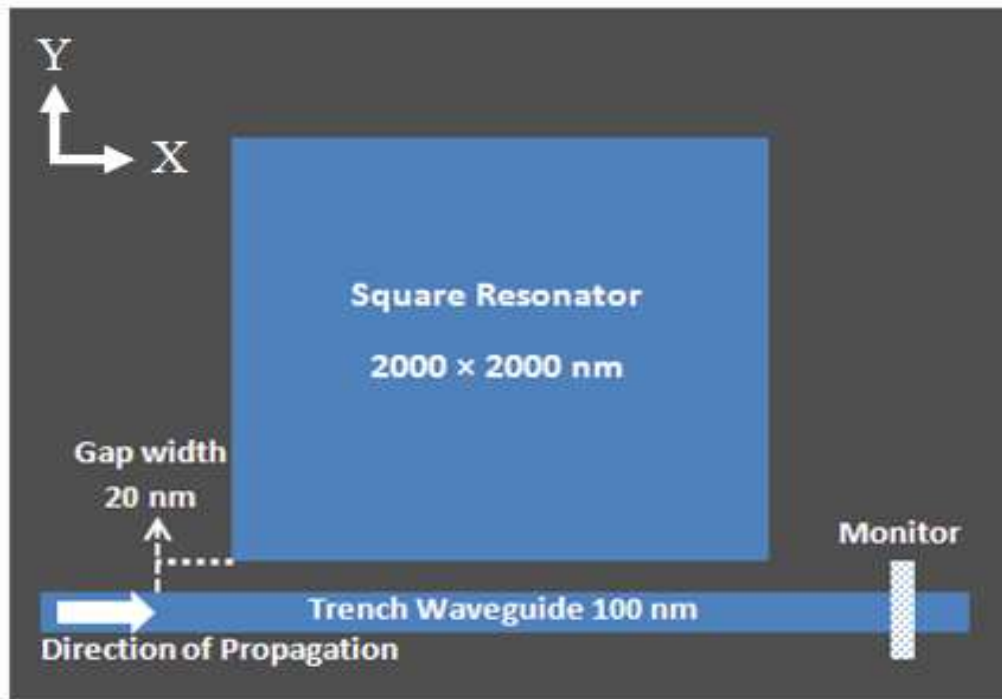


Figure. 33. Schematics of the plasmonic square resonator with a trench structure used in the FDTD simulations. The figure shows a schematic of the plasmonic square resonator using Metal-Insulator-Metal (MIM) configuration. The light is incident at the input port [denoted by Direction of Propagation]. The transmission intensity is detected around 450 nm away from the square resonator's right edge [denoted by Monitor].

4.3 Wavelength characteristics of the plasmonic square resonator

The wavelength characteristics of the plasmonic square resonator are evaluated using FDTD. Figure 34 shows the transmission intensities (output power divided by the input power $|E_{\text{output}}|^2 / |E_{\text{input}}|^2$) of the trench plasmonic waveguide as functions of wavelength. The solid and dotted lines correspond to the transmission intensities when the refractive index near the resonator changed from 1.00 to 1.01, respectively. The light is incident at the input port [denoted by Direction of Propagation in Fig. 33]. The transmission

intensity is detected around 450 nm away from the square resonator's right edge [denoted by Monitor in Fig. 33].

For specific wavelengths resonance occurs and plasmons are coupled to the square resonator. The transmission spectrum will exhibit a very sharp drop for this specific wavelength. The resonance wavelength is very sensitive to changes of the effective index, which on its turn is very sensitive to changes of the refractive index of the surrounding medium [166].

When the refractive index of dielectrical surroundings of square cavity is changed, the resonance condition for the device changes, and as a result, the resonant mode shifts to a new wavelength. So, a change of the refractive index of sensed materials can be detected by the shift of the resonant wavelength. In addition change in refractive index of the region probed by the resonant mode causes a corresponding frequency shift. The change in resonant frequency is converted to the sensing signal [167].

For our proposed sensor, it was found that when the refractive index near the resonator varies from 1.00 to 1.01, the wavelength is shifted by nearly 7 nm. The wavelength shift could be shown clearly in the magnified image in Fig. 34.

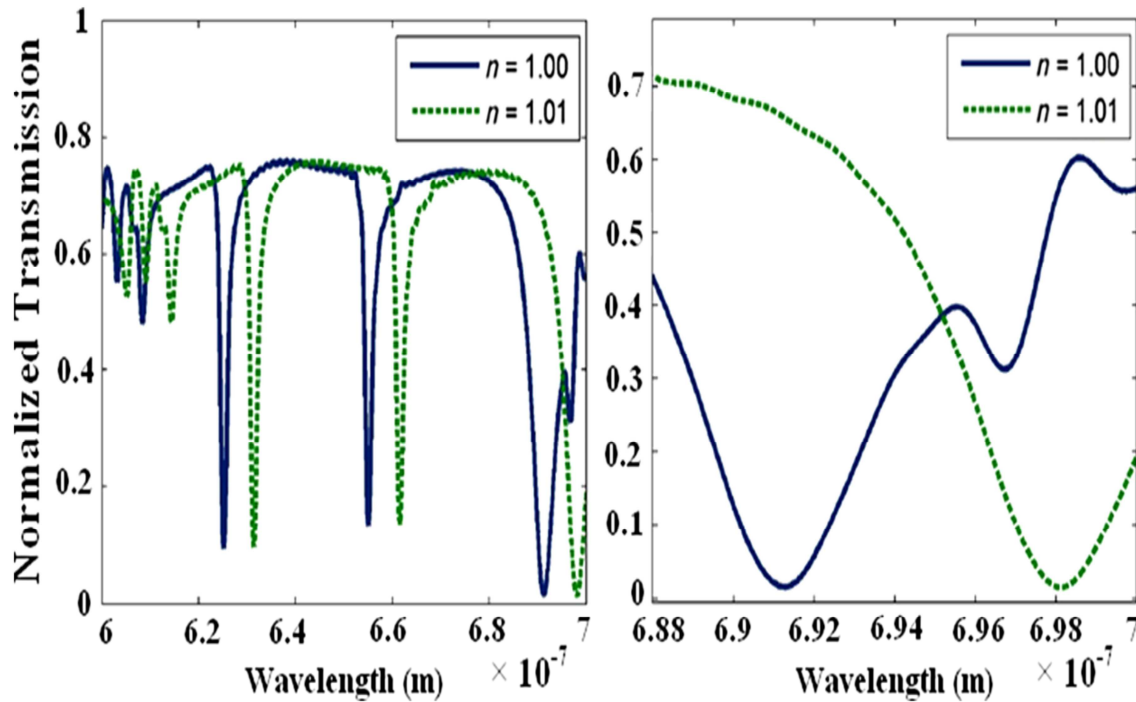


Figure 34. Transmission spectra of plasmonic square resonator as a function of wavelength.

When the refractive index near the resonator varies from 1.00 to 1.01, the wavelength is shifted by nearly 7 nm. The wavelength shift could be shown clearly in the magnified image appears on the right hand side.

For high detection of refractive index changes, it's preferred to use the wavelength with the largest rate of change in the transmission intensity as an experimental reference, so that a small shift in the wavelength corresponds to the largest change in intensity. It was found that at a wavelength equal 691 nm, when the refractive index was changed from 1.00 to 1.01, the transmission intensity had the maximum absolute slope. Such drop in the transmission intensity holds as the key to detect the small refractive index change near the plasmonic resonator. A shift in the resonant wavelength provides information about the refractive index shift. Thus, it is standard to define the spectral sensitivity of such sensors as $S = \Delta\lambda/\Delta n$. The spectral sensitivity has a unit of nm/RIU, where RIU is the refractive index unit [168,169]. In our case the spectral sensitivity was found to be 700 nm/RIU.

The impact of our proposed sensor as compact sensor suitable for on-chip sensing applications could be understood when involved in a proposed design of an integrated hybrid chip as shown in Fig.35. It should be mentioned that other devices such as detectors etc. could be fabricated on such hybrid chip to serve multifunctional measurements. The proposed integrated plasmonic sensor will be associated with input and output ports through an efficient coupling between the trench plasmonic waveguide and a silicon waveguide. The efficient coupling between plasmonic waveguide and silicon waveguide recently has been demonstrated over wide band [169,170].

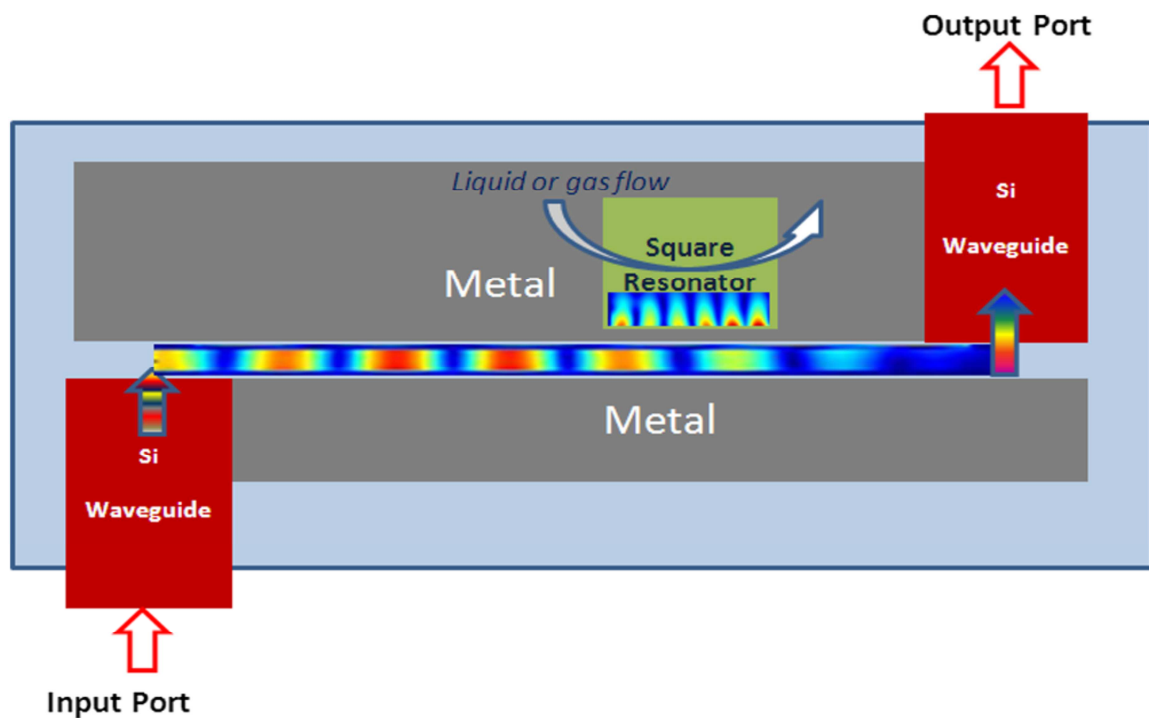


Figure 35. A proposed design of an integrated hybrid chip involving our proposed plasmonic sensor. From such figure we could understand that the proposed nanosensor could be involved in a proposed design of an integrated hybrid chip. The plasmonic sensor could be associated with input and output ports through an efficient coupling between the trench plasmonic waveguide and a silicon waveguide.

As shown in Fig.35, the refractive index of dielectrical surroundings of square cavity could be changed as a result of gas or liquid flow near the square resonator. So our proposed

sensor could be used in gas- and liquid-phase chemical sensing. Also it is well known that the specific capture of biomolecules at the sensor surface results in a local change in refractive index, producing a sensing signal that enables quantification of the biomolecules in a sample [167].

In addition, the sensing mode of operation could use a broadband input. As a function of the refractive index of the sample medium we monitor the position of the spectral minima in the transmission curve. This approach has been called ‘wavelength interrogation mode’ in the literature [46,166].

4.4 Electric field profiles of the plasmonic square resonator

Figure 36 shows the profiles of the electric field in the plasmonic square resonator (a) a wavelength of 691.0 nm and (b) 673.0 nm. As shown in Fig. 36(a) at the resonance wavelength 691.0 nm, SPPs are enhanced in the square resonator. The SPPs are coupled from the waveguide to the square resonator and enhanced. In this case, the transmission intensity is minimum at the output port.

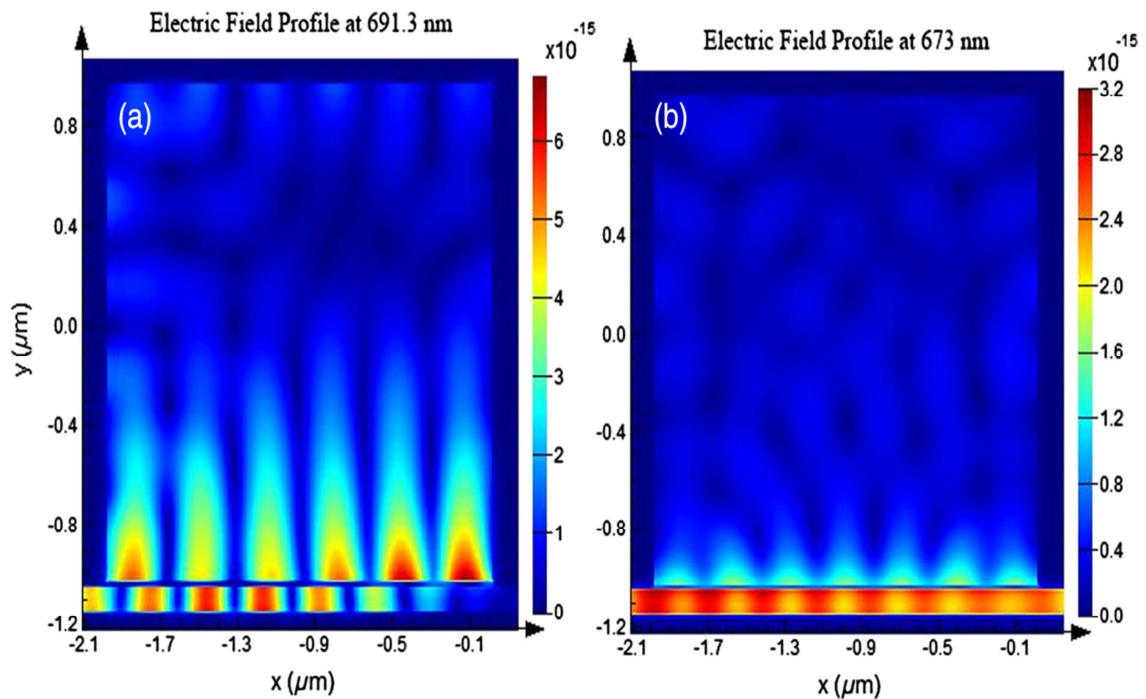


Figure 36. Profiles of the electric field in the plasmonic square resonator for (A) a wavelength of 691.3 nm (This wavelength is a resonance wavelength i.e The SPPs are coupled from the waveguide to the square resonator and enhanced) and for (B) a wavelength 673.0 nm (At this wavelength offresonance occur i.e The SPPs is not coupled in the square resonator)

In Fig. 36(b) a negligible portion of the optical field is coupled from the waveguide to the square resonator. The SPPs is not coupled in the square resonator as the wavelength of 673.0 nm is off resonance wavelength.

Therefore, due to the high field localization inside the square resonator at the resonance case, the interaction between the optical field and any material inside this resonator is maximized. Accordingly, any small change of the refractive index inside the resonator results in a significant shift in the resonance condition.

4.5 Analysis of the detection limit of the refractive index Change

In order to evaluate the detection limit of the refractive index change, the refractive index of materials surrounding the plasmonic square resonator is varied from 1.0 to 1.01. Figure 5

shows the transmission intensity as a function of the refractive index of materials surrounding the plasmonic square resonator. Figure 37 also shows a magnified view of refractive index range from 1.0 to $1.0+10^{-7}$. As shown in Fig. 37 the transmission intensity decreases when the refractive index of materials surrounding the plasmonic square resonator increases. It was found that the difference of the transmission intensity could be seen when the refractive index changed from 1.0 to $1.0+10^{-6}$.

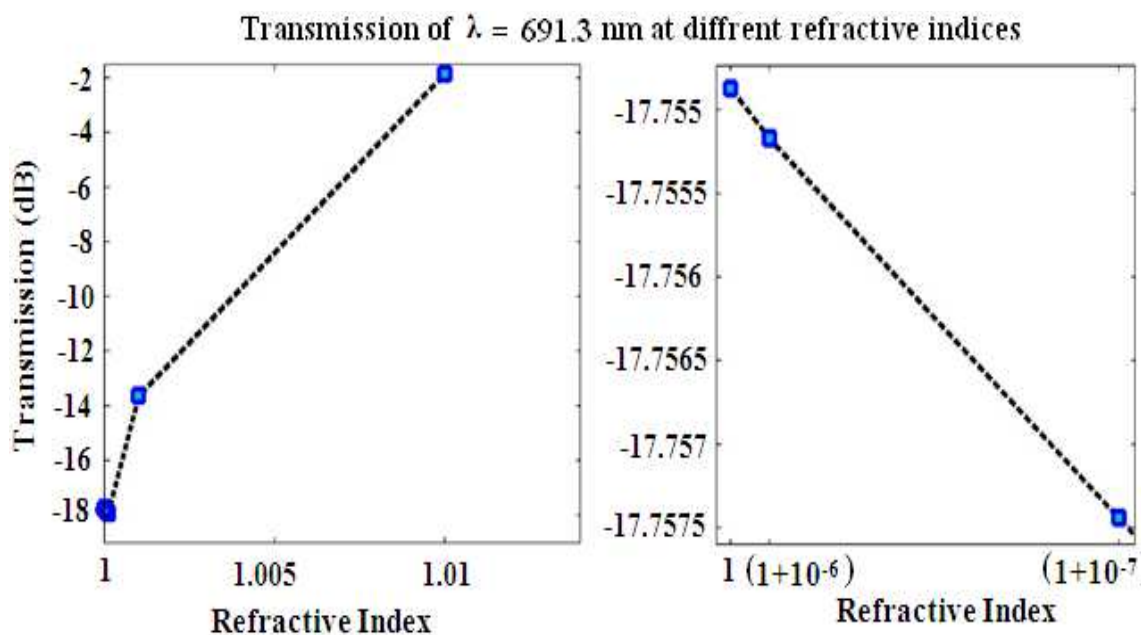


Figure 37. Transmission intensity at the wavelength of 691 nm as a function of the refractive index changes of materials surrounding the plasmonic square resonator. The transmission intensity decreases when the refractive index of materials surrounding the plasmonic square resonator increases. The difference of the transmission intensity could be seen when the refractive index changed from 1.0 to $1.0+10^{-6}$. However, the difference of the transmission intensity could not be distinguished when the refractive index changed from 1.0 to $1.0+10^{-7}$

However, the difference of the transmission intensity could not be distinguished when the refractive index changed from 1.0 to $1.0+10^{-7}$. Therefore, the detection limit of the refractive index change is 10^{-6} . The highest detection limit of existing system is 10^{-6} RIU.

The detection limit of our proposed plasmonic square resonator is almost same as the existing system that has the highest detection limit.

4.6 Sensitivity Analysis of the Proposed Sensor

In order to analyze the sensitivity of the proposed sensor to the design and fabrication parameters, various simulations have been performed. For example, the effect of the gap changes examined is shown in Fig. 38 for different gap sizes.

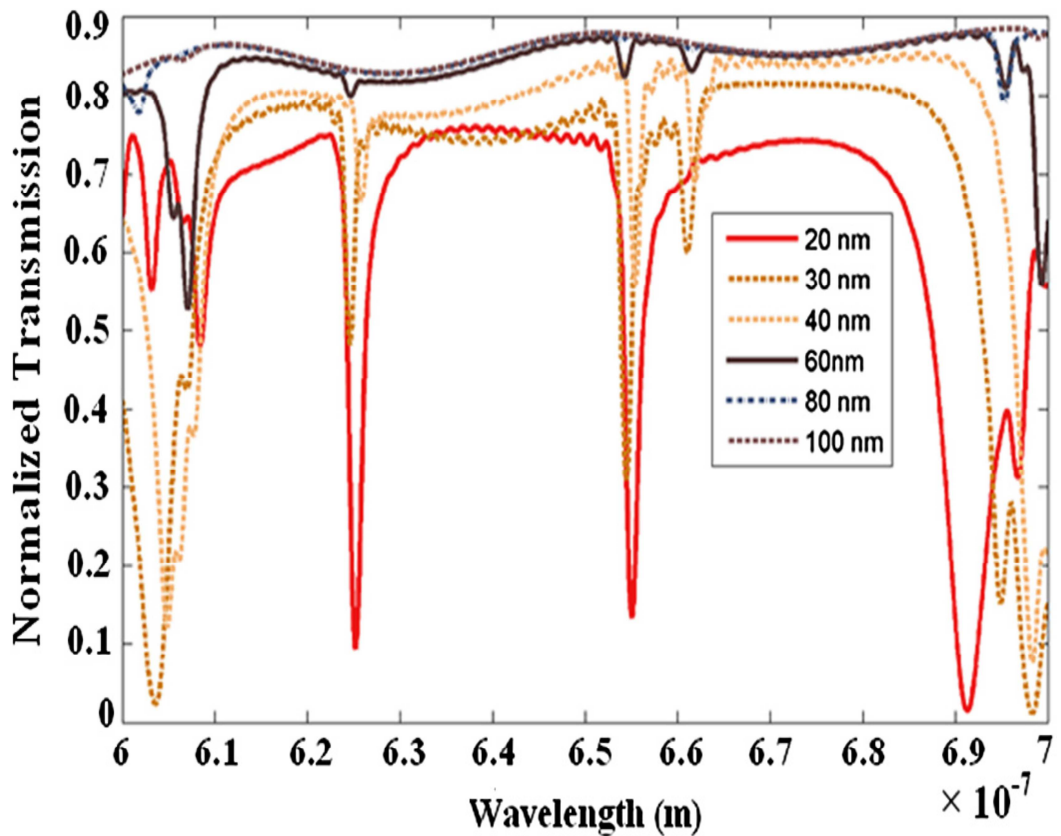


Fig. 38 Transmission intensity as a function of the wavelength for different gap sizes.

The gap size, of course, is one of the important design parameters as it controls the amount of the power coupled to the resonator. Increasing the gap size effect causes a small shift in the resonance wavelength. It also causes deterioration in the power coupled to the resonator due to the increase of the gap size over the skin depth of the optical field inside the optical metals at the visible band, which is limited to a few tens of nanometers. Thus, it is obvious from the figure that for gap size of >40 nm, the resonance power starts to diminish. Thus, based on these results, a value of <40 nm for the gap size is required to ensure acceptable performance of the resonator. The change in the refractive index has a negligible effect on the resonance of the proposed structure.

The effect of fabrication imperfections in the design parameters has also been investigated by examining 10% change in the gap size, as shown in Fig. 39.

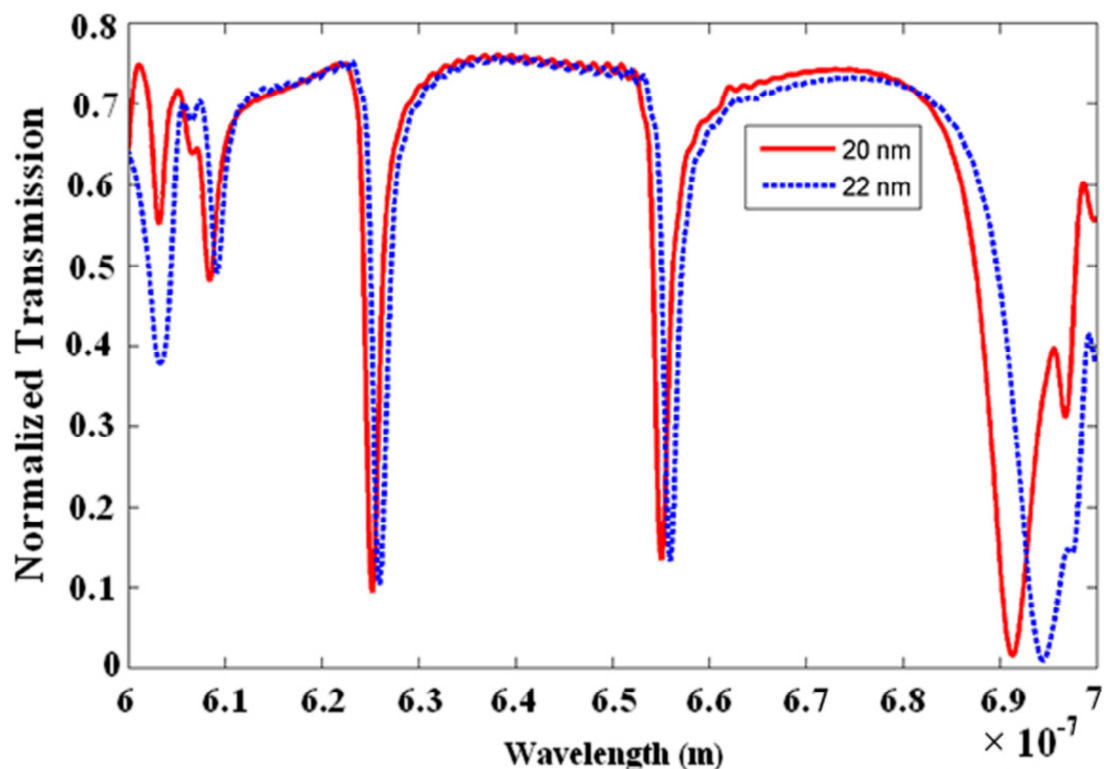


Fig. 39 Transmission intensity as a function of the wavelength for gap of 20 nm and gap of 22 nm.

It is clear that a small shift in the resonance wavelength occurs due to the change in the gap size.

Figure 40, also shows the response due to a change in the resonator dimension change by 10% in each direction to result in a resonator of $1.8 \times 1.8 \mu\text{m}$. Based on the results from Figs. 39 and 40, it is clear that working at the wavelength of 525 nm is less sensitive to the fabrication of the design parameters. Thus, if the fabrication process requires high tolerance, it may be more suitable to utilize the resonance at 625 nm. This resonance has the same sensitivity as the one at 692 nm, as shown in Fig. 40. It also has less sensitivity to the fabrication parameters, and hence, it may be more suitable for a fabrication process with large tolerance.

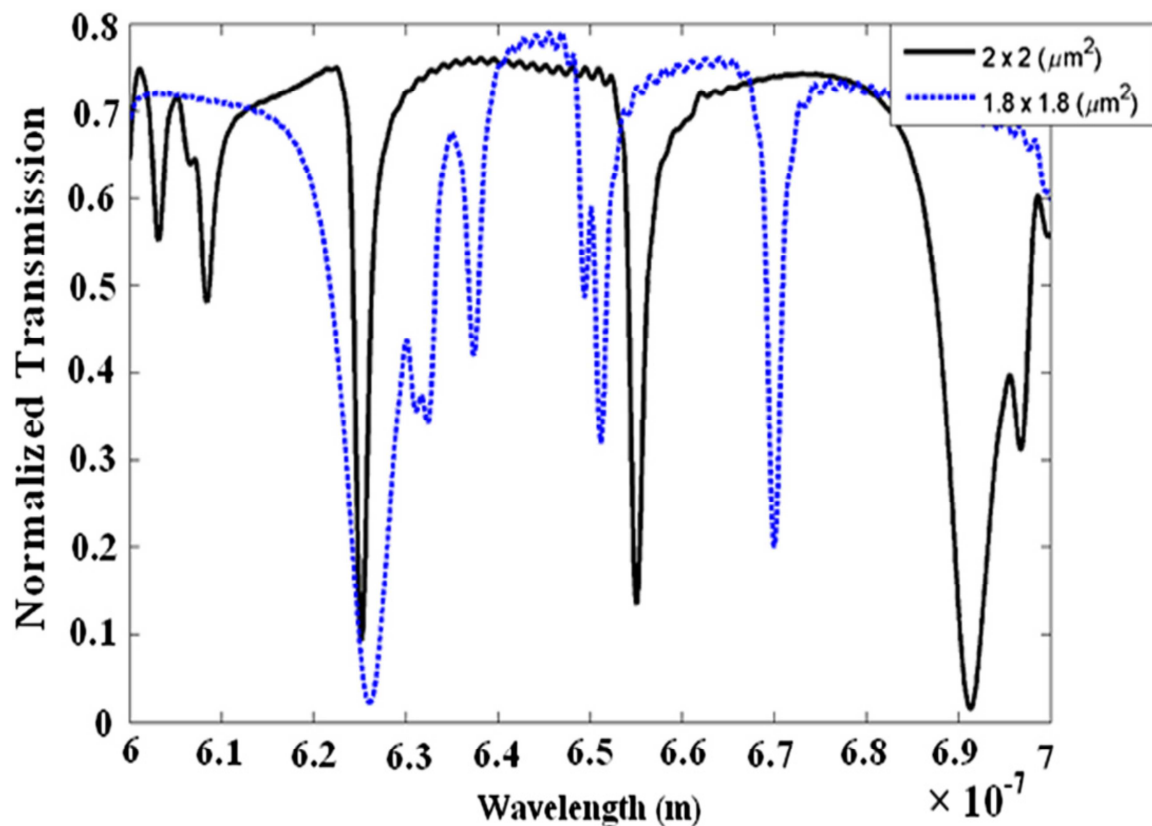


Figure 40 Transmission intensity as a function of different square resonator dimensions.

CONCLUSION

We have proposed a sensing system using the plasmonic resonator for detecting minor changes of the refractive index. Our proposed sensor is compact and can easily be utilized for integrated on chip system for lab-on-chip application. The sensor is associated with a sensitivity of 700 nm/RIU and a high detection limit, which could reach to 10^{-6} RIU. The sensor utilizes square shape resonator as the key sensing element. This resonator can be utilized as a size selector that detects particles with size smaller than its size only which can fit inside it. Thus, by controlling the size of this resonator, the upper limit of particle size that can be detected is also controlled. Our proposed sensor could be used in gas- and liquid-phase chemical sensing. In addition this sensor could be utilized for biosensing thus, by capturing of biomolecules producing a sensing signal that enables quantification of the biomolecules in a sample. The proposed structure opens the door for a high-sensitivity on-chip sensor using the plasmonic silicon hybrid technology toward practicable realization for lab-on-chip system.

CHAPTER 5

GENERAL CONCLUSIONS & FUTURE WORK

5.1 General Conclusions

Current micro-scale electronics technology has been approaching rapidly towards its technological limit. This has shifted the focus towards nano-scale technology in recent years. More and more researchers around the world are working for bringing nano-scale technology into mainstream.

The research carried out here was a small step towards a similar goal. Novel nanofabrications and nanostructures were fabricated, developed and optimized. The resulted nanofabrications could help to investigate novel optoelectronic and nanophotonic devices. So the research described here is a little step combining the worlds of nanophotonics and optoelectronics.

In chapter 2 and chapter 3, our research revolves around two kinds of nanofabrications. One of which was based on (Si) silicon. PSi and SiNWs have been the focus of intensive research due to their unique physical morphology and the associated electrical, mechanical, and thermal properties. PSi and SiNWs were main the main Si nanostructures we have been fabricated. Psi was fabricated using electrochemical etching of Si in HF solution. SiNWs were fabricated using an improved metal-assisted electroless etching of Si in $\text{KMnO}_4/\text{AgNO}_3/\text{HF}$ solution. In chapter 3, the formation mechanism of SiNWs was discussed. SEM miographies were performed to study the morphology of SiNWs.

In chapter 2 and chapter 3 the synthesis and fabrication of the conducting polymers Nanopolyaniline (NPANI) and its derivative poly Ortho-Toluidine (POT) was discussed. In chapter 2, the morphological, structural and optical properties of the fabricated NPANI were characterized by SEM, TEM, FTIR and UV-visible techniques.

Different parameters for the assembled NPANI/PSi heterojunction were calculated from I–V measurements performed in the dark conditions in the temperature range 298–373 K. It has been found that while the zero-bias barrier height decreases, ideality factor increases with decreasing temperature. This behavior has been attributed to particular distribution of barrier heights, barrier inhomogeneity, and interface states localized at the NPANI/PSi SBD. The calculated ideality factor (2.8-5.45) indicates that NPANI/PSi SBD represents a non-ideal diode.

The series resistance values are decreased with increasing temperature, which was attributed to the factors responsible for increase in η and/or to the lack of free carriers at low temperatures.

The results suggested that the NPANI was covalently grafted onto the PSi surface, and polymerization took place throughout the porous layer.

In chapter 3, We have succeeded to fabricate a high quality NPOT/SiNWs heterojunction through economical cheap and simple techniques in all stages of fabrication processes. The device presented a reproducibility of electrical characteristics, good rectifying behavior, of low turn on voltage (0.3 volts), saturation current of ($I_0 5.328 \times 10^{-7}$ A), ideality factor becomes close to 2, series resistance (1.4 K Ω) and barrier height (0.79 eV).

In chapter 4, a different type of nano-structure developed and investigated. The nanostructure proposed in chapter 4 was based upon nano-metallic design which serves as a plasmonic nanosensor to detect minor changes of refractive index. The proposed plasmonic nanosensor was based on square resonator. Our proposed sensor is compact and can be easily utilized for integrated on chip system for lab on chip application. The sensor was associated with a sensitivity of 700 nm/RIU and high detection limit which could reach to 10^{-6} RIU. The sensor utilize square shape resonator as the key sensing element which is easily to be fabricated using FIB milling. This resonator also can be utilized as size selector that detect particle with size smaller than its size only which can fit inside it. Thus, by controlling the size of this resonator, the upper limit of particle size that can be detected is also controlled.

5.2 Future Work

Part of the intended and possible future work introduced here is connected to the present work already done. Possible future research could be done through optimizing or improving the introduced nanofabrications and nanostructures or finding further and future applications.

For example, in chapter 3, we are presently performing experiments to investigate the conduction mechanisms of NPOT/SiNWs in more details.

Also the fabricated SiNWs could play an important role in providing a large effective junction area which could help in light trapping helping in solar cell applications [150] which is considered as a future point of research to use conducting polymers/SiNWs heterojunction to serve as a hybrid solar cell candidate.

In chapter 4, the proposed plasmonic nanosensor could be easily fabricated using the FIB milling technique. We are presently performing the fabrication of the proposed sensor using FIB milling technique to be able to experimentally characterize the real fabrication of the proposed design. It is so important to attain the experimental results of the real fabrication then compare to the simulation results.

Our suggested method of fabrication was done by milling of silver layer using FIB milling. The fabrication method started by evaporating a silver film with a thickness of 700 nm on a quartz glass substrate or Si substrate.

Then, we milled the layer of silver to a depth of 500 nm using the FIB technique. The width, depth, and waveguide-square gap are 40 nm, 500 nm, and 100 nm, respectively. As noted we started to fabricate a gap of 40 nm. Our plan is to decrease the gap gradually and see the possibility to reach to the minimum and possible gap width.

Another possible future and hot research which could be considered almost new could be done based on SiNWs fabrications. The idea based on fabrication of a novel metallic nanostructure which is Silver-coated SiNWs.

Based on plasmonic resonance, Silver-coated SiNWs nanofabrication could serve as Surface Enhanced Raman Spectroscopy (SERS) device. Some recent contributions were related to SiNWs -based highly-efficient SERS were reported [79-81].

We are presently performing the fabrication of a metal nano-array of Silver-coated SiNWs arrays. Silver-coated SiNWs arrays were prepared for molecular sensing and label-free immunoassay sensing of SERS signals, using rhodamine 6G (R6G) molecules. our the future fabrications of Silver-coated SiNWs nanofabrication for SERS applications the idea is

to fabricate SiNWs with the same improved metal-assisted electroless etching of silicon in $\text{KMnO}_4/\text{AgNO}_3/\text{HF}$ solution mentioned in chapter 3. This method of fabrication is a low cost technique to fabricate SiNWs compared some other fabrication methods used to use SiNWs for SERS by nanolithography. SiNWs fabrication will be followed by deposition of silver (30 or 40 nm) by thermal evaporation. Finally the molecular sensing and label-free immunoassay sensing of SERS signals, using deposition of rhodamine 6G (R6G) molecules.

REFERENCES

- [1] M.Deal, Nanotechnology, Stanford (Online article, last access 3 March 2014)
<http://snf.stanford.edu/Education/Nanotechnology.SNF.web.pdf>
- [2] Buffat P. and J. P. Borel, “Size effect on the melting temperature of gold particles,”
Phys. Rev. A, 13 (6), pp.2287-2298 (1976); <http://dx.doi.org/10.1103/PhysRevA.13.2287>
- [3] Susie Eustis and Mostafa A. El-Sayed “Why gold nanoparticles are more precious than
pretty gold: Noble metal surface plasmon resonance and its enhancement of the
radiative and nonradiative properties of nanocrystals of different shapes,” Chem. Soc.
Rev., 35, pp.209–217 (2006); <http://dx.doi.org/10.1039/b514191e>
- [4] Z. L. Wang and W. Wu, “Nanotechnology-Enabled Energy Harvesting for Self-
Powered Micro-/Nanosystems,” Angew. Chem. Int. Ed. 51(47) (2012);
<http://dx.doi.org/10.1002/anie.201201656>
- [5] Mihail C. Roco, Chad A. Mirikin and Mark C. Hersam, “Nanotechnology research
directions for societal needs in 2020: summary of international study,” J. Nanopart.
Res. 13(3) pp.897-919 (2011); <http://dx.doi.org/10.1007/s11051-011-0275-5>
- [6] A. R. Jha, “MEMS and Nanotechnology-Based Sensors and Devices for
Communications, Medical and Aerospace Applications,” CRC Press (2008);
<http://dx.doi.org/10.1201/9780849380709>
- [7] T. Steiner, “Semiconductor Nanostructures for Optoelectronic Applications,” Artech
House Semiconductor Materials and Devices Library, Artech House Publishers (July
2004).
- [8] P. Boisseau, P. Houdy and M. Lahmani, “Nanoscience: Nanobiotechnology and
Nanobiology,” Springer Heidelberg Dordrecht London, New York (2009);
<http://dx.doi.org/10.1007/978-3-540-88633-4>
- [9] Jau Su Yu et al., “Semiconductor nanostructures towards optoelectronic device
applications,” Proc. SPIE 8268, Quantum Sensing and Nanophotonic Devices IX,
82680A (January 20, 2012); <http://dx.doi.org/10.1117/12.907968>

- [10] Z. Zalevsky and I. Abdulhalim, "Integrated Nanophotonic Devices (Micro and Nano Technologies)," William Andrew 1 edition (November 4, 2010).
- [11] K. A. Jackson and W. Schroter, "Handbook of Semiconductor Technology," Volume 2 Wiley-VCH Verlag GmbH (1998); <http://dx.doi.org/10.1002/9783527619290>
- [12] A. Bose, S. Puri, and P. Banerjee, "Modern Inertial Sensors and Systems," PHI learning Private Limiting, New Delhi (2008).
- [13] N. Maluf and K. Williams, "An Introduction to Microelectromechanical Systems Engineering," Second Edition, Artech House Publishers. (2004).
- [14] M.A. Mohammad et al., "Fundamentals of Electron Beam Exposure and Development," Ch 2 in Nanofabrication, M. Stepanova and S. Dew, Eds., Springer: New York, , pp. 11–41 (Dec. 2011); http://dx.doi.org/10.1007/978-3-7091-0424-8_2
- [15] S. Hang et al., "Direct helium ion milling technology: towards the fabrication of extremely down-scaled graphene nanodevices", Silicon Nanoelectronics Workshop (SNW), Kyoto, JP (2013) <http://eprints.soton.ac.uk/id/eprint/352172>
- [16] E. Ozbay, "Plasmonics: Merging Photonics and Electronics at Nanoscale Dimensions," Science 311(5758) pp. 189-193 (2006); <http://dx.doi.org/10.1126/science.1114849>
- [17] R. B. Nielsen et al., "Channel plasmon polariton propagation in nanoimprinted V-groove waveguides," Opt. Lett. 33(23) pp. 2800-2802 (2008); <http://dx.doi.org/10.1364/OL.33.002800>
- [18] "Techniques for synthesis of nanomaterials," Pdf online lecture; http://www.ttu.ee/public/m/Mehaanikateaduskond/Instituudid/Materjalitehnika_instituut/MTX9100/Lecture11_Synthesis.pdf (last access to the page was in Jan 2014)
- [19] Philip Coane, "Introduction to Electron Beam Lithography," online pdf, [http://140.120.11.121/~denda/Upload/paper/\[11\]Introduction%20to%20Electron%20Beam%20Lithography.pdf](http://140.120.11.121/~denda/Upload/paper/[11]Introduction%20to%20Electron%20Beam%20Lithography.pdf) (last access to the page was in Jan 2014)
- [20] Alireza Samavat et al., "Germanium nanoislands grown by radio frequency magnetron sputtering: Annealing time dependent surface morphology and photoluminescence,"

- Chin. Phys. B, 22 (9) pp. 098102-1-5 (2013); <http://dx.doi.org/10.1088/1674-1056/22/9/098102>
- [21] Benjamin Bruhn et al., “Transition from silicon nanowires to isolated quantum dots: Optical and structural evolution,” *Physical Review B*, 87(4) (2013); <http://dx.doi.org/10.1103/PhysRevB.87.045404>
- [22] M. B. de la Mora et al., “Porous Silicon Biosensors,” Chapter 6 in *State of the Art in Biosensors - General Aspects*, (March 13, 2013) <http://dx.doi.org/10.5772/52975>
- [23] Z. Zalevsky and I. Abdulhalim, “Integrated Nanophotonic Devices (Micro and Nano Technologies),” William Andrew (2010).
- [24] H. Zappe, “Fundamentals of Micro-Optics,” Cambridge University press (2010); <http://dx.doi.org/10.1017/CBO9780511781797>
- [25] D. J. Harrison and A. Berg, “Micro total analysis systems 98,” Kluwer Academic publisher. (2000); <http://dx.doi.org/10.1007/978-94-011-5286-0>
- [26] P. Pal and K. Sato, “Fabrication methods based on wet etching process for the realization of silicon MEMS structures with new shapes,” *Microsystem Technologies*, 16 (7), pp. 1165–1174 (2010); <http://dx.doi.org/10.1007/s00542-009-0956-5>
- [27] N. K. A. A-baidi, “Fabrication and characterization of electrochemically formed nanocrystalline porous Si and GaAs,” Doctoral thesis, Universiti Sains Malaysia (2008); http://eprints.usm.my/9893/1/FABRICATION_AND_CHARACTERIZATION_OF.pdf
- [28] E. X Pérez, “Design, Fabrication and characterization of porous silicon multilayer optical devices,” Doctoral thesis, Universitat Rovirai Virgili (2007); <http://www.tdx.cat/handle/10803/8458>
- [29] N. Chiboub et al., “Covalent grafting of polyaniline onto aniline-terminated porous silicon,” *J. Opt. Mat.* 32(7), pp. 748–752 (2010); <http://dx.doi.org/10.1016/j.optmat.2010.02.007>
- [30] P N Patel et al., “Theoretical and experimental study of nanoporous silicon photonic microcavity optical sensor devices,” *Adv. Nat. Sci.: Nanosci. Nanotechnol.*, 3(3) 035016 (pp.1-7) (2012); <http://dx.doi.org/10.1088/2043-6262/3/3/035016>

- [31] K. S. Khashan, A. A. Awaad and M. A. Mohamed, "Effect on Rapid Thermal Oxidation process on Electrical Properties of Porous Silicon," Eng. & Tech. J. vol. 27, pp. 663-674 (2009); <http://www.iasj.net/iasj?func=fulltext&aId=29195>
- [32] Kasra Behzad et al., "Effect of Preparation Parameters on Physical, Thermal and Optical Properties of n-type Porous Silicon," Int. J. Electrochem. Sci., 7, pp. 8266 - 8275 (2012); <http://www.electrochemsci.org/papers/vol7/7098266.pdf>
- [33] R. Herino., "Nanocomposite materials from porous silicon," Materials Science and Engineering B, 69-70(70) pp.70-76 (2000); [http://dx.doi.org/10.1016/S0921-5107\(99\)00269-X](http://dx.doi.org/10.1016/S0921-5107(99)00269-X)
- [34] M. Mynbaeva et al., "HVPE GaN growth on porous SiC with closed surface porosity," J. Cryst. Growth 303 (2) pp.472-479 (2007); <http://dx.doi.org/10.1016/j.jcrysgro.2006.12.041>
- [35] A. A. M Farag et al., "Fabrication and electrical characterization of n-InSb on porous Si heterojunctions prepared by liquid phase epitaxy," Microelectronics J. 39(2) pp.253-260 (2008); <http://dx.doi.org/10.1016/j.mejo.2007.10.029>
- [36] Ming-Liang Zhang et al., "Preparation of Large-Area Uniform Silicon Nanowires Arrays through Metal-Assisted Chemical Etching," J. Phys. Chem. C, 112 (12), pp.4444-4450 (2008) ; <http://dx.doi.org/10.1021/jp077053o>
- [37] Z. Li, "Sequence-Specific Label-Free DNASensors Based on Silicon Nanowires," Nano Lett., 4 (2), pp. 245-247 (2004); <http://dx.doi.org/10.1021/nl034958e>
- [38] Jong-in Hahm and Charles M. Lieber, "Direct Ultrasensitive Electrical Detection of DNA and DNA Sequence Variations Using Nanowire Nanosensors," Nano Lett., 4(1), pp.51-54 (2004); <http://dx.doi.org/10.1021/nl034853b>
- [39] Y. Cui, "Nanowire Nanosensors for Highly Sensitive and Selective Detection of Biological and Chemical Species," Science, 293(5533), pp. 1289-1292 (2001); <http://dx.doi.org/10.1126/science.1062711>
- [40] Y. Wang et al., "Epitaxial growth of silicon nanowires using an aluminium catalyst," Nature Nanotechnology, 1 (3) pp. 186-189 (2006); <http://dx.doi.org/10.1038/nnano.2006.133>
- [41] R. S. Wagner and W. C. Ellis, "Vapor-liquid-solid mechanism of single crystal growth," Appl. Phys. Lett. 4, pp.1053 -1064 (1964); <http://www.chem.sc.edu/faculty/greytak/chem749/wagner-trans-metall-soc-aime-1965-vls.pdf>

- [42] G.-C. Yi, "Semiconductor Nanostructures for Optoelectronic Devices," NanoScience and Technology, Springer-Verlag Berlin Heidelberg (2012); <http://dx.doi.org/10.1007/978-3-642-22480-5>
- [43] V. Sivakov et al., "Wet - Chemically Etched Silicon Nanowire Architectures: Formation and Properties," Ch3 in "Nanowires Fundamental research," <http://www.intechopen.com/download/get/type/pdfs/id/16561>
- [44] Z. Huang et al., "Metal-Assisted Chemical Etching of Silicon: A Review," Adv. Mater. 23 (2), pp. 285–308 (2011); <http://dx.doi.org/10.1002/adma.201001784>
- [45] V. Schmidt, S. Senz and U. Gosele, "Diameter-Dependent Growth Direction of Epitaxial Silicon Nanowires," Nano Lett. 5 (5), pp.931-935 (2005); <http://dx.doi.org/10.1021/nl050462g>
- [46] Z. Huang et al., "Oxidation rate effect on the direction of metal-assisted chemical and electrochemical etching of silicon," J. Phys. Chem. C, 114(24), pp.10683–10690 (2010); <http://dx.doi.org/10.1021/jp911121q>
- [47] Z. P. Huang et al., "Ordered Arrays of Vertically Aligned [110] Silicon Nanowires by Suppressing the Crystallographically Preferred <100> Etching Directions," Nano Lett. 9(7) pp. 2519-2525 (2009); <http://dx.doi.org/10.1021/nl803558n>
- [48] W. K. Choi, T. H. Liew and M. K. Dawood, "Synthesis of Silicon Nanowires and Nanofin Arrays Using Interference Lithography and Catalytic Etching," Nano Lett. 8(11) , pp.3799-3802 (2008); <http://dx.doi.org/10.1021/nl802129f>
- [49] J. de Boor et al., "Sub-100 nm silicon nanowires by laser interference lithography and metal-assisted etching," Nanotechnology, 21(9), 095302 (2010); <http://dx.org/10.1088/0957-4484/21/9/095302>
- [50] S. G. Cloutier et al., "Enhancement of Radiative Recombination in Silicon via Phonon Localization and Selection-Rule Breakin," Adv. Mater. 18 (7) , pp. 841-844 (2006); <http://dx.doi.org/10.1002/adma.200600001>
- [51] P. Kleimann, X. Badel and J. Linnros, "Toward the formation of three-dimensional nanostructures by electrochemical etching of silicon," Appl. Phys. Lett. , 86 (18), pp. 183108 (1-3) (2005); <http://dx.doi.org/10.1063/1.1924883>

- [52] A. I. Hochbaum et al., “Enhanced thermoelectric performance of rough silicon nanowires,” *Nature*, 451 (7175), pp. 163-168 (2008); <http://dx.doi.org/10.1038/nature06381>
- [53] A. G. MacDiarmid, “Synthetic metals: a novel role for organic polymers,” *Synth. Met.* 125(1), pp.11-22 (2001); [http://dx.doi.org/10.1016/S0379-6779\(01\)00508-2](http://dx.doi.org/10.1016/S0379-6779(01)00508-2)
- [54] J. Li et al., “A Gas sensor array using carbon nanotube and microfabrication technology,” *Electrochem. Solid State Lett.*, 8(11), pp.100–102 (2005); <http://dx.doi.org/10.1149/1.2063289>
- [55] Ali Eftekhari, “Nanostructured Conductive Polymers,” John Wiley & Sons Ltd (2010); <http://dx.doi.org/10.1002/9780470661338>
- [56] C. Batich, H.A. Laitinen and H.C. Zhou, “Chromatic Changes in Polyaniline Films,” *J. Electrochem. Soc.* 137 (3), pp. 883-885 (1990); <http://dx.doi.org/10.1149/1.2086572>
- [57] S. A. Sapp, G. R. Sotzing and J. R. Reynolds, “High Contrast Ratio and Fast Switching Dual Polymer Electrochromic Devices,” *J. R. Chem. Mater*, 10 (8), pp. 2101-2108 (1998); <http://dx.doi.org/10.1021/cm9801237>
- [58] D. Yaohua and M. Shaolin, “Photoelectrochemical behavior of polyaniline affected by potentials and pH of solutions,” *Electrochim. Acta.* 36(13), pp. 2015-2018 (1991); [http://dx.doi.org/10.1016/0013-4686\(91\)85087-N](http://dx.doi.org/10.1016/0013-4686(91)85087-N)
- [59] K. M. Zaidan et al., “Synthesis and characterization of poly (o-toluidine) POT blend with polyethylene oxide PEO as conducting polymer alloys,” *Der Chemica Sinica*, 3(4), pp.841-848 (2012); <http://pelagiaresearchlibrary.com/der-chemica-sinica/vol3-iss4/DCS-2012-3-4-841-848.pdf>
- [60] J. M. G. Laranjeira et al., “Conducting polymer/silicon heterojunction diode for gamma radiation detection,” *Nuclear Technology Publishing*, vol. 101, Nos. 1–4, pp. 85–88 (2002); downloaded from <http://rpd.oxfordjournals.org/> at The University of Tokushima on January 13, 2014.
- [61] Jorge Bravo-Abad and Francisco J. García-Vidal, “PLASMONIC LASERS, A sense of direction,” *News & Views, NATURE NANOTECHNOLOGY VOL 8 (JULY 2013)*; <http://www.uam.es/proyectosinv/plasmonq/pdfs/90.pdf>

- [62] S. Lal, S. Link and N. J. Halas, "Nano-optics from sensing to waveguiding," *Nature photonics*, 1(11), pp. 641-648 (2007); <http://dx.doi.org/10.1038/nphoton.2007.223>
- [63] R. Zia et al., "Plasmonics: the next chip-scale technology," *Materials Today*. 9(7-8), pp. 20-27 (2006); [http://dx.doi.org/10.1016/S1369-7021\(06\)71572-3](http://dx.doi.org/10.1016/S1369-7021(06)71572-3)
- [64] J. Moosburger et al., "Enhanced transmission through photonic-crystal-based bent waveguides by bend engineering," *Appl. Phys. Lett.* 79 (22), pp. 3579-3581 (2001); <http://dx.doi.org/10.1063/1.1421087>
- [65] S. A. MAIER, "PLASMONICS: FUNDAMENTALS AND APPLICATIONS," Springer Science+Business Media LLC (2007).
- [66] A E Cetin et al., "Handheld high-throughput plasmonic biosensor using computational on-chip imaging," *Light: Science & Applications*, 3(e122), pp. 1-10 (2014); <http://dx.doi.org/10.1038/lsa.2014.3>
- [67] C. Giancarlo, "An introduction to optoelectronic sensors," World Scientific Publishing (2009).
- [68] L. B. Sagle et al., "Advances in localized surface plasmon resonance spectroscopy biosensing," *Nanomedicine*, 6(8), pp.1447–1462 (2011); <http://dx.doi.org/10.2217/nmm.11.117>
- [69] J. Homola, S. S. Yee, and G. Gauglitz, "Surface plasmon resonance sensors: review," *Sensors and Actuators B*, 54(1-2) , pp. 3–15 (1999); [http://dx.doi.org/10.1016/S0925-4005\(98\)00321-9](http://dx.doi.org/10.1016/S0925-4005(98)00321-9)
- [70] James M. McDonnell, "Surface plasmon resonance: towards an understanding of the mechanisms of biological molecular recognition," *Curr. Opin. Chem. Biol.* 5(5) , pp. 572–577 (2001); [http://dx.doi.org/10.1016/S1367-5931\(00\)00251-9](http://dx.doi.org/10.1016/S1367-5931(00)00251-9)
- [71] H. J. Lee, A. W. Wark and R. M. Corn, "Enhanced bioaffinity sensing using surface plasmons, surface enzyme reactions, nanoparticles and diffraction gratings," *The Analyst*,133(5), pp. 596–601 (2008); <http://dx.doi.org/10.1039/b718713k>
- [72] C. Shad Thaxton and Chad A. Mirkin, "Plasmon coupling measures up," *Nat. Biotechnol.* 23(6) , pp. 681–682 (2005); <http://dx.doi.org/10.1038/nbt0605-681>

- [73] S. Chah, M. R. Hammond and R. N. Zare, "Gold nanoparticles as a colorimetric sensor for protein conformational changes," *Chem. Biol.* 12(3) , pp. 323–328 (2005); <http://dx.doi.org/10.1016/j.chembiol.2005.01.013>
- [74] B. M. Reinhard et al., "Calibration of dynamic molecular rule based on plasmon coupling between gold nanoparticles," *Nano Lett.* 5(11), pp. 2246–2252 (2005); <http://dx.doi.org/10.1021/nl051592s>
- [75] Reinhard BM et al., "Use of plasmon coupling to reveal the dynamics of DNA bending and cleavage by single EcoRV restriction enzymes," *Proc. Natl Acad. Sci. USA*, 104 (8), pp. 2667–2672 (2007); <http://dx.doi.org/10.1073/pnas.0607826104>
- [76] T. R. Jensen et al., "Nanosphere Lithography: Tunable Localized Surface Plasmon Resonance Spectra of Silver Nanoparticles," *J. Phys. Chem. B*, 104(45), pp.10549 - 10556 (2000); <http://dx.doi.org/10.1021/jp002435e>
- [77] Jian Feng Li et al., "Shell-isolated nanoparticle-enhanced Raman spectroscopy," 464(18), pp. 392-395 (2010); <http://dx.doi.org/doi:10.1038/nature08907>
- [78] Y. S. Huh and A. J. Chung, "Surface enhanced Raman spectroscopy and its application to molecular and cellular analysis," *Microfluid. Nanofluid.* 6 (3), pp. 6:285–297 (2009); <http://dx.doi.org/10.1007/s10404-008-0392-3>
- [79] Xuemei Han, "Silicon Nanowire-Based Surface-Enhanced Raman Spectroscopy Endoscope for Intracellular pH Detection," *ACS Appl. Mater. Interfaces*, 5(12), pp. 5811–5814 (2013); <http://dx.doi.org/10.1021/am401391g>
- [80] Yao He, "Silicon nanowires-based highly-efficient SERS-active platform for ultrasensitive DNA detection," *Nano Today*, 6(2), pp. 122-130 (2011); <http://dx.doi.org/10.1016/j.nantod.2011.02.004>
- [81] Xianzhong Sun, "Fabrication of silver-coated silicon nanowire arrays for surface-enhanced Raman scattering by galvanic displacement processes," *Applied Surface Science*, 256 (3), pp. 916–920 (2009); <http://dx.doi.org/10.1016/j.apsusc.2009.08.085>
- [82] E.T. Kang, K.G. Neoh and K.L. Tan, "Polyaniline: A Polymer with many interesting intrinsic redox states," *Prog. Polym. Sci.* 23 (2) , pp. 277-324 (1998); [http://dx.doi.org/10.1016/S0079-6700\(97\)00030-0](http://dx.doi.org/10.1016/S0079-6700(97)00030-0)

- [83] H. Namazi, R. Kabiri and A. Entezami, "Determination of extremely low percolation threshold electroactivity of the blend polyvinyl chloride/polyaniline doped with camphorsulfonic acid by cyclic voltammetry method," *Euro. Polym. J.* 38(4), pp. 771-777 (2002); [http://dx.doi.org/10.1016/S0014-3057\(01\)00232-4](http://dx.doi.org/10.1016/S0014-3057(01)00232-4)
- [84] A. J. MacDiarmid et al., "Electrochemical Characteristics of "Polyaniline" Cathodes and Anodes in Aqueous Electrolytes," *Mol. Cryst. Liq. Cryst.* 121(1-4), pp. 187-190 (1985); <http://dx.doi.org/10.1080/00268948508074859>
- [85] P. Novák et al., "Electrochemically Active Polymers for Rechargeable Batteries," *Chem. Rev.* 97(1), pp. 207-282, (1997); <http://dx.doi.org/10.1021/cr941181o>
- [86] C. Batich, H.A. Laitinen and H.C. Zhou, "Chromatic Changes in Polyaniline Films," *J. Electrochem. Soc.* 137(3), pp. 883-885 (1990); <http://dx.doi.org/10.1149/1.2086572>
- [87] S. A. Sapp, G. R. Sotzing and J. R. Reynolds, "High Contrast Ratio and Fast Switching Dual Polymer Electrochromic Devices," *J. R. Chem. Mater.* 10 (8), pp. 2101-2108 (1998); <http://dx.doi.org/10.1021/cm9801237>
- [88] N. F. Atta, A. Galal and H. M. A. Amin, "Synthesis and Photoelectrochemical Behavior of a Hybrid Electrode Composed of Polyaniline Encapsulated in Highly Ordered TiO₂ Nanotubes Array," *Int. J. Electrochem. Sci.*, 7, 2012
- [89] S. Tan et al., "Property Influence of Polyanilines on Photovoltaic Behaviors of Dye-Sensitized Solar Cells," *Langmuir* 20 (7), pp. 2934-2937 (2004) <http://dx.doi.org/10.1021/la036260m>
- [90] J. Jang et al., "Organic light-emitting diode with polyaniline-poly (styrene sulfonate) as a hole injection layer," *Thin Solid Films*, 516 (10), pp. 3152- 3156 (2008); <http://dx.doi.org/10.1016/j.tsf.2007.08.088>
- [91] S.A. Chen et al., "White- light emission from electroluminescence diode with polyaniline as the emitting layer", *Synth. Met.* 82 (3), pp. 207-210 (1996); [http://dx.doi.org/10.1016/S0379-6779\(96\)03790-3](http://dx.doi.org/10.1016/S0379-6779(96)03790-3)
- [92] Q. Li et al., "Application of microporous polyaniline counter electrode for dye-sensitized solar cells," *Electrochem. Comm.* 10(9), pp. 1299 -1302 (2008); <http://dx.doi.org/10.1016/j.elecom.2008.06.029>

- [93] S.X. Tan et al., "Polyaniline as hole transport material to prepare solid solar cells," *Synth. Met.* 137 (1-3), pp. 1511-1512, (2003); [http://dx.doi.org/10.1016/S0379-6779\(02\)01207-9](http://dx.doi.org/10.1016/S0379-6779(02)01207-9)
- [94] X.Y. Zhang, W.J. Goux and S.K. Manohar, "Synthesis of polyaniline nanofibers by nanofiber seeding," *J. Am. Chem. Soc.* 126 (14), pp. 4502-4503 (2004); <http://dx.doi.org/10.1021/ja031867a>
- [95] Y. Y. Wang and X. L. Jing, "Intrinsically Conducting Polymers for Electromagnetic Interference Shielding," *Polym. Adv. Technol.* 16 (4), pp. 344-351 (2005); <http://dx.doi.org/10.1002/pat.589>
- [96] Omed Gh. Abdullah et al., "Electrical Characterization of Polyester Reinforced by Carbon Black Particles," *International Journal of Applied Physics and Mathematics*, 1(2), pp. 101-105 (2011); <http://dx.doi.org/10.7763/IJAPM.2011.V1.20>
- [97] E. F. Barbosa, "Immobilization of Peroxidase onto Magnetite Modified Polyaniline," *The Scientific World Journal*, 2012, pp. 1-5 (2012); <http://dx.doi.org/10.1100/2012/716374>
- [98] P. C de Leon et al., "Conducting polymer coatings in electrochemical technology Part 2 – Application areas," *Maney Publishing*, 86 (1), pp. 34-40 (2008) <http://dx.doi.org/10.1179/174591908X264392>
- [99] A. Kalendova et al., "Anticorrosion properties of inorganic pigments surface-modified with a polyaniline phosphate layer," *Prog. Org. Coat.* 63 (2), pp. 209-221 (2008); <http://dx.doi.org/10.1016/j.porgcoat.2008.06.001>
- [100] J. C. Chiang and A. G. MacDiarmid, "Polyaniline": Protonic acid doping of the emeraldine form to the metallic regime," *Synth. Met.* 13(1-3), pp.193-205 (1986); [http://dx.doi.org/10.1016/0379-6779\(86\)90070-6](http://dx.doi.org/10.1016/0379-6779(86)90070-6)
- [101] D. Zhang and Y. Y. Wang, "Synthesis and applications of one-dimensional nano-structured polyaniline: An overview," *Mater. Sci. Eng. B*, 134 (1), pp. 9-19 (2006); <http://dx.doi.org/10.1016/j.mseb.2006.07.037>
- [102] J.X. Huang et al., "Polyaniline Nanofibers: Facile Synthesis and Chemical Sensors," *J. Am. Chem. Soc.* 125 (2), pp. 314-315 (2003); <http://dx.doi.org/10.1021/ja028371y>

- [103] J. X. Huang and R. B. Kaner, "Nanofiber Formation in the Chemical Polymerization of Aniline: A Mechanistic Study," *Angew. Chem.* 116 (43), pp. 5941-5945 (2004); <http://dx.doi.org/10.1002/ange.200460616>
- [104] S.E. Moulton et al., "Polymerisation and characterisation of conducting polyaniline nanoparticle dispersions," *Curr. Appl. Phys.* 4 (2-4), pp. 402-406 (2004); <http://dx.doi.org/10.1016/j.cap.2003.11.059>
- [105] M. Mynbaeva et al., "HVPE GaN growth on porous SiC with closed surface porosity," *J. Cryst. Growth*, vol. 303, pp. 472-479 (2007); <http://dx.doi.org/10.1016/j.jcrysgro.2006.12.041>
- [106] Y. J. Mii et al., "Studies of molecular-beam epitaxy growth of GaAs on porous Si substrates," *J. Vac. Sci. Technol. B*, 6(2), pp. 696-698 (1988); <http://dx.doi.org/10.1116/1.584395>
- [107] M. Yin and A. Krier, "Liquid Phase Epitaxial Growth and Characterization of InSb on Cd_{0.955} Zn_{0.045} Te," Physics Department, Lancaster University <http://www.lancaster.ac.uk/staff/yinm1/LPE%20growth%20and%20characterization%20of%20InSb---NASM3.pdf>
- [108] S. R. Forrest, M. L. Kaplan and P.H. Schmidt, "Organic- on- inorganic semiconductor contact barrier diodes. I. Theory with applications to organic thin films and prototype devices," *J. Appl. Phys.* 55 (6) , pp. 1492-1507 (1984); <http://dx.doi.org/10.1063/1.333407>
- [109] W. Wang, E. Schiff and Q. Wang "Amorphous silicon/polyaniline heterojunction solar cells: Fermi levels and open-circuit voltages," *Journal of Non-Crystalline Solids* 354(19-25) pp. 2862-2865 (2008); <http://dx.doi.org/10.1016/j.jnoncrysol.2007.10.104>
- [110] W. Wang and E.A. Schiff. "Polyaniline on crystalline silicon heterojunction solar cells," *Appl. Phys. Lett.* 91 (13) , pp. 133504-133506 (2007); <http://dx.doi.org/10.1063/1.2789785>
- [111] E. A. T. Dirani et al., "Study of heterojunction diodes using POMA/PANI and amorphous/microcrystalline silicon structures," *Synth. Met.* vol. 121, pp. 1545.-1546, (2001); [http://dx.doi.org/10.1016/S0379-6779\(00\)01221-2](http://dx.doi.org/10.1016/S0379-6779(00)01221-2)

- [112] N. Chiboub et al., "Covalent grafting of polyaniline onto aniline-terminated porous silicon," *J. Opt. Mat.* 32 (7), pp. 748-752 (2010); <http://dx.doi.org/10.1016/j.optmat.2010.02.007>
- [113] C.A. Betty, "Highly sensitive capacitive immunosensor based on porous silicon– polyaniline structure: Bias dependence on specificity," *Biosens. and Bioelectron.* 25 (2), pp. 338-343 (2009); <http://dx.doi.org/10.1016/j.bios.2009.07.009>
- [114] J. Fan, M. Wan and D. Zhu "Studies on the rectifying effect of the heterojunction between porous silicon and water-soluble copolymer of polyaniline," *Synth. Met.* 95 (2), pp. 119-124 (1998); [http://dx.doi.org/10.1016/S0379-6779\(98\)00043-5](http://dx.doi.org/10.1016/S0379-6779(98)00043-5)
- [115] Ş. Aydoğan, M. Sağlam and A. Türüt. "On the barrier inhomogeneities of polyaniline/p-Si/Al structure at low temperature," *Appl. Surf. Sci.* 250 (1-4), pp. 43 - 49 (2005); <http://dx.doi.org/10.1016/j.apsusc.2004.12.020>
- [116] Y. Guo and Y. Zhou "Polyaniline nanofibers fabricated by electrochemical polymerization: A mechanistic study," *Euro. Polym. J.* 43 (6), pp. 2292-2297 (2007); <http://dx.doi.org/10.1016/j.eurpolymj.2007.01.020>
- [117] N. J. Pinto et al., "Electric response of isolated electrospun polyaniline nanofibers to vapors of aliphatic alcohols," *Sensors & Actuators B: Chem.* 129 (2), pp.621-627 (2008); <http://dx.doi.org/10.1016/j.snb.2007.09.040>
- [118] Z. Wang, M. Chen and H-L. Li, "Preparation and characterization of uniform polyaniline nano-fibrils using the anodic aluminum oxide template," *Mater. Sci. Eng. A.* 328 (1-2), pp. 33-38 (2002) ; [http://dx.doi.org/10.1016/S0921-5093\(01\)01695-1](http://dx.doi.org/10.1016/S0921-5093(01)01695-1)
- [119] Z. Zhang, J. Deng and M. Wan "Highly crystalline and thin polyaniline nanofibers oxidized by ferric chloride," *Mater. Chem. Phys.* 115 (1), pp. 275-279 (2009); <http://dx.doi.org/10.1016/j.matchemphys.2008.12.005>
- [120] E. H. Rhoderick, and R.H. Williams *Metal Semiconductor Contacts*, second ed. (Oxford, Clarendon) 1988.
- [121] Ş. Aydoğan, M. Sağlam and A. Türüt. "Some electrical properties of polyaniline/p-Si/Al structure at 300 K and 77 K temperatures," *Microelectron. Eng.* 85 (2), pp. 278-283 (2008); <http://dx.doi.org/10.1016/j.mee.2007.06.004>

- [122] M. Pattabi, S. Krishnan and X. Mathew. "Effect of temperature and electron irradiation on the I–V characteristics of Au/CdTe schottky diodes," *Sol. Energy.* 81 (1), pp. 111–116 (2007); <http://dx.doi.org/10.1016/j.solener.2006.06.004>
- [123] DT. Quan and H. Hbib "High barrier height Au/n-type InP Schottky contacts with a POXNyHz interfacial layer," *Solid. State. Electron.* 36 (3) , pp. 339-344 (1993); [http://dx.doi.org/10.1016/0038-1101\(93\)90085-5](http://dx.doi.org/10.1016/0038-1101(93)90085-5)
- [124] Gümüő, A. Türüt, and N. Yalçın "Temperature dependent barrier characteristics of CrNiCo alloy Schottky contacts on n-type molecular-beam epitaxy GaAs," *J. Appl. Phys.* 91 (1), pp. 245-250 (2002); <http://dx.doi.org/10.1063/1.1424054>
- [125] C. Coskun, M. Biber and H. Efeoglu. "Temperature dependence of current–voltage characteristics of Sn/p-GaTe Schottky diodes," *Appl. Surf. Sci.* 211 (1-4), p. 363 (2003); [http://dx.doi.org/10.1016/S0169-4332\(03\)00267-8](http://dx.doi.org/10.1016/S0169-4332(03)00267-8)
- [126] H. Werner and H.H. Guttler "Barrier inhomogeneities at Schottky contacts," *J. Appl. Phys.* 69 (3), pp. 1522-1533, (1991); <http://dx.doi.org/10.1063/1.347243>
- [127] C. A. Dimitriadis, S. Logothetidis, and I. Alexandrou "Schottky barrier contacts of titanium nitride on n-type silicon," *Appl. Phys. Lett.* 66 (4), Jan 1995, pp. 502-504, (1995); <http://dx.doi.org/10.1063/1.114070>
- [128] N. Tugluglu et al., "Temperature dependence of current–voltage characteristics of Ag/p-SnSe Schottky diodes," *Appl. Surf. Sci.* 233 (1-4), pp. 320-327 (2004); <http://dx.doi.org/10.1016/j.apsusc.2004.03.238>
- [129] Y. Xia, K. Sun, and J. Ouyang, "Solution-Processed Metallic Conducting Polymer Films as Transparent Electrode of Optoelectronic Devices," *Adv. Mater.* 24 (18), pp. 2436–2440 (2012); <http://dx.doi.org/10.1002/adma.201104795>
- [130] S. Cho et al., "Enhanced Electrochemical Performance of Highly Porous Supercapacitor Electrodes Based on Solution Processed Polyaniline Thin Films, ACS," *Appl. Mater. Interfaces*, 2013, 5 (18), pp. 9186–9193(2013); <http://dx.doi.org/10.1021/am402702y>

- [131] M. K. Ram et al., "Electrochemical and optical characteristics of conducting poly(o-toluidine) films," *Thin Solid Films*, 304 (1-2), pp. 65–69 (1997); [http://dx.doi.org/10.1016/S0040-6090\(97\)00186-7](http://dx.doi.org/10.1016/S0040-6090(97)00186-7)
- [132] D. D. Boroleet al., "Effect of inorganic dopants (in presence of electrolyte) on the conductivity of polyaniline, poly(o-toluidine) and their copolymer thin films," *Material letters*, 57 (4), pp. 844-852 (2002); [http://dx.doi.org/10.1016/S0167-577X\(02\)00883-2](http://dx.doi.org/10.1016/S0167-577X(02)00883-2)
- [133] D. kumar, "Poly(o-toluidine) polymer as electrochromic material," *European Polymer Journal*, 37(8), pp. 1721-1725 (2001); [http://dx.doi.org/10.1016/S0014-3057\(01\)00018-0](http://dx.doi.org/10.1016/S0014-3057(01)00018-0)
- [134] F. Bai et al., "Template-free fabrication of silicon micropillar/nanowire composite structure by one-step etching," *Nanoscale Research Letters*, 7 (1), pp. 557 (2012); <http://dx.doi.org/10.1186/1556-276X-7-557>
- [135] K. S. Nahm, Y. H. Seo and H. J. Lee, "Formation mechanism of stains during Si etching reaction in HF-oxidizing agent-H₂O solutions," *Appl. Phys.*, 81(5), pp. 2418-2424 (1997); <http://dx.doi.org/10.1063/1.364248>
- [136] R. Douani et al., "Silver-assisted electroless etching mechanism of silicon," *Phy Stat Sol*, 205(2), pp.225-230 (2008) ; <http://dx.doi.org/10.1002/pssa.200723159>
- [137] W. Feng, "Synthesis and Characterization of Photoconducting Polyaniline-TiO₂ Nanocomposite," *Bull. Chem. Soc. Japan*, 73 (11) pp. 2627–2633 (2000); <http://dx.doi.org/10.1246/bcsj.73.2627>
- [138] T. Jeevananda et al., "Preparation of polyaniline nanostructures using sodium dodecylsulphate," *Materials Letters*, 62(24) pp.3995–3998 (2008); <http://dx.doi.org/10.1016/j.matlet.2008.05.041>
- [139] K. Hess, "Advanced Theory of Semiconductor Devices," Wiley-IEEE Press (2009); <http://dx.doi.org/10.1109/9780470544105>
- [140] Leonard J. Brillson, "Contacts to Semiconductors, Fundamentals and Technology," Noyes Press, Park Ridge, NJ, (1993)

- [141] T. Hoshi et al., “Low-Turn-on-Voltage Heterojunction Bipolar Transistors with a C-Doped InGaAsSb Base Grown by Metalorganic Chemical Vapor Deposition,” *Jpn. J. Appl. Phys.*, 51 p. 04DF01 (2012); <http://dx.doi.org/10.1143/JJAP.51.04DF01>
- [142] K. Akkilic, I. Uzunb, and T. Kilicoglu, “The calculation of electronic properties of an Ag/chitosan/n-Si Schottky barrier diode,” *Synth. Met.* 157 (6-7), pp. 297-302 (2007); <http://dx.doi.org/10.1016/j.synthmet.2007.03.009>
- [143] M. A. Yeganeh and S. H. Rahmatollahpur, “Barrier height and ideality factor dependency on identically produced small Au/p-Si Schottky barrier diodes,” *Journal of semiconductors*, 31 (7), pp.074001-1-7 (2010); <http://dx.doi.org/10.1088/1674-4926/31/7/074001>
- [144] Z-F Cao et al., “Determination of the series resistance under the Schottky contacts of AlGaN/AlN/GaN Schottky barrier diodes,” *Chin. Phys. B*, 21 (1), pp- 0171031-1-5 (2012); <http://dx.doi.org/10.1088/1674-1056/21/1/017103>
- [145] S.K. Cheung and N.W. Cheung, “Extraction of Schottky Diode Parameters from Forward Current- Voltage Characteristics,” *Appl. Phys. Lett.*, 49 (2), pp. 85-87 (1986); <http://dx.doi.org/10.1063/1.97359>
- [146] Salah E. El-Zohary et al., “Electrical Characterization of Nanopolyaniline/Porous Silicon Heterojunction at High Temperatures,” *Journal of Nanomaterials*, Volume 2013 pp. 1-8 (2013); <http://dx.doi.org/10.1155/2013/568175>
- [147] A. Ashery et al., “Fabrication and characterization of in situ polymerized n-polyaniline films grown on p-Si heterojunctions,” *Microelectronic Engineering*, 85, pp. 2309–2315 (2008); <http://dx.doi.org/10.1016/j.mee.2008.08.003>
- [148] P. Kumar, S. Adhikari and P. Banerji, “Fabrication and characterization of polyaniline/porous silicon heterojunction,” *Synth. Met.* 160 (13-14), pp. 1507–1512 (2010); <http://dx.doi.org/10.1016/j.synthmet.2010.05.011>
- [149] R. Poddar and C. Luo “A novel approach to fabricate a PPy/p-type Si heterojunction,” *Solid-State Electronics* 50 (11-12), pp. 1687–1691 (2006); <http://dx.doi.org/10.1016/j.sse.2006.10.006>

- [150] J.M.G. Laranjeira et al., "Fabrication of high quality silicon–polyaniline heterojunctions," *Applied Surface Science* 190 (1-4), pp. 390–394 (2002); [http://dx.doi.org/10.1016/S0169-4332\(01\)00901-1](http://dx.doi.org/10.1016/S0169-4332(01)00901-1)
- [151] Q. Zhang and G. Cao, "Nanostructured photoelectrodes for dye-sensitized solar cells," *Nano Today*, 6 (1), pp. 91-109 (2011); <http://dx.doi.org/10.1016/j.nantod.2010.12.007>
- [152] W. Lukosz, "Principles and sensitivities of integrated optical and surface plasmon sensors for direct affinity sensing and immunosensing," *Biosens. Bioelectron.* 6 (3), pp.215–225 (1991); [http://dx.doi.org/10.1016/0956-5663\(91\)80006-J](http://dx.doi.org/10.1016/0956-5663(91)80006-J)
- [153] M. A. Cooper, "Optical biosensors in drug discovery," *Nat. Rev. Drug Discov.* 1(7), pp. 515-528, (2002). <http://dx.doi.org/10.1038/nrd838>.
- [154] V. S.-Y. Lin et al., "A porous silicon-based optical interferometric biosensor," *Science* 278 (5339), pp. 840–843, (1997); <http://dx.doi.org/10.1126/science.278.5339.840>.
- [155] A. J. Haes, and R. P. Van Duyne, "A nanoscale optical biosensor: sensitivity and selectivity of an approach based on the localized surface plasmon resonance spectroscopy of triangular silver nanoparticles," *J. Am. Chem. Soc.* 124 (35), pp. 10596–10604, (2002); <http://dx.doi.org/10.1021/ja020393x>.
- [156] J. Homola, "On the sensitivity of surface plasmon resonance sensors with spectral interrogation," *Sens. Actuators B Chem.* 41 (1-3), pp. 207–211, (1997); [http://dx.doi.org/10.1016/S0925-4005\(97\)80297-3](http://dx.doi.org/10.1016/S0925-4005(97)80297-3).
- [157] M. E. Stewart et al. "Nanostructured plasmonic sensors," *Chem. Rev.*, 108 (2), pp. 494–521, (2008); <http://dx.doi.org/10.1021/cr068126n>
- [158] J. Homola, "Surface plasmon resonance based sensors," *Springer Series on Chemical Sensors and Biosensors*, (Springer, Berlin, 2006); <http://dx.doi.org/10.1007/b100321>
- [159] B. Min et al., "High-Q surface-plasmon-polariton whispering-gallery microcavity," *Nature* 457 (7228), pp. 455–458, (2009); <http://dx.doi.org/10.1038/nature07627>.
- [160] Q. Zhang et al., "A subwavelength coupler-type MIM optical filter," *Opt. Express* 17 (9), pp. 7549–7555 (2009); <http://dx.doi.org/10.1364/OE.17.007549>

- [161] M. A. Swillam, and A. S. Helmy, "Feedback effect in plasmonic slot waveguides examined using closed form," *Photonics Technology Lett.* 24 (6) pp 497-499 (2012); <http://dx.doi.org/10.1109/LPT.2011.2181350>.
- [162] T.-B. Wang et al. "The transmission characteristics of surface plasmon polaritons in ring resonator," *Opt. Express* 17 (26), 240961–24101 (2009); <http://dx.doi.org/10.1364/OE.17.024096>.
- [163] S. Randhawa et al., "Experimental demonstration of dielectric-loaded plasmonic waveguide disk resonators at telecom wavelengths," *Appl. Phys. Lett.* 98 (16), pp. 1–3 (2011); <http://dx.doi.org/10.1063/1.3574606>.
- [164] Lumerical Solutions, Inc. <http://www.lumerical.com/tcad-products/fdtd/> (Jan 2013)
- [165] Z. Liu et al., "Near-field Moiré effect mediated by surface plasmon polariton excitation," *Opt. Lett.* 32 (6), p. 629 (2007); <http://dx.doi.org/10.1364/OL.32.000629>.
- [166] P. Debackere et al., "Si based waveguide and surface plasmon sensors," *Proc. SPIE* 6477, Silicon Photonics II, vol. 6477, 647719 (2007); <http://dx.doi.org/10.1117/12.702040>
- [167] I. M. White and F. Xudong, "On the performance quantification of resonant refractive index sensors," *Optics Express*. 16 (2), p. 1021, (2008); <http://dx.doi.org/10.1364/OE.16.001020>
- [168] Z. Yu and S. Fan, "Extraordinarily high spectral sensitivity in refractive index sensors using multiple optical modes," *Optics Express*, 19 (11), pp. 10029-10040 (2011); <http://dx.doi.org/10.1364/OE.19.010029>.
- [169] Charles Lin et al., "Efficient broadband energy transfer via momentum matching at hybrid junctions of guided," *Applied Physics Letters*. 101(12), pp. 123115 (2012).
- [170] B. Lau, M. A. Swillam, and A. S. Helmy, "Hybrid orthogonal junctions: wideband plasmonic slot—silicon wire couplers," *Opt. Express* 18(26), 27048–27059 (2010), <http://dx.doi.org/10.1364/OE.18.027048>.